IMPROVEMENTS IN COMMINUTION EFFICIENCY THROUGH HIGH VELOCITY IMPACT

by

Amir Bahador Moosavi zadeh

B.A.Sc., University of British Columbia, 2009

A THESIS SUBMITTED IN PARTIAL FULFILLMENT OF THE

REQUIREMENTS FOR THE DEGREE OF

MASTER OF APPLIED SCIENCE

in

THE FACULTY OF GRADUATE STUDIES

(Mining Engineering)

THE UNIVERSITY OF BRITISH COLUMBIA

(Vancouver)

April 2012

ABSTRACT

In order to conduct efficient physical separation of a valuable mineral from an ore, the mineral in question must be liberated (broken into finer particles). Comminution, the physical process of rock breakage, accounts for a large portion (50 to 70%) of energy costs in the mining industry. Conventional comminution uses compressive forces to initiate and propagate cracks throughout the rock mass, yet it actually breaks under tension. Converting compressive forces into tensile ones is only 1 to 2 percent efficient. Blasting rock, in contrast, shows energy efficiencies of the order of 10 to 20%. This difference exists because a larger amount of forces are applied directly in tension and because the velocity of impact (and the rate of energy input) is orders of magnitude higher (10,000 m/s versus 10 m/s). This thesis reports on studies that build on previous work that showed high strain rates achieved through high speed impact can enhance the energy efficiency of comminution. The work examines the effects of high energy input and impact speed as separate, but interconnected, phenomena to explain from where the efficiency improvement derives. The project also takes a preliminary look at rock-on-rock breakage. Magnetite samples of varying sample weights and size distributions were impacted by a projectile at various speeds. Different materials and weights of projectile were studied. Before and after each experiment, the specific surface area of the sample was measured and the energy recovered as new surface energy was calculated. The results indicate that energy efficiency increases to about 5% (over 3 times that observed in conventional comminution) as impact speed reaches the range of 200 to 300 ms^{-1}. Above this velocity, the efficiency begins to fall off although significant comminution at higher than normal efficiency is still attained. The efficiency improvement results from both increased input energy and impact speed. Suggestions are given as to how this energy improvement could be scaled-up into a Barmac crusher. Recommendations are given for a new target chamber in the UBC CERM3 high-velocity facility in which the peak efficiency point at maximum compression might be eliminated in future testwork.

TABLE OF CONTENTS

LIST OF TABLES

LIST OF FIGURES

ACKNOWLEDGMENTS

I would like to take this opportunity to thank the many wonderful people who kindly lend me their support and assistance whether through their words of wisdom or through encouragement.

I would like to extent my appreciation for the support and guidance that my supervisor, Dr. John Meech provided me with. This study could not be done without his invaluable input, as well as the resources he provided me throughout my work. John, in addition to being a great supervisor with extensive technical knowledge, you are a great human being who taught me many valuable life lessons.

I would also like to thank Dr. Desmond Tromans for his valuable input and support.

I would also like to thank members of the Department of Mining Engineering - faculty, staff, and students - as well as members of the university community whom I have had the pleasure of knowing, for their assistance throughout my studies and for truly enhancing my university experience.

Most importantly, I would like to sincerely acknowledge the support and encouragement of my wonderful family, especially my mother, Ms. Elham Asefi and my father, Mr. Ghodratollah Moosavi-zadeh, for their patience and continuous assistance in every step of my life. Words cannot describe my level of appreciation for your sacrifices, thus, this work is dedicated to my wonderful family: my parents, my sister Shaghayegh, my brother AmirAbbas, and my sister-in-law Behnoush and our precious Nava.

1 INTRODUCTION

Comminution is a crucial process in mining and mineral processing operations. The process refers to the size reduction of solid materials through application of energy, usually by means of mechanical forces. Comminution is required to liberate valuable minerals from gangue (or waste minerals) and it consumes a major amount of the total energy used during mining and mineral recovery. It is reported that more than half the energy used in a typical mineral processing plant is for size reduction and liberation of minerals (Walkiewicz et al., 1991). In a typical cement plant, comminution (crushing and grinding) consumes over 60 percent of all electrical expenditures (Fujimoto, 1994).

Comminution efficiency in this work is defined as the ratio of the useful output energy to total input energy. Fundamentally, this can be calculated from the ratio of new surface energy to the total input energy. With this definition, the efficiency of conventional comminution has been shown to be of the order of only 1 to 2% (Whittles et al., 2006; Tromans & Meech, 2002; Walkiewicz et al., 1991), with most input energy being dissipated as heat (Austin, 1984). From measurements performed on a single stage ball mill, 85% of the energy was dissipated as heat, 14% was converted to kinetic energy with the actual efficiency into the ore being only 1% (Alvarado et al., 1998).

As such, even minor improvements in efficiency (1 or 2 percent) can result in considerable energy savings, thereby justifying the conduct of research on energy efficiency in comminution.

1.1 Comminution Energy

Crushing and grinding are the major stages of comminution. The main objectives of comminution are to produce particles of a required size and shape, to liberate valuable minerals from waste before concentration, and/or to increase surface area available for chemical reaction. About 50% of total comminution costs are attributed to energy consumption (Radziszewski, 2000) and it is estimated that comminution consumes over 3% of the total electricity generated worldwide (Fuerstenau et al., 1999). Grinding accounts for 90% of comminution energy compared to crushing which uses about 5-7% and

blasting at 3-5% (Alvarado et al., 1998). A breakdown of energy expenditures in a typical cement plant is shown in Figure 1.

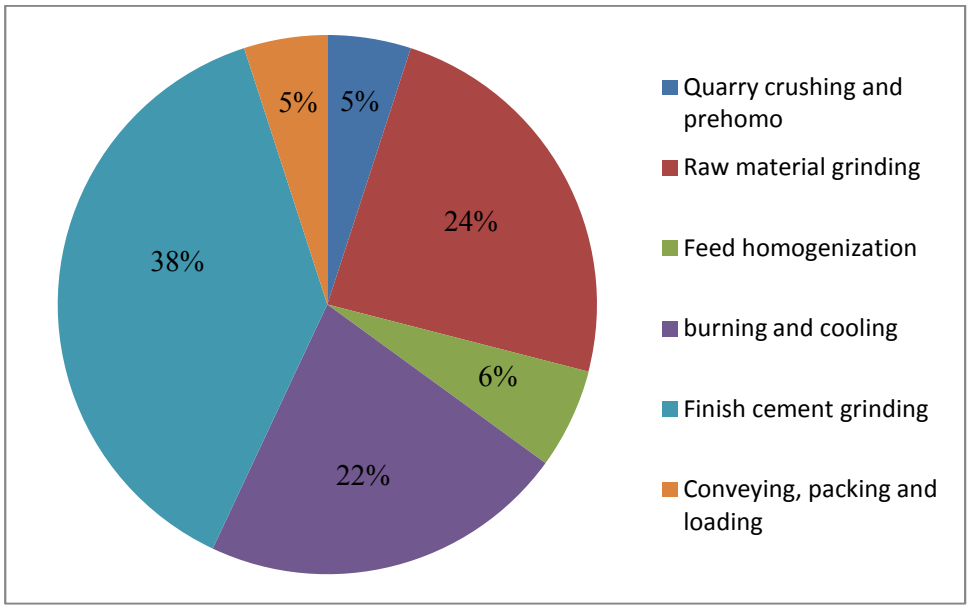

Figure 1. Distribution of electricity costs in a typical cement plant (Scheuer & Ellerbrock, 1992)

Energy consumption during rock breakage depends on the availability of micro- or macro-cracks within particles. Less and less of these fractures exist as material becomes finer (below about 100 microns) meaning these sizes are more resistant to breakage. For ultra-fine grinding, the very low microcrack density significantly increases a material's work index by as much as several orders of magnitude.

1.2 Problem Statement

Comminution efficiency in this work is determined from the ratio of the difference between the measured surface energy of the product and the feed (i.e., the energy of new surface created during size reduction) to the mechanical energy supplied to the machine that performs size reduction (Fuerstenau & Abouzeid, 2002). In a practical sense, the energy required to break a tonne of material from an infinite 80% passing size to an 80% passing size of 100 micron is defined as the Bond Work Index. This value can be determined from laboratory testwork as well as from observations taken

from an operating plant. Ratios of the plant value to the laboratory value can be used to evaluate the effectiveness of the operating plant which of course is subject to a great deal of variations in ore conditions, as well as plant operating changes. These efficiencies will typically range from a low level of about 75% to a high of perhaps 110%, but this does not reflect the real efficiency of energy used to break the ore.

Theoretical estimations suggest that the true energy efficiency during crushing and grinding is of the order of 1 to 2% (Tromans & Meech, 2002). Table 1 shows the estimated comminution energy efficiency and Bond work index for several minerals calculated by a thermodynamic analysis.

Table 1. Estimated energy efficiency of comminution and Bond Work Index for several minerals. (Tromans & Meech, 2002)

Mineral	Wi (kWh/ton)	Efficiency (%)
Galena	10.19	0.27
Fluorite	9.76	0.58
Pyrite	8.9	0.78
Garnet	12.37	0.94
Feldspar	11.67	0.97
Magnetite	10.21	1.38
Hematite	12.68	1.76
Rutile	12.12	2.03

The energy efficiency of particle fracture depends on several factors such as the loading force and the size and orientation of inherent micro-fractures in the particles. Generally, it may take a number of impacts before a force sufficient to propagate a fracture, is applied. Impacts that do not result in fracture generate elastic strain energy which is stored within the particles as thermal heat without any new surface area being produced which contributes to the inefficiency of the process (Tromans & Meech, 2004). Impact forces applied to a particle, as shown in Figure 2, result in compression parallel to the axis of impact and tensile stresses normal to the axis of impact. Interaction of these stresses may lead to the failure of the material with the orientation of internal flaws in the material playing a

key role in determining breakage efficiency. All rock particles fracture in tension, hence the transfer of a compressive force to a tensile stress is a major factor related to why efficiency is so low.

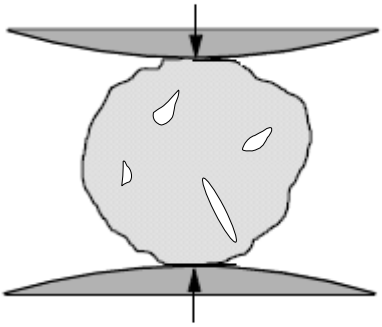

Figure 2. A particle with inherent flaws being impacted

1.3 Hypothesis of the Thesis

During comminution, kinetic energy applied through physical contact will transform to potential energy (stored in the material as surface energy), heat, and sound. Energy stored in the material as new surface areas is the useful energy with only a small fraction of the total energy (about one to two percent) contributing to the new surfaces.

However, energy efficiency in blasting, which is the first stage of the breakage of material, is at least an order of magnitude higher than that of grinding mills and crushers. The calculated efficiency ranges from about 13 to about 20%. Despite the high costs associated with drilling and blasting, downstream cost savings in crushing and grinding make this unit operation an effective method to increase overall comminution effectiveness (Eloranta, 1997). There are three factors that contribute to the high energy efficiency of blasting: first, the sudden increase in pressure and rapid rate of energy release causing the rock to fracture (i.e., energy input); second, the shock wave produced by blasting moves in all directions throughout the rock with a velocity over 2,000 ms^{-1} (i.e., better conversion of compression to tension forces) (Formby & Wharton, 1996); and thirdly, the material after blasting generally has a higher density of micro-cracks which reduce the material's Work Index. Based on these ideas, this research project was commenced in 2004 to examine if the intermediate stress regime

that exists between crushing equipment and blasting could be exploited to produce higher energy efficiencies. The approach taken was to design a facility to impact rock at high velocities (Sadrai et al., 2011) and a successful demonstration project showed that energy efficiency could be improved significantly as the impact velocity increased.

The research project described here was initiated to increase our understanding of how energy use improves when compressive forces are applied at high rates. The methodology of using the high impact velocity facility was refined to ensure reproducibility and better correlation between new surface area created and energy input at high impact velocities.

1.3.1 UBC-CERM3 High Velocity Impact Facility

The UBC-CERM3 high velocity impact facility (operating at speeds between 100 to 350 ms $^{-1}$) was built to study how impact velocity can improve fragmentation and minimize energy use. Aggregated rock samples are fragmented inside a chamber by being subjected to the impact of a projectile. The apparatus uses compressed gas at high pressure (up to 250 psi) to accelerate the projectile. Immediately before impact, the projectile speed is measured by two pairs of fixed laser diode detectors, which record the time of passage of the projectile (Sadrai et al. 2006). Figure 3 is a schematic diagram of the facility.

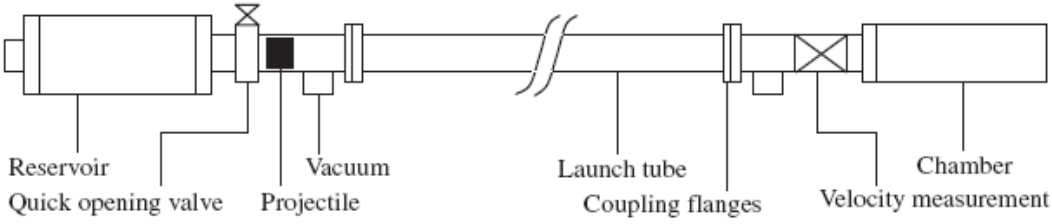

Figure 3. Design configuration of the UBC-CERM3 high-velocity impact apparatus (Sadrai et al., 2011)

The initial testwork used limestone, quartz, and rock salt. These materials were selected to observe the effect of impact velocity over a range of Poisson's ratios and porosities. For each material,

samples of -2mm + 1mm were prepared and impacted at different speeds. The results showed a clear influence of velocity on energy efficiency for all materials up to about 250 ms^{-1} with the suggestion that a peak may exist in that region (see Figure 4).

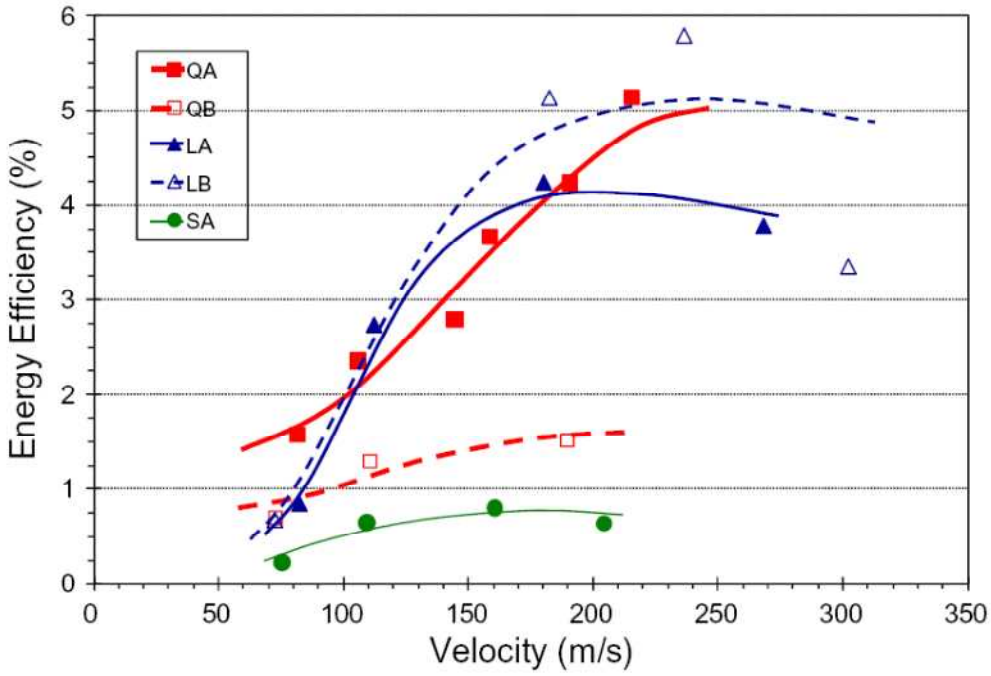

Figure 4. Energy efficiency as a function of impact velocity for Q=Quartz, L=Limestone, and S = Salt Rock (A = 13 gram sample and B = 25 gram sample) (Sadrai et al., 2011)

While the results show that energy efficiency increases with impact velocity, considerable scatter is evident. As a result, this project was undertaken to improve reproducibly and determine the influence of velocities above the apparent peak point. In addition, it was considered important to examine if the energy input rate or the level of velocity impact was more important in increasing energy efficiency.

1.4 Objectives of the Thesis

The purpose of this research is to explore methods to improve energy efficiency of comminution (processes and/or equipment) with the goal to decrease the cost of comminution. The specific objectives are as follows:

- To investigate the relationship between energy input during fragmentation and the amount of new surface area created within the rock mass.
- To investigate the effects of particle size and bed depth of particles on the relationship between energy efficiency and impact velocity.
- To separate the effects of impact velocity and input energy on energy efficiency.
- To simulate and examine relationships for rock-on-rock impact.
- To improve the reproducibility of testwork using the high velocity impact facility.

2 COMMINUTION PROCESSES

2.1 Summary

This section provides background on current comminution technology by reviewing the unit operations of blasting, crushing and grinding. Some of the specialized comminution equipment aimed at increasing energy efficiency and the basic principles of their operation are outlined. Previous work on the relationship between impact velocity and comminution efficiency is presented. Calculations are presented to demonstrate the energy requirements for one type of impact machine were it to be operated at higher velocities.

2.2 Current Comminution Technology

Comminution technology is widely used in modern industry, with all mining and mineral processing operations being major users of comminution equipment. Applications range from crushing of mined ore to grinding of very fine particles to produce advanced materials. The first stage of comminution includes rock cutting and blasting with blasting being the dominant method. Researchers have shown that an integrated approach comminution across the blasting and crushing stages can provide substantial energy and cost savings since the energy efficiency in blasting lies between 13 to 20 % (Dance et al., 2007; Workman, 2003; Paley & Kojovic, 2001; Dance, 2001; Eloranta, 1995).

2.2.1 Blasting Operations

The extraction of rock mass and subsequent fragmentation generally begins with drilling and blasting techniques. A number of holes are drilled using a specified pattern and these are filled with explosive. The blast is initiated row by row with micro-second to milli-second delays to allow the rock mass to move out through the free-face. The degree of fragmentation is affected significantly by the blast hole pattern – the distance and orientation between adjacent holes as well as the accuracy of the holes drilled with respect to the desired directions and lengths. The type of explosive is an important factor

with ammonium nitrate and fuel oil (ANFO) being the dominant choice. Environmental factors such as water infiltration into the holes can also play a major role in the success of a blast.

Immediately following detonation, two types of loading forces are applied to the rock: a shock wave that quickly travels out from the explosion cavity (drill hole) into the material surrounding the borehole and a longer duration gas pressurization loading (Fourney et al., 1993). Controversy exists over which type of loading has the highest contribution to fragmentation. Stress waves propagate throughout the rock in all directions at high velocities to form crack patterns which then separate from the application of the high pressure explosion gas onto the crack surfaces (Donzé et al., 1997; McHugh, 1983).

Energy efficiency is influenced by many factors including burden, stemming length, delay period between rows, placement of booster charge, booster ratio, and blast pattern (Singh et al., 1994). Blasting provides high energy efficiency in comparing surface area (energy) change of the rock mass with the chemical energy released from the explosion. A major reason behind this high level is that the transmitted energy directly produces tensile stresses causing fragmentation along the boundaries between blast holes. During blasting, impact velocity is much higher (3,000-6,000 ms^{-1}) than that within conventional mechanical equipment leading to an increased crack density. Moreover, existing flaws and discontinuities help distribute the explosive gas throughout the rock helping to propagate these cracks. In addition to fragmentation, the strength of the surrounding rocks is diminished because of the new cracks introduced, making subsequent operations more efficient. Comminution efficiency can be improved by intensified blasting (Chi et al., 1996). Reducing the blast burden and spacing by 25% led to an equal energy reduction during crushing and a 9% improvement in grindability.

Blasting is typically limited to achieving a top size (450 to 600 mm) sufficient to load and transport material to the primary crusher. These constraints are due to the cost of drilling and blasting and the problem of fly-rock generation and noise that may impact on nearby facilities.

2.2.2 Crushing Operation

The main objective of crushing is to reduce the material in size by breaking large particles into fragments. Crushers are designed to reduce particle size to a specific top size and sometimes, it is a requirement that a minimum amount of fines is produced, although it is impossible to produce only material larger than a desired minimum size. Since the main objective is size reduction, crushers are usually compared using the term "Reduction Ratio". This ratio is a performance metric defined as the 80% passing particle size in the feed divided by that in the product. The energy used is affected by feed size and hardness changes together with idling periods (or other delays) while awaiting new ore.

Crushing machines are normally massive pieces of equipment because of the tough nature of their operating environment. With all crushing equipment, crushing action results from stresses applied to particles by a moving solid surface within the equipment working against another (moving or stationary) solid surface. In the case of a gyratory or cone crusher, a cone (mantle) moves within a stationary bowl while in a jaw crusher, two plates are used – one moving and one stationary. The stresses produce strain within the ore particles leading to fracture when the deformation limit is reached. Crushers are commonly used for coarse (primary) breakage to 100 - 250 mm (4 - 10 inches), intermediate (secondary) to 25 - 65 mm (1 - 2.5 inches), and fine crushing to 12-20 mm (½ - ¾ inches). Both dry (< 5 %H_2O) and wet (~10 %H_2O) crushing of materials can be conducted, but coarse crushing is always done dry with intermediate crushing typically being done on dry materials as well. When the ore is very wet or contains high quantities of mud and/or clay minerals, then wet crushing may be used to advance the material through the equipment (Water Flush® crushing).

2.2.2.1 Jaw Crushers

Jaw crushers are one of the most commonly used types of crushing equipment (Jinxi et al., 2007; Georget & Lambrecht, 1982). This crusher is mainly used as a primary crusher and consists of two vertical jaws. One jaw is fixed while the other moves back and forth using a cam mechanism. As

shown in Figure 5, material is fed from the top where the distance between the jaws is highest (known as the gape). As material falls through the machine, movement of the jaws together with the narrowing distance leads to fracture as particles and jaws impact each other. Jaw crushers are typically used to treat ores at tonnage rates below 1,000 tph. Crushing occurs on the inward stroke of the moving jaw while product is discharged on the opening stroke.

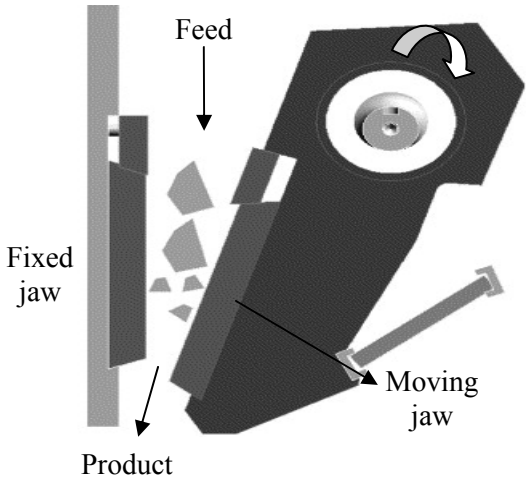

Figure 5. Jaw crusher mechanism (Lindqvist & Evertsson, 2003).

2.2.2.2 Gyratory Crusher

Gyratory crushers can be thought of as jaw crushers, only with circular plates. Figure 6 shows the cross-sectional view of this type of crusher. Tonnage rates are significantly higher than that of jaw crushers with individual units capable of treating up to 10,000 tph. Crushing and discharge take place continuously as the mantle moves around inside the bowl to be closed on one side and open on the other. In most high tonnage open-pit operations, gyratory crushers are used as primary crushers, especially when processing hard and abrasive ores. Compared to other crushers, they have the largest unrestricted opening and provide more flexibility in terms of moderating feed rates (Major, 2002).

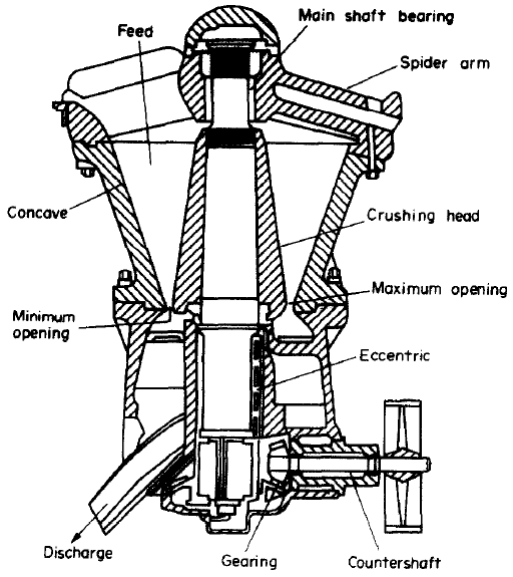

Figure 6. Cross-sectional view of a gyratory crusher (Biddulph, 1976).

With primary crushers the size of a unit is usually characterized by the gape (or opening) required to process the ore at its run-of-mine top size and its tonnage rate. These crushers are "set" by adjusting the Open-Side setting which essentially controls the top size of the discharged product.

2.2.2.3 Cone Crushers

Of all machines used in crushing plants, cone crushers have seen the greatest advancements and improvements in performance (Svensson & Steer, 1990). In a cone crusher, used mainly in secondary crushing plants, rocks are compressed between an eccentrically rotating spindle and a concave bowl similar to the configuration of a gyratory crusher, except in the latter case the bowl and mantle orientation is opposite (i.e., the bowl is convex). As large pieces of rock enter the crusher, they break and slide down to a lower position until they reach a size small enough to pass through the opening at the bottom of the crusher. Figure 7 demonstrates the operation of a cone crusher. With these units, the Closed-Side Setting is used to control product size and productivity mainly because of the difficulty in measuring the setting which is usually done using a piece of lead on a string and passed through the

crusher while it is idling. The angle and opening size of these crushers are different depending on the performance – either a secondary function (1 to 2.5") or a tertiary function (0.5 to 0.75").

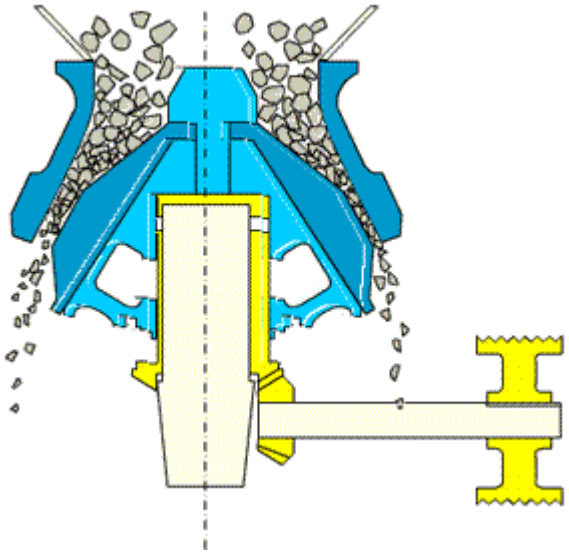

Figure 7. Schematics of a cone crusher

2.2.3 Grinding Mills

The main objective of grinding is also size reduction, but to a much finer size wherein about 80% of all valuable particles are fully liberated from gangue material. This limitation is generally determined by a cost/benefit analysis in which 80% liberation is the typical design target. Grinding equipment normally consists of a heavy surface that slides or rolls over another solid surface, with material caught between the two surfaces. This mechanism leads to shearing and impact stresses in the material, causing it to be ground by attrition or impact into very small sizes (between 10 to 200 microns). Typically, the grinding action is achieved by tumbling steel rods or balls inside a cylinder or autonomously, using larger ore pieces (or pebbles) to break smaller particles. Compared to crushers, grinding units possess a much larger reduction ratio. For crushing, the typical reduction ratio lies from 3 to 10, while for grinding it can be 100 or larger. Grinding mills are most often used for wet applications. However, there are some cases, such as coal preparation for combustion or in the

preparation of chemicals that may or may not be soluble, where ball mills are used to grind dry material – typically to ultra-fine sizes (less than 20 microns).

Energy is input into the rotating drum through a gear trunion that rotates the drum such that the velocity of the coarsest and heaviest material (generally the largest steel rod or ball) is about 80% of the critical velocity (the speed at which the ball centrifuges inside the drum as it rotates). Changes in feed size and ore hardness affect the actual energy required for a specific tonnage rate, but generally the steel charge (35-40% of the internal volume) determines the majority of energy needed. In the case of autogenous and semi-autogenous mills where the steel charge is from 0 to 18% of the total volume, the speed of the mill may be adjusted to compensate for varying ore parameters. Figure 8 shows the general operation of a ball mill while that of a rod mill is depicted in Figure 9.

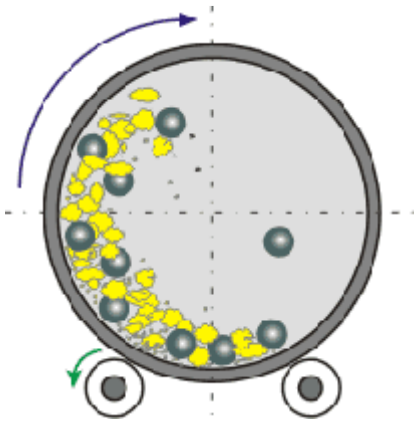

Figure 8. Ball mill schematics

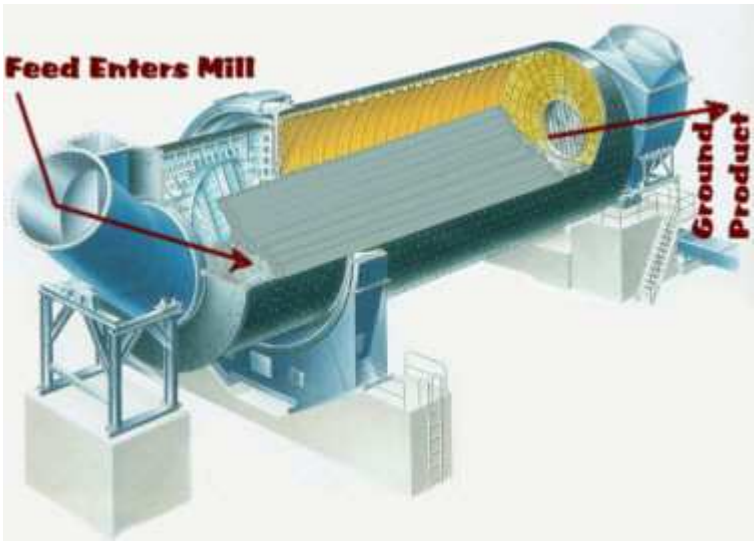

Figure 9. Rod mill operation

Grinding mills come in a variety of lengths and diameters. Typical rod and ball mills have length to diameter ratios greater than 1.0 and, in some cases separate compartments are used to isolate the steel balls. In the case of rod mills, although these types of mills have a self-regulating size control which generates a size distribution narrower than that of an equivalent ball mill, these units have reached a point of maximum length of about 6 m at which point the rods begin to bend under their own weight. As milling equipment has increased in size to reduce maintenance costs and downtime, rod mills have gone out of vogue to be replaced by large capacity ball mills and autogenous or semi-autogenous mills. Autogenous and SAG milling has increased dramatically over the past forty years due to the reduction in steel consumption and the desire for higher-capacity milling circuits. SAG and Ag mills can receive feed directly from a primary crusher, hence the secondary crushing plant can be eliminated. Many of these mills have length to diameter (L:D) ratios of less than 1.0 to increase the height at which the coarse particles or steel balls fall. Mills as large as 12 m in diameter are now in common use. Despite this increase in height, the velocity of impact is in the range of 10-20 ms^{-1}.

2.2.4 Hammer Mills

Hammer mills are a common grinding or crushing unit in small-scale operations or in those cases where fine breakage is undesirable. These units generally consist of a horizontal shaft, rotating at high speed within a cylindrical chamber, attached to a disk with a number of swing hammers located on its circumference. The material entering the mill is impacted and broken by the swinging hammers. The broken particles are thrown against the inside surface of the chamber. Hammer mills are used for intermediate to fine crushing and in some cases for ultrafine (grinding) size production. The velocity of the swing hammers is generally in the range of 10 to 50 ms^{-1} with the major limitation being wear rates and maintenance/replacement requirements.

Figure 10. A laboratory size hammer mill.

2.2.5 Attrition Mills

There are two types of attrition mills. One type, called the ring attrition mill, is used in laboratory-scale applications to grind samples to ultra-fine sizes. The unit consists of a cylinder within which a set of smaller cylindrical metal or ceramic rings are rotated. The action of these rings on the base of the cylinder leads to fine grinding of the material. Some commercial-scale versions are also in use.

Figure 11. Ring attrition mill.

A second type of attrition mill consists of two grooved flat circular rotating disks that face each other. The disks are either both rotating at high speeds (in opposite directions) or one of them is rotated while the other is fixed. Particles entering through an opening in one of the disks, pass towards the narrow gap between the disks, rubbing between the grooved surfaces and then discharged from the periphery (Sadler III et al., 1974). It is believed this type of milling has a high energy efficiency however, throughput is limited and is mainly used where production of ultra-fines is desired.

Figure 12. Laboratory attrition mill

2.2.6 Rolling Compression Mills

Although these types of mills have been around for many years, only recently have they made a resurgence due to the development in the 1960s of high-pressure compression milling. In this type of mill (the term "mill" is used because of the rotating nature of the device, similar to a ball or rod mill),

particles are caught and crushed between a roller and a solid surface. Bowl mills and roller mills are both considered rolling compression mills in which a rotating roller moves around the surface of a flat plate or a bowl. Rolling mills are mainly in use in the cement industry where dry grinding is preferred and air can be used to sweep ground particles off the surface of the flat plate or bowl.

2.2.6.1 High Pressure Grinding Rolls (HPGR)

Since its commercial introduction in the early 1980s, applications of HPGR have significantly increased in the last few years. HPGR is in wide use in the cement industry, but has had a considerably slower start in the mineral industry mainly due to a perception that wear rates are excessive. Over the last few years the problems with the wear rates have been addressed by the use of advanced wear-resistant materials leading to increased interest in the technology, particularly in copper and iron ore processing (Lim et al., 1997). HPGR offers a higher energy efficiency (about 30%) compared to processes such as semi-autogenous grinding (SAG) and balls mills (Rosario, 2010). It is today viewed as an alternative technology with a realistic potential to reduce comminution energy requirements (Daniel & Morrell, 2004).

The cross-section of an HPGR can be seen in Figure 13. Material is drawn from the feeder into the unit by rotating rolls. There are two counter-rolling rolls, with one moving linearly and the other one rotating around a fixed axis. This creates a high compression force leading to inter-particle stresses throughout the particle bed to create particle breakage. High inter-particle stresses result in a greater amount of fines in comparison to other comminution methods according to (D. Fuerstenau et al., 1995).

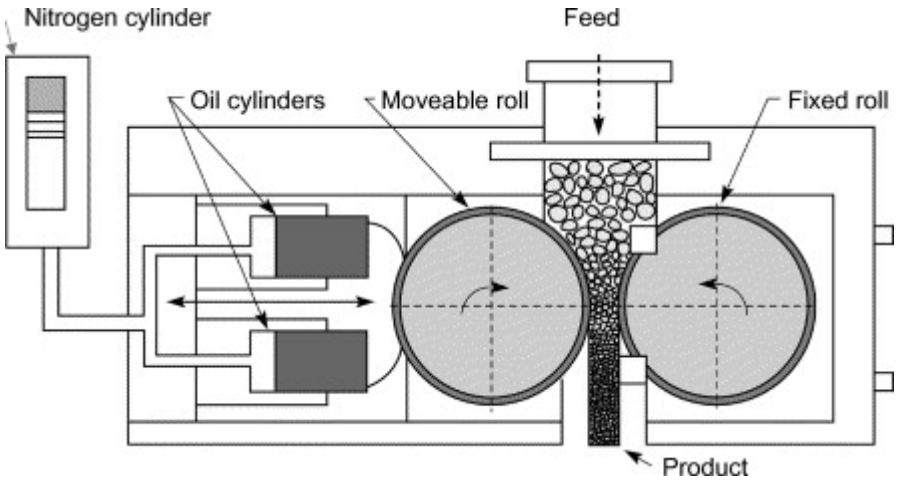

Figure 13. Schematics of HPGR (Napier-Munn, 1996)

It has been shown that weakening of particles in high-pressure roll grinding together with the HPGR product containing a greater amount of fines compared to other crushing methods leads to energy savings of the order of 20-40% (Tavares, 2005). The product leaves the unit as a compressed cake which must be broken-up for further processing. The energy to do this is relatively low.

2.2.7 Barmac Crusher

The Barmac crusher is a type of impact crusher invented in the early 1960s by McDonald and Bartley in New Zealand. It is a high energy centrifugal rock "pump" with a relatively high rotor speed up to 100 ms^{-1} tip speed (Hamer, 1998; Rodriguez, 1990). They are most commonly used in the cement and aggregate industries for abrasive materials. Figure 14 illustrates a schematic of a Barmac crusher.

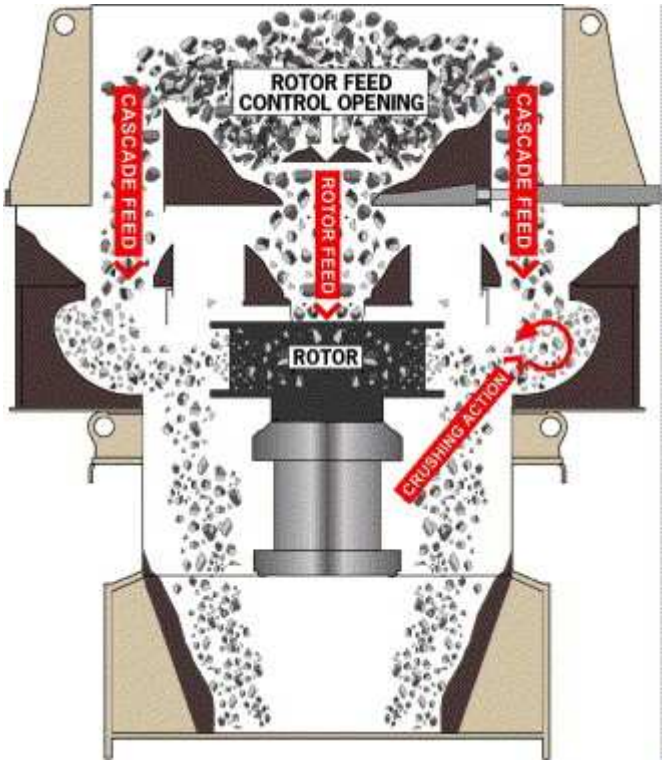

Figure 14. Schematic of Barmac crusher operation (Jankovic et al., 2004)

As the feed passes over the distributing plate, it is split into two separate streams. Part of the material passes into the central rotor where it is accelerated by the centrifugal force of the rotor action. The remainder of the material falls vertically in the form of a curtain around the periphery of the chamber. The rotor-accelerated material is driven outward into this curtain where particles meet at high impact velocity in the crushing chamber. This "rock-on-rock" crushing involves a number of fracture modes such as impact, attrition, and abrasion to reduce the material size. The crushed particles discharge through the clearance between the crusher chamber and the rotor wall (Jankovic et al., 2004; Sandvik et al., 1999). Simulation and modeling work have shown that pre-crushing using Barmac crushers or replacement of roller crusher circuits with Barmac crushers can improve energy efficiency of the circuit and reduce operating costs significantly (Jankovic et al., 2004; Sandvik et al., 1999).

2.2.8 Jet Milling

Jet mills are widely used in industries for ultra-fine grinding of solid materials, a unit operation process where particles are ground to a fineness in which 80% of the particles are smaller than 1-10 μm (Katz & Kalman, 2007). The milling component of a jet mill consists of a chamber and several nozzles. Particles are fed from a nozzle into a spiral opening where they are accelerated by pressurized gas or steam jets entering through other nozzles. The grinding effect is produced by collisions between the particles or by impact against solid surfaces. After breakage, material is classified from the center of the mill outlet (Vogel, 1991). The most significant variables in jet milling are feed rate, volumetric flow rate of air, and the height of the classification tube to provide a constant grinding pressure (Tuunila & Nyström, 1998). Feed rates and mass flow rates of air are the most important factors (Han et al., 2002; Ramanujam & Venkateswarlu, 1969). Figure 15 shows the components and operations of a jet mill (Cino Equipment, n.d.).

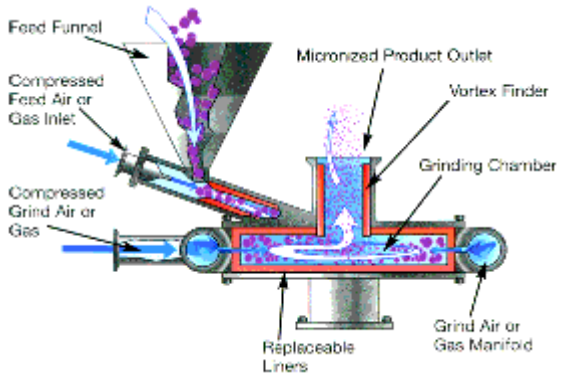

Figure 15. Components and operation of a jet mill.

High pressure water jet comminution shows great potential in coal pulverization with low energy consumption and high comminution efficiency and low equipment wear. The technique was first used in the mid-80s to disintegrate organic and non-organic materials, but applications today include coal comminution (Cui et al., 2006; Mazurkiewicz, 1984). The general operation of high pressure water

jets is similar to jet-milling with particles obtaining kinetic energy from the water jet, travelling at speeds from 200 to 400 ms^{-1} before colliding with each other and a target plate (Cui et al., 2006).

3 TESTWORK AND PROCEDURE

3.1 Summary

This section of the thesis outlines the testwork procedures used to conduct this research. The physical characteristics of the materials and the methods employed to prepare the samples are presented. The different steps of the experiments and the equipment used are discussed.

3.2 Sample Preparation

8 pieces of Lodestone (magnetite) were purchased from Ward's Natural Science. 6 pieces of these pieces, totaling about 4.5 kg in weight were crushed as shown in Figure 16.

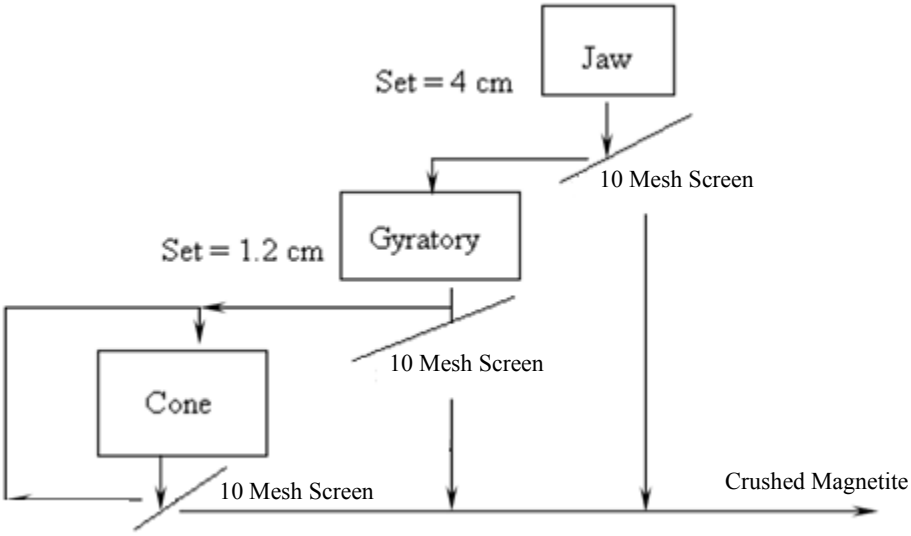

Figure 16. Crushing flowsheet

After crushing, a sieve analysis was performed on the material. Figure 17 shows the graph of cumulative weight percent passing as a function of particle size obtained from this analysis.

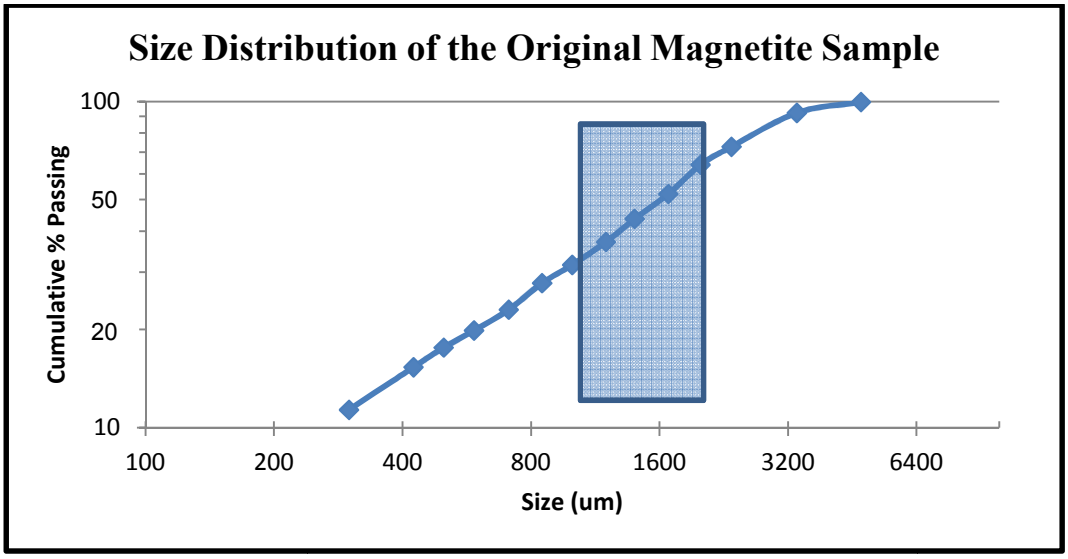

Figure 17. Sieve analysis on crushed magnetite

As expected, the size distribution in the region of interest (from 1mm to 2 mm), as highlighted on the graph, is approximately linear on a log-log graph.

Figure 18 illustrates the relationship between Specific Surface Area (SSA) of the original magnetite sample (before impact) as a function of particle size. Figure 18 indicates an unexpectedly high value for the SSA (0.78 to 0.8 m^2g^{-1}) of magnetite for the relatively large particles (1 to 2mm) involved in this work. For comparison purposes, a spherical grain of magnetite of size 1.5 mm would have a SSA of 80 cm^2g^{-1} – a value 100 times less than this measure. While one would expect to see a higher SSA for real-world particles, two orders of magnitude seems exorbitant. This discrepancy was believed to have occurred because of the magnetic properties of magnetite; larger particles attract many dust-sized particles to their surface. These tiny particles have an extremely high SSA which gives a false measure of the true SSA for the larger particles.

To verify this theory, a sample of the 1 to 2 mm size material was washed with water – gently shaken, not stirred – and then dried to ensure that most of the dust-like particles were eliminated from a subsequent measurement. The SSA of this washed material was determined to be 0.34 m^2g^{-1}, i.e., significantly lower than the initial measurement. The amount of dust washed out of the sample was

measured as 3.2%. If the dust has a mean particle size of 0.5 microns, then its theoretical specific surface area is 6.28 m^2g^{-1}. Assuming a 100% increase above theoretical (12.56), this gives a calculated specific surface area for the washed 1.5 mm sized magnetite of 0.41 m^2g^{-1} which is close to the measured value of 0.34.

The difficulty in isolating the -2+1 mm material from dust-sized particles does not affect the results of this work. The measured SSA gives the correct value before and after impact and the dust-sized particles in each sample remains as part of the sample throughout the experiment and within the final sample as well. All efficiency calculations are based on an accurate measurement of newly created surface area, i.e., the difference between the final and initial surface area of the material.

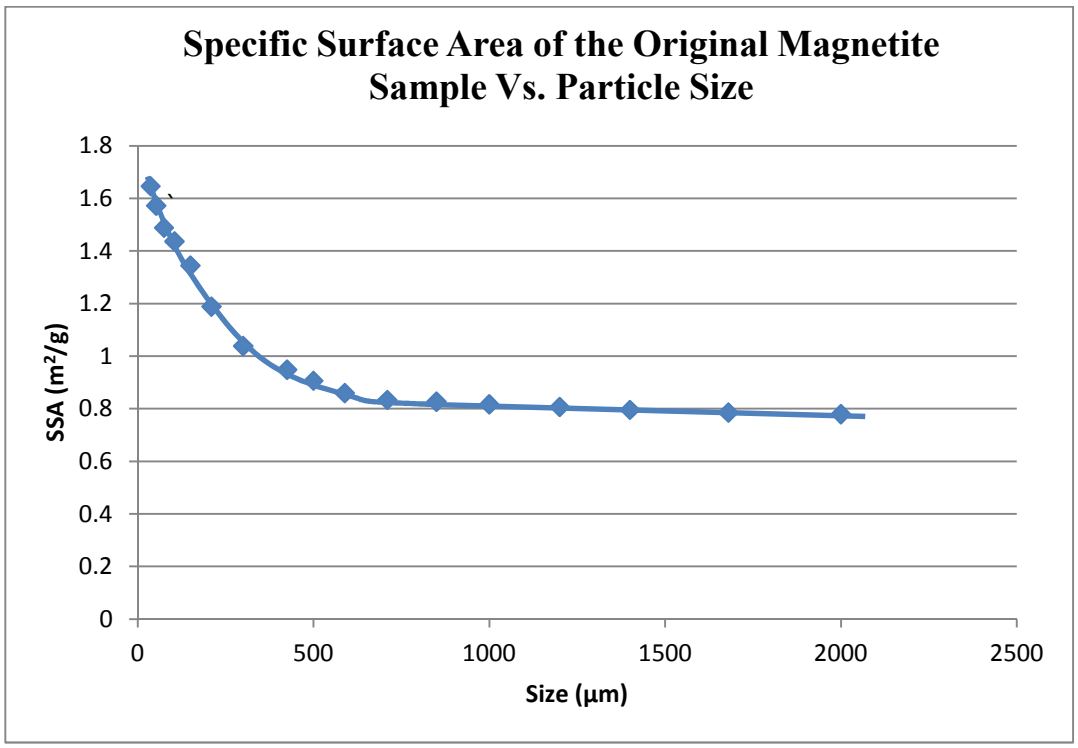

Figure 18. Specific Surface Area (SSA) of magnetite as a function of particle size

A representative sample of magnetite was prepared and sent for assaying. The results (as shown in Appendix F) show a total iron content of 68% with 24% FeO and 71% in the form of Fe_2O_3

indicating about 6% gangue minerals in the sample. So the sample consists of about 77% pure magnetite with about 16% pure hematite. Microscopic analysis shows considerable intergrowth between hematite and magnetite as would be expected of a lodestone sample.

3.3 Experiments

3.3.1 Samples

A total of 61 samples of different size distributions and different masses were prepared and impacted at various speeds by projectiles of varying lengths and different materials (steel, aluminum, and quartz glass). Each experiment was referenced using the following naming scheme:

[BulletLength][BulletMaterial]-[SampleWeight]Mag[SampleSizeID][ImpactSpeed]

Table 2 lists all the experiments that were conducted.

Table 2. Summary of all experiments

Experiment Type	# of Samples	Sample ID	Bullet Type	Sample Mass (g)	Size Distribution
Base Case	7	1/2"St-10MagAD	1/2" long Steel	10	1 mm – 2 mm
Repeatability and Error Minimization	10	1/2"St-10MagA	1/2" long Steel	10	1 mm – 1.2 mm
	5	1/2"St-10MagB	1/2" long Steel	10	1.2 mm – 1.4 mm
	5	1/2"St-10MagC	1/2" long Steel	10	1.4 mm – 1.68
	5	1/2"St-10MagD	1/2" long Steel	10	1.68 mm – 2 mm
Sample Size Distribution Effects	3	1/2"St-10MagE	1/2" long Steel	10	500 µm -589 µm
	3	1/2"St-10MagF	1/2" long Steel	10	210 µm -300 µm
	3	1/2"St-10MagG	1/2" long Steel	10	90 µm -150 µm
Sample Mass Effects	3	1/2"St-5MagAD	1/2" long Steel	5	1 mm – 1.2 mm
	3	1/2"St-15MagAD	1/2" long Steel	15	1 mm – 1.2 mm
Bullet Type Effects	3	1/4"St-10MagAD	1/4" long Steel	10	1 mm – 1.2 mm
	3	1"St-10MagAD	1" long Steel	10	1 mm – 1.2 mm
	4	1/2"Al-10MagAD	1/2" long Aluminum	10	1 mm – 1.2 mm
	4	1/2"Gl-10MagAD	1/2" long Glass	10	1 mm – 1.2 mm

Table 3 shows some of the physical characteristics of the material. The initial bulk density was calculated for the +1-2 mm size samples by placing a base case sample into the target chamber and measuring the sample bed depth. The specific surface energy for magnetite is from a literature value (Tromans & Meech, 2002) while the Bond Work Index was measured as described in Appendix C.

Table 3. Physical characteristics of magnetite

Specific Gravity (g/cm^3)	Initial Bulk Density (g/cm^3)	Specific Surface Energy (Jm^{-2})*	Bond Work Index (kWh/t)
5.15	2.18	6.449	11.3

* (Tromans & Meech, 2002)

3.3.2 Procedure

Before and after each experiment, a particle size analysis was performed on each sample using a sieving time of 10 minutes. Each experiment consisted of the steps shown in Figure 19. The specific surface area of the sample was measured using a BET surface area analyzer, then the sample was placed into the CERM3 High-Velocity Impact Facility and impacted using the appropriate projectile. The sample was retrieved, weighed, and its specific surface area measured after impact.

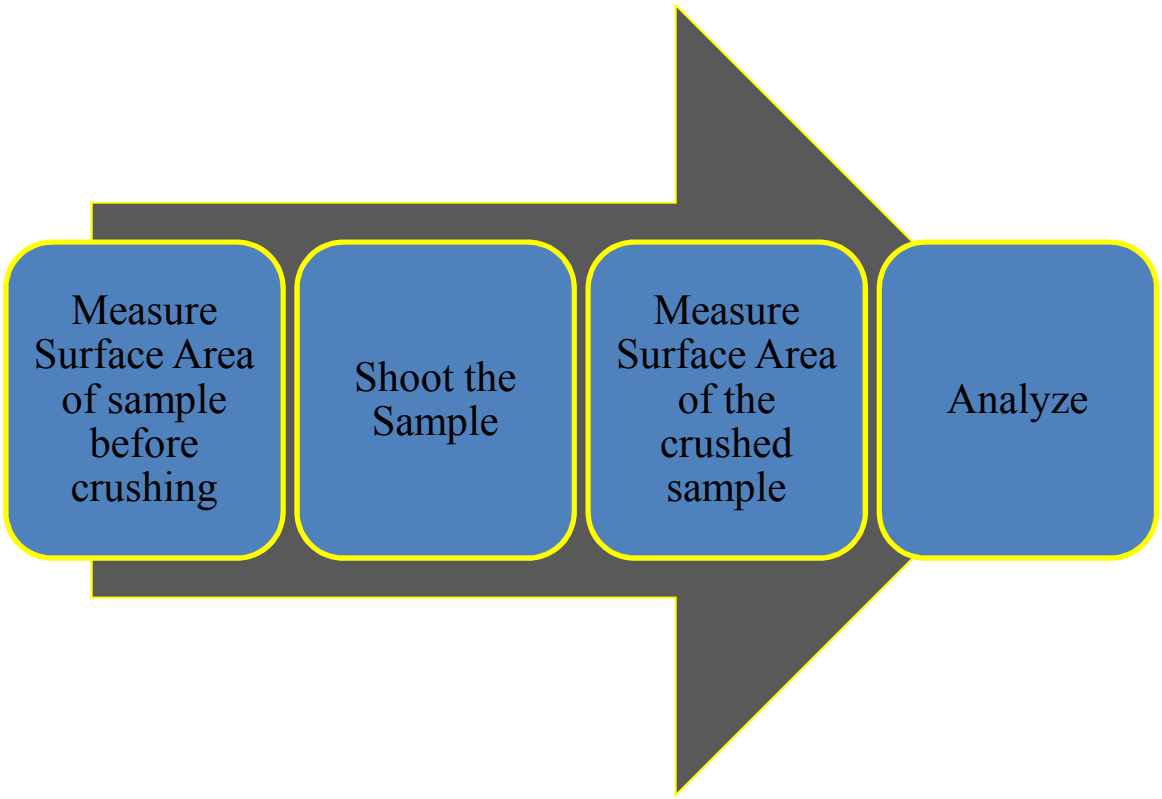

Figure 19. Experimental flowchart

The energy efficiency of breakage was then calculated using Equation 1:

$$\eta = 100 \times \frac{(SSA_{after}\text{-}SSA_{before})M_{sample}.S_E}{\frac{1}{2}M_{projectile}V^2} \quad (1)$$

where: η = Energy Efficiency (%)

SSA_{after} = Specific surface area after breakage (m^2/g)

SSA_{before} = Specific surface area before breakage (m^2/g)

M_{sample} = Mass of sample (g)

S_E = Specific surface energy (J/m^2)

$M_{projectile}$ = Mass of projectile (g)

V = Speed of projectile (m/s)

All variables were experimentally measured or calculated based on measurements except for the specific surface energy of magnetite which was taken to be 6.449 J/m^2 (Tromans & Meech, 2002). It is possible that as particles become smaller, their specific surface energy may increase as edges take on a more important role. However, Tromans and Meech, 2002 showed that this phenomenon does not become significant until the particle size drops below 1 micron. So in these experiments, the assumption that specific surface energy remains independent of particle size is considered reasonable.

3.3.2.1 BET Surface Area Analyzer

Since direct measurement of surface energy is not easily done without using calorimetry, the total surface area of each sample before and after crushing was measured to calculate the energy efficiency of the system. Measurements were done using a BET surface analyzer, called the AUTOSORB-1 by Quantachrome Instruments.

The equipment operates by measuring the quantity of nitrogen gas adsorbed onto a solid surface at an equilibrium vapor pressure. To obtain the necessary data, the material is placed in a sample cell maintained at a constant temperature and a known quantity of adsorbate gas is added to the cell. As adsorption occurs, the pressure in the sample cell changes until equilibrium is established. The difference between the amount of gas admitted and the amount required to fill the void space around the adsorbent is the amount of gas adsorbed at the equilibrium pressure. Using the Brunauer-Emmett-Teller (BET) (Brunauer et al. 1938) equation, the specific surface area of the sample is determined. For all experiments, nitrogen was used as the adsorbate gas.

3.3.2.2 Impact Testing using the High-Velocity Impact Facility

The apparatus used to conduct these experiments and crush the samples is a laboratory scale device designed and built at UBC (S. Sadrai et al., 2006). The apparatus consists of a one-stage gas gun in which air is pressurized to a maximum of 250 psi using an air compressor. The projectile, together with a carrier (or sabot) to ensure that the projectile stays on track, is placed inside one end of a 6 m

long pipe of 25 mm internal diameter, facing a target chamber at the opposite end. The target chamber is filled with the sample to be impacted and the pipe is evacuated to a level of less than 5 mm Hg using a vacuum pump. A number of solenoid valves are used to release the compressed air and evacuate the pipe.

To shoot the projectile, the solenoid valve that allows compressed air to enter the air chamber is triggered. The released air pushes the projectile assembly down the pipe accelerating it towards the target. About 25 cm before reaching the target, the diameter of the pipe abruptly changes to 12.7 mm which stops the sabot thus releasing the projectile with all the associated energy. Using two sets of laser diode detectors located at fixed positions, the projectile is detected and the time of travel recorded. This value is used to calculate the actual velocity of the projectile just before it enters the target chamber to impact the sample. After impact, the sample is recovered from the target chamber. Figure 20 shows the different components of the high velocity impact facility.

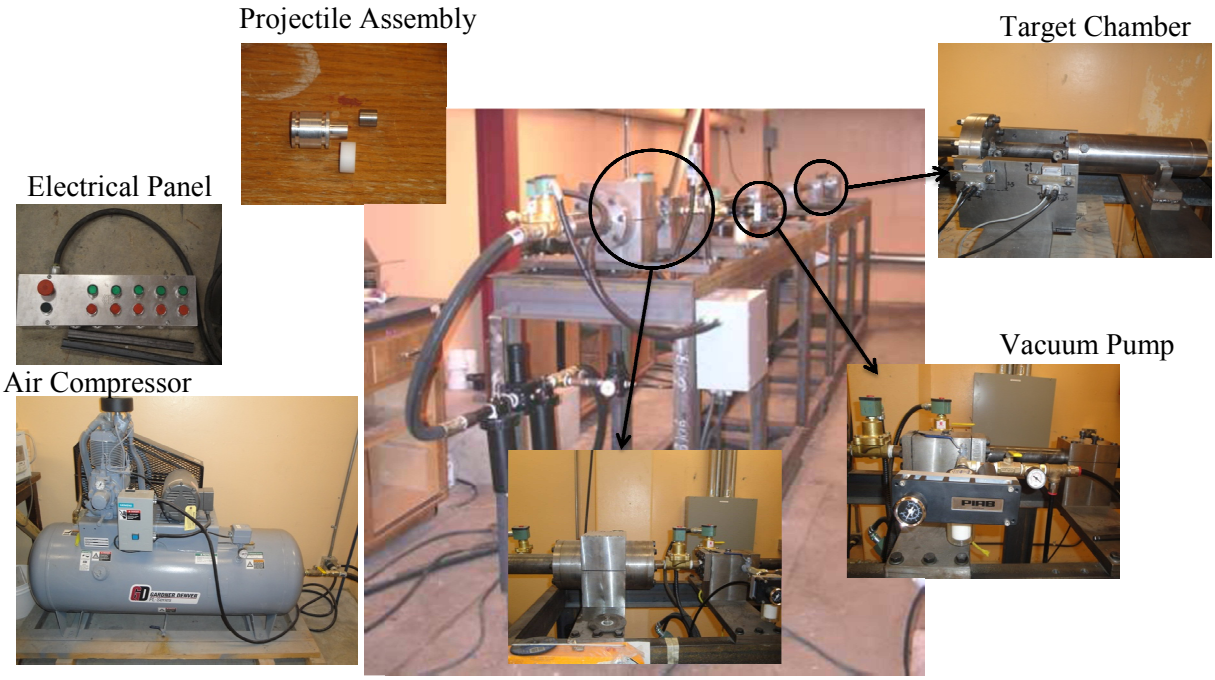

Figure 20. UBC-CERM3 high velocity impact facility

4 RESULTS AND DATA ANALYSIS

4.1 Summary

In this section, the results of the experiments performed are presented including the base case in which 1 to 2 mm size samples are impacted at various speeds by a 12.7 mm length steel projectile.

For all experiments, the size distribution of samples after impact as well as the relationship between energy efficiency and impact velocity is given. For some experiments, the 80% passing size of the product as a function of impact speed, the relationship between the Bond energy and input energy as well as the relationship between energy efficiency and input energy are also shown.

In the case of tests done with a glass projectile, the energy recovered into new surfaces in the broken projectile is also presented.

4.2 The Base Case (1/2"St-MagAD Series)

The 1/2"St-10MagAD series was used as the base case throughout this research. To prepare a representative sample and avoid potential errors, samples were prepared from each of the size distributions (from A to D) and mixed in the correct proportions to give the total AD sample with a linear relationship on a log-log scale.

After breakage, a particle size analysis was conducted on each sample as shown in Figure 21. Note that significant improvement in breakage is observed as the impact speed increases.

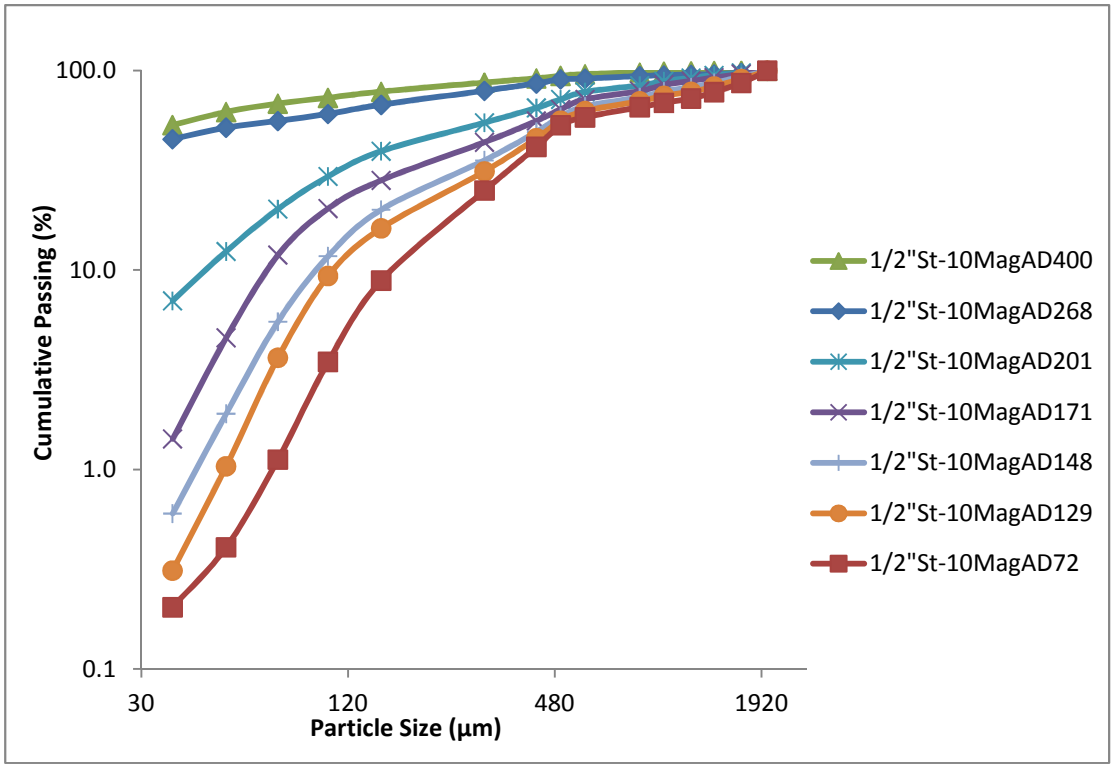

Figure 21. Particle size analysis for 10 gram 1-2 mm size magnetite samples impacted by 1/2" long steel bullet

Table 4 shows the P80 size, the Bond energy, and the weight percent - 37 µm size particles and weight% -150 µm size particles after impact. Note that the amount of undersize particles in the product significantly increases as the impact speed goes above 200 ms^{-1}. In other words, as the impact speed increases above this value, the amount of fines created in the product substantially increases.

Table 4. P80, Bond energy and weight percent -37 µm material and -150 µm material of the Base Case

Sample	Speed (ms^{-1})	P80 (µm)	Bond Energy (J)	- 37 µm Size (Weight%)	- 150 µm Size (Weight%)
Before Impact	0	1800	0	0	0.0
1/2"St-10MagAD72	72	1462	1.1	0.2	8.9
1/2"St-10MagAD129	129	1265	1.8	0.3	16.2
1/2"St-10MagAD148	148	1064	2.9	0.6	20.1
1/2"St-10MagAD171	171	875	4.2	1.4	28.2
1/2"St-10MagAD201	201	666	6.2	7.0	39.5
1/2"St-10MagAD268	268	313	13.4	45.3	67.4
1/2"St-10MagAD400	400	177	21.0	53.4	78.5

The Bond energy as a function of total input energy is shown in Figure 22. As can be seen, the Bond energy increases as the total input energy increases but appears to level out at high energy levels.

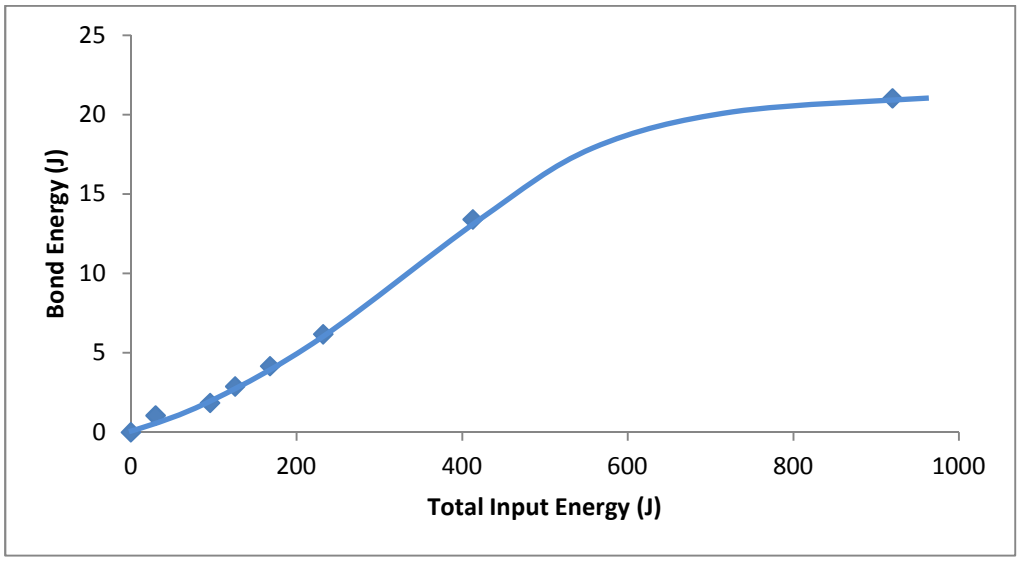

Figure 22. Bond energy as a function of total input energy for the 1/2"St-MagAD Series

During each experiment, some of the sample is unrecovered, which could contribute to experimental error. Table 5 shows the material lost in each experiment. On average, the material loss is about 1.7% and appears to be randomly distributed as a function of impact speed.

Table 5. Material loss during experiments for the 1/2"St-MagAD Series

Sample	Speed (ms^{-1})	Material Loss (g)	Material Loss (%)
1/2"St-10MagAD72	71.8	0.1097	1.10
1/2"St-10MagAD129	128.5	0.3410	3.41
1/2"St-10MagAD148	148.4	0.1242	1.24
1/2"St-10MagAD171	170.9	0.1392	1.39
1/2"St-10MagAD201	200.5	0.1069	1.07
1/2"St-10MagAD268	268.3	0.2113	2.11
1/2"St-10MagAD400	400.0	0.1378	1.38

Figure 23 presents the energy efficiency as a function of impact speed. As can be seen, the energy efficiency increases as speed increases, but peaks between 250 to 300 ms^{-1}. At this peak, the efficiency is about four to five times higher than the efficiency at speeds below 100 ms^{-1}.

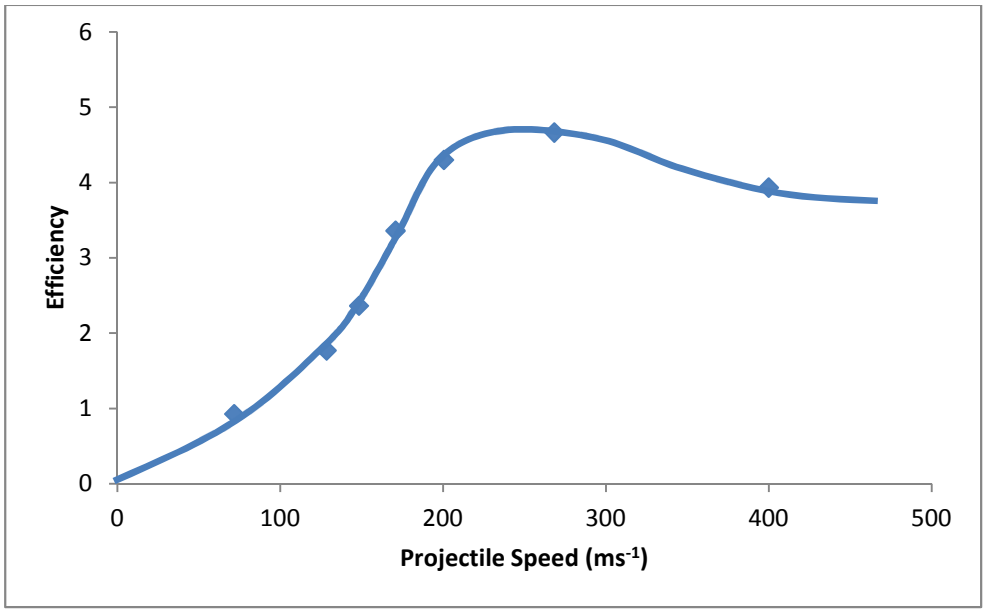

Figure 23. Energy efficiency as a function of impact speed for magnetite samples with a size distribution of 1 to 2 mm, impacted using 12.7 mm length steel bullets.

4.3 Reproducibility and Error Minimization

To examine the reproducibility of these experiments, additional tests were performed on individual samples of a tighter size distribution within the range of 1 to 2 mm. To produce a more precise feed size, 4 sets of samples from this size fraction were prepared with progressively smaller sizes. Ten representative samples of 1 to 1.2 mm size (A series), 5 samples of 1.2 to 1.4 mm size (B series), 5 samples of 1.4 to 1.68 mm size (C series) and 5 samples of 1.68 to 2 mm size (D series) were prepared. The samples were impacted with a 12.7 mm steel bullet at 5 speeds ranging from 100 ms^{-1} to 350 ms^{-1}. After breakage, a screen analysis was performed on each sample. As can be seen in Figure 24, experiments conducted at similar impact speeds generate almost identical particle size distributions, showing high reproducibility. For all sets, a similar trend to the base case is observed, i.e., as velocity increases, breakage becomes more efficient – the error band is about ±0.1%.

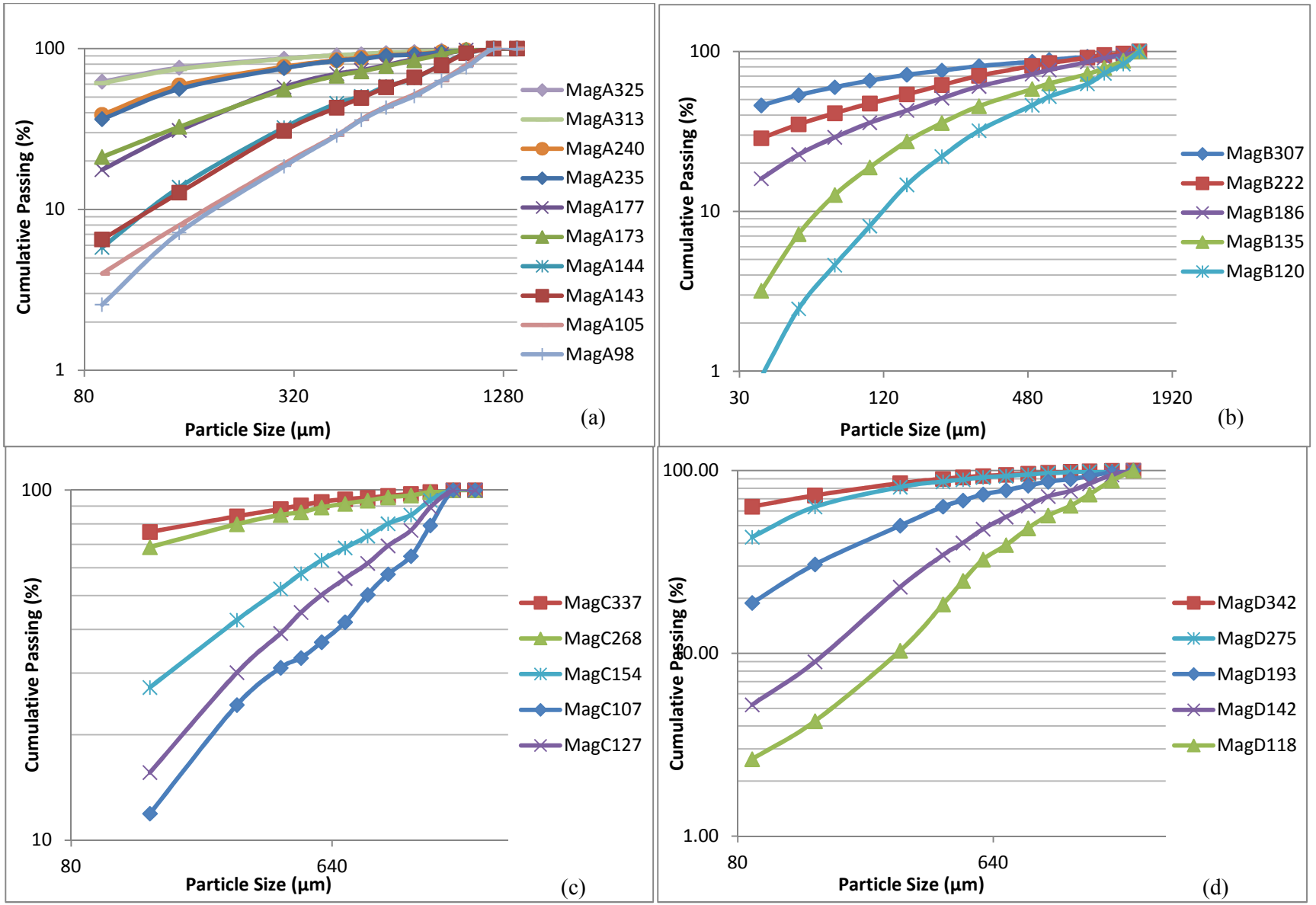

Figure 24. Particle size analysis of 10 gram magnetite samples, impacted by a 12.7 mm length steel bullet, with feed size distributions of a) 1 to 1.2 mm b) 1.2 to 1.4 mm c) 1.4 to 1.68 mm d) 1.68 to 2 mm.

The P80, Bond energy, and weight percent -150 µm size particles in the product are shown in Table 6 for each sample. As expected, the P80 is reduced and the amount of undersize particles increases as impact speed increases. Moreover, for similar experiments (experiments with very close impact speeds) the P80 and the amount of undersize particles in the product are similar.

Table 6. P80 and weight percent -150 µm material for MagA to MagD Series

Sample	Speed (ms^{-1})	P80 (µm)	Bond Energy (J)	- 150 µm Size (Wt. %)
1/2"St-10MagA Series				
Before Impact	0	1160	0.0	0.0
1/2"St-10MagA98	98	1031	0.7	7.2
1/2"St-10MagA105	105	1007	0.9	8.0
1/2"St-10MagA143	143	863	1.9	12.7
1/2"St-10MagA144	144	852	2.0	13.7
1/2"St-10MagA173	173	629	4.3	32.7
1/2"St-10MagA177	177	605	4.6	31.0
1/2"St-10MagA235	235	366	9.3	56.1
1/2"St-10MagA240	240	348	9.9	59.0
1/2"St-10MagA313	313	221	15.4	74.5
1/2"St-10MagA324	324	207	16.3	76.0
1/2"St-10MagB Series				
Before Impact	0	1360	0.0	0.0
1/2"St-10MagB120	120	1135	1.0	14.6
1/2"St-10MagB135	135	1026	1.7	27.4
1/2"St-10MagB186	186	684	4.5	42.8
1/2"St-10MagB222	222	476	7.6	53.8
1/2"St-10MagB307	307	264	14.0	71.4
1/2"St-10MagC Series				
Before Impact	0	1624	0.0	0.0
1/2"St-10MagC107	107	1410	0.7	11.9
1/2"St-10MagC127	127	1252	1.4	15.6
1/2"St-10MagC154	154	996	2.8	27.3
1/2"St-10MagC268	268	302	13.3	68.7
1/2"St-10MagC337	337	224	17.1	75.9

1/2"St-10MagD Series				
Before Impact	0	1936	0.0	0.0
1/2"St-10MagD118	118	1517	1.2	4.3
1/2"St-10MagD142	142	1272	2.2	9.0
1/2"St-10MagD193	193	767	5.4	30.7
1/2"St-10MagD275	275	290	14.6	63.3
1/2"St-10MagD342	342	234	17.4	73.2

The P80s for each of the above experiments are plotted against impact speed in Figure 25. As observed, for impact speeds between 100 to 250 ms^{-1}, the P80 decreases rapidly as impact speed increases, but after 250 ms-1, the rate at which the P80 decreases drops. Note that at speeds above 250 ms^{-1}, the P80 size for all experiments regardless of the original size distribution appears to converge to about 200 µm.

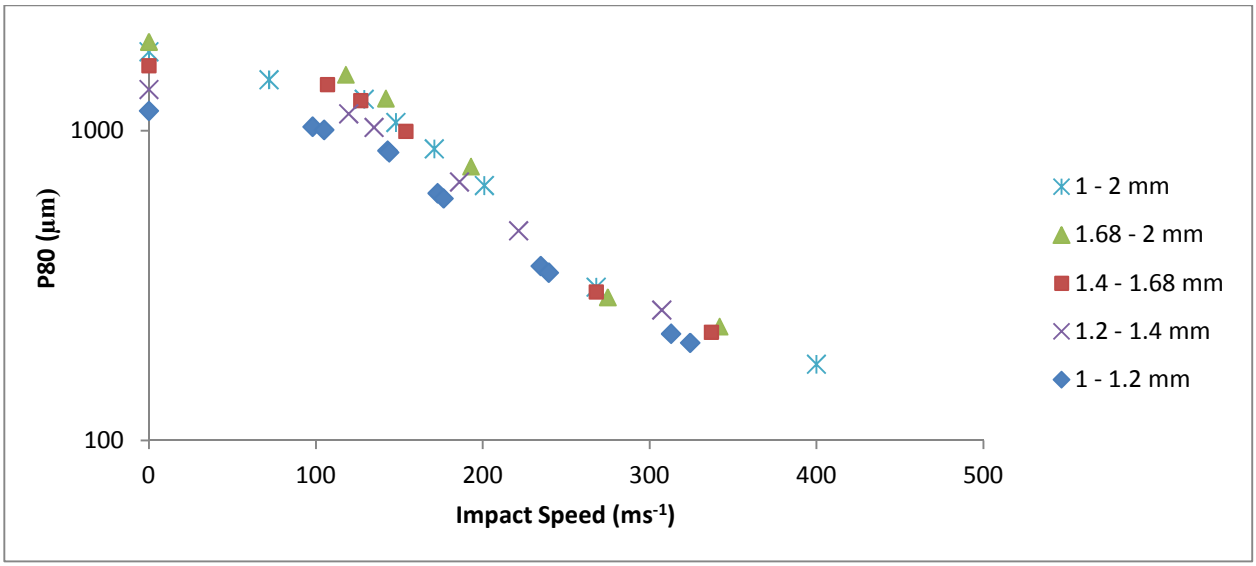

Figure 25. P80 as a function of impact speed for samples with various size distribution (between 1 to 2mm)

Figure 26 shows the Bond energy as a function of impact speed. Note that all results appear to follow a similar trend line simply displaced slightly along the trend line reflecting their different initial particle size. Note as well, that the Bond energy appears to level off at high velocities and high input energy levels.

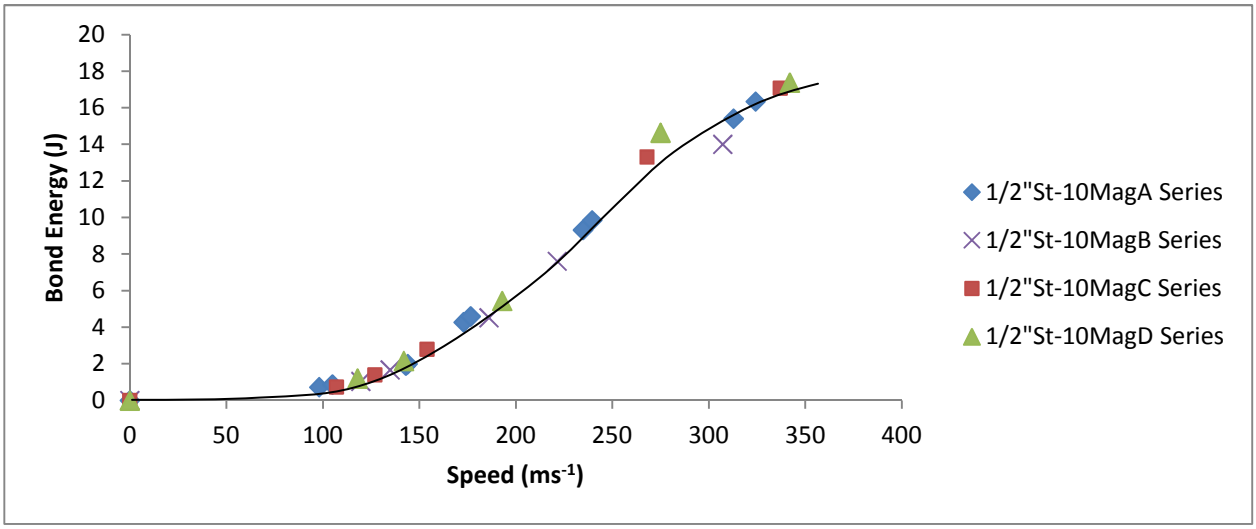

Figure 26. Bond energy as a function of impact speed for samples with various size distribution (between 1 to 2mm)

A graph of Bond energy as a function of total input energy is presented in Figure 27.

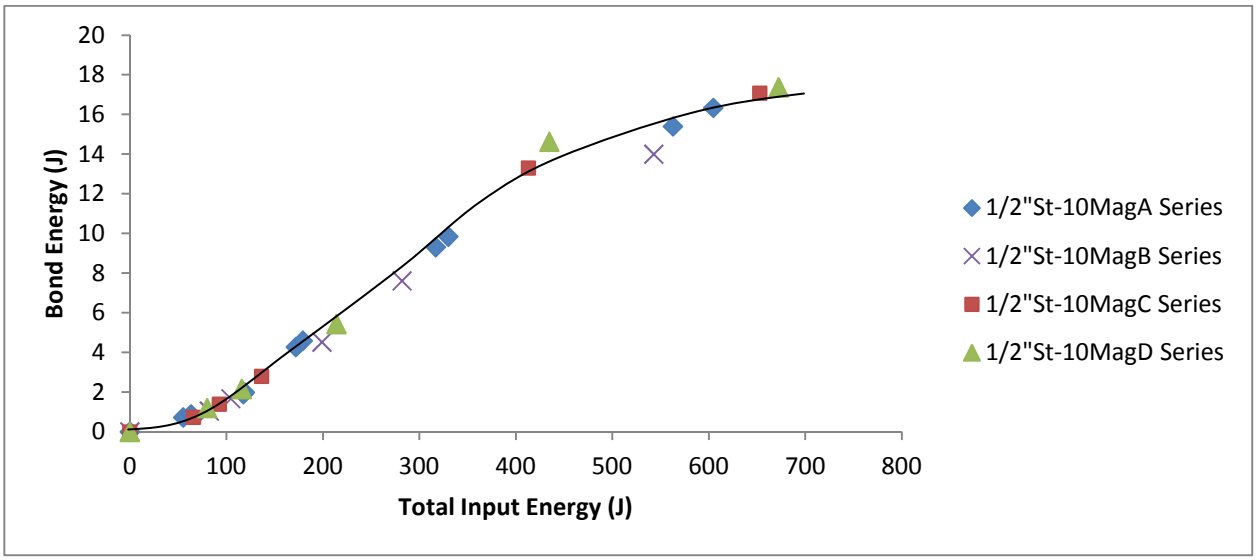

Figure 27. Bond energy as a function of total input energy for samples with various size distribution (between 1 to 2mm)

Energy efficiency as a function of impact speed is given in Figure 28. A peak efficiency is observed at a speed of about 250 ms^{-1}. The reproducibility of the experiments is clearly apparent. The trend of efficiency as a function of impact speed and the velocity at which the efficiency peaks are similar for all four sets of experiments.

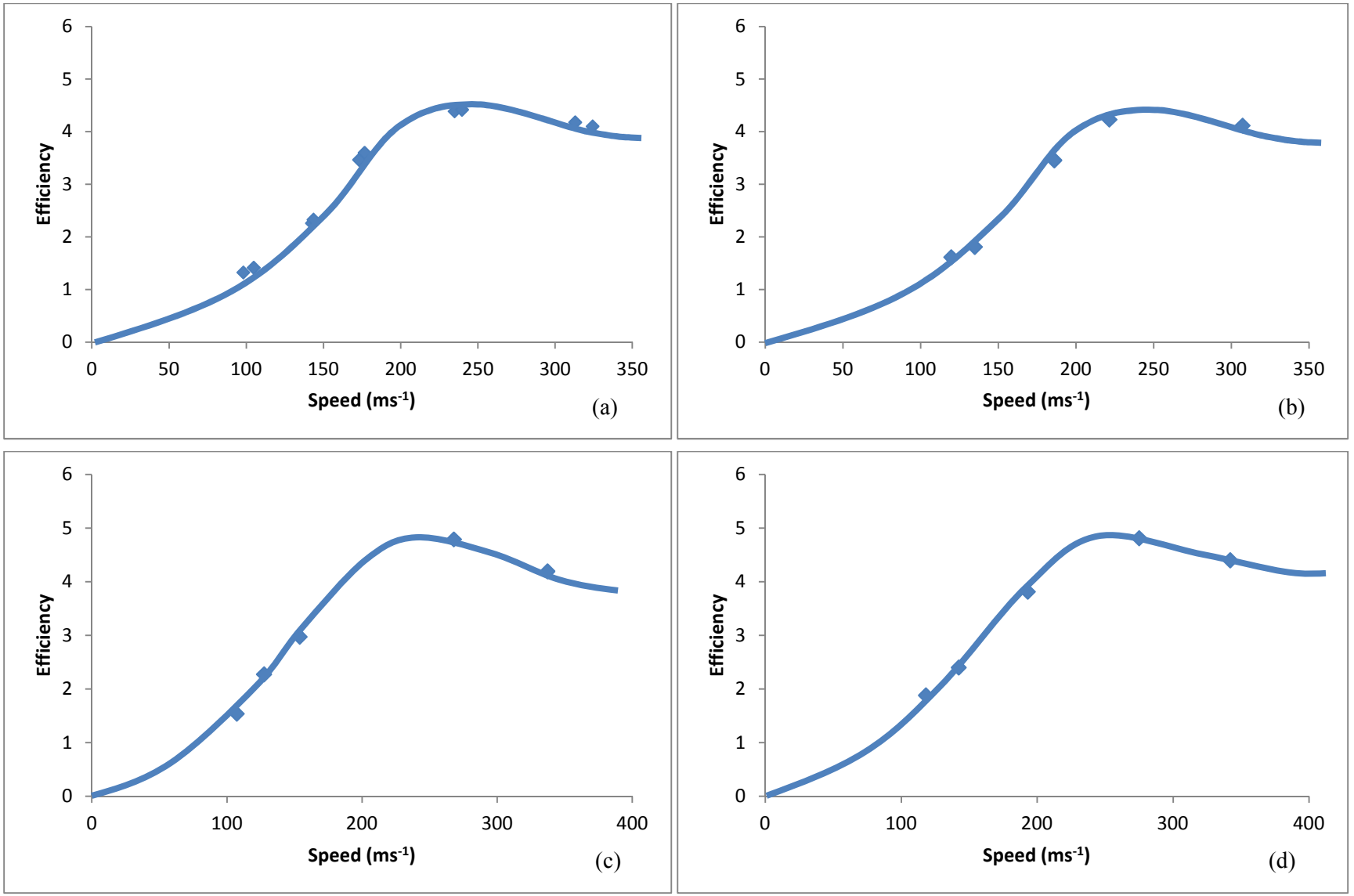

Figure 28. Impact efficiency as a function of impact speed for magnetite samples (impacted using a 12.7 mm length steel bullets) with a size distribution of a) 1 to 1.2 mm b) 1.2 to 1.4 mm c) 1.4 to 1.68 mm d) 1.68 to 2 mm.

4.4 The Effect of Particle Size Distribution

The above experiments raise the question of how the relationship between the energy efficiency and impact speed changes as the feed particle size distribution varies. More specifically, does this trend continue as the feed size becomes finer? To answer this question, another set of experiments was designed with an ever decreasing particle size distribution. A total of 9 representative samples, 3 of 500 to 589 μm size (E series), 3 of 210 to 300 μm size (F series), and 3 of 90 to 150 μm (G series), were prepared and impacted using a 12.7 mm length steel bullet at speeds ranging from 100 ms^{-1} to 350 ms^{-1}. Figure 29 shows the results of these tests. As can be seen, better breakage occurs as the impact speed is increased but the effect seems to drop off with decreasing feed particle size.

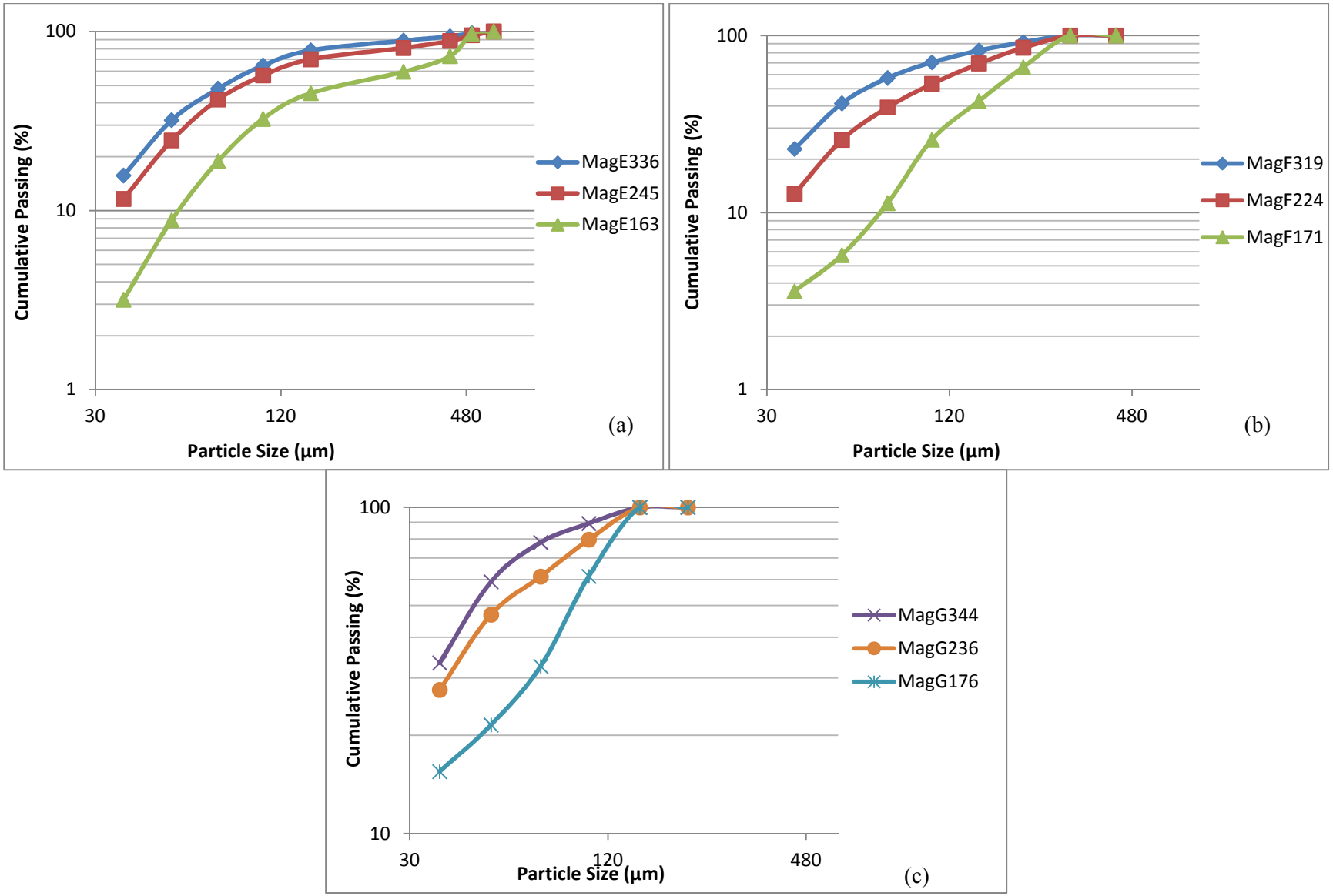

Figure 29. Size analysis for 10g mag. samples impacted by a 12.7 mm long steel bullet, with a feed size distribution of a) 500 to 589 µm b) 210 to 300 µm c) 90 to 150 µm.

Table 7 contains the P80, Bond energy and weight percent of -37 µm size particles after impact for each sample. As expected, the amount of undersize particles increases as impact speed increases. Moreover, at the same impact speed, the amount of undersize particles in the product is higher when the size of the original sample is smaller.

Table 7. P80, Bond energy, and weight percent of - 37 µm material for MagE, MegF and MagG Series

Sample	Speed (ms^{-1})	P80 (µm)	Bond Energy (J)	- 37 µm Size (Weight %)
1/2"St-10MagE Series (-589 + 500 microns)				
Before Impact	0	571	0.0	0.0
1/2"St-10MagE163	163	447	2.2	3.2
1/2"St-10MagE245	245	286	7.0	11.6
1/2"St-10MagE336	336	172	14.0	15.7
1/2"St-10MagF Series (-300 + 210 microns)				
Before Impact	0	282	0.0	0.0
1/2"St-10MagF171	171	247	1.7	3.6
1/2"St-10MagF224	224	190	5.3	12.7
1/2"St-10MagF319	319	127	11.9	22.8
1/2"St-10MagG Series (-150 + 90 microns)				
Before Impact	0	138	0.0	0.0
1/2"St-10MagG176	176	127	1.5	15.5
1/2"St-10MagG236	236	106	4.9	27.5
1/2"St-10MagG344	344	77	11.7	33.4

The relationship between the Bond energy and input energy for this series of experiments is shown in Figure 30. Note that the Bond energy appears to increase at a higher rate for samples with the coarsest feed size distributions as a function of total input energy whereas for the finer sized samples the slope appears to remain the same and the Bond energy does not show a leveling off at high energy levels.

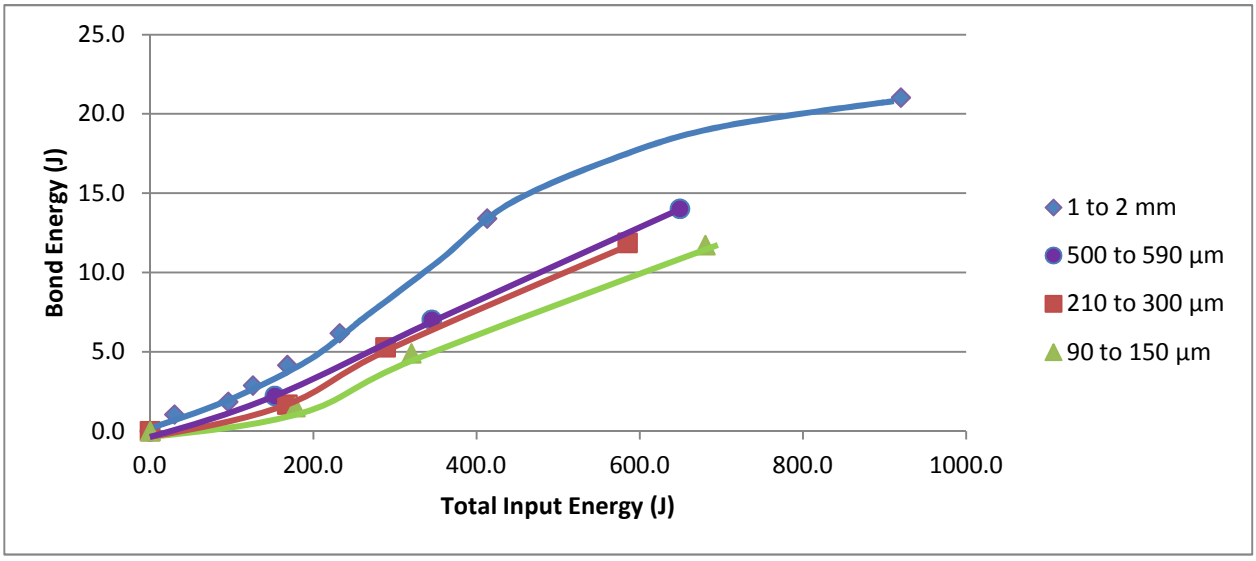

Figure 30. Bond energy as a function of total input energy for samples of different size distributions

Figure 31 shows how energy efficiency changes as a function of impact speed for four sets of different size distributions. As observed, the trend of each graph is similar, but energy efficiency at a particular impact speed is lower for finer feed size distributions. As well, the point at which energy efficiency peaks appears to increase as feed size decreases. For the G series, the efficiency peaks at 350 ms^{-1}.

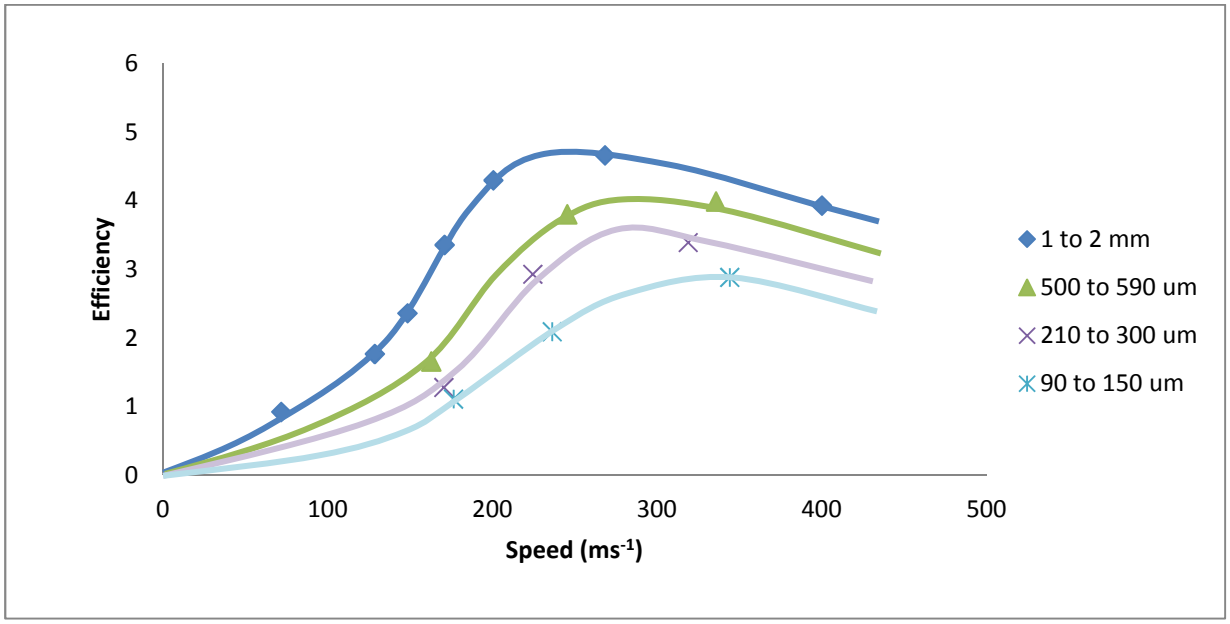

Figure 31. Comparison of energy efficiency vs. impact speed for samples of different size distributions

The velocity at which efficiency peaks together with the peak efficiency for each set is shown in Table 8.

Table 8. Estimated peak efficiency and velocity for each feed size

Feed Size (μm)	Peak Velocity (ms^{-1})	Peak Efficiency (%)
1000-2000	240	4.8
500-590	280	4.0
210-300	310	3.4
90-150	350	2.8

4.5 The Effect of Sample Mass

A factor that may also affect energy efficiency achieved for a particular impact speed is the weight of the sample (or the bed depth of the target). To investigate this aspect, three 5g and three 15g samples with the same particle size distribution as the base case were prepared. The samples were each impacted by a 12.7 mm length bullet at speeds ranging from 100 to 350 ms^{-1}. Figure 32 shows the particle size distribution of the 5g and 15g samples after impact. As can be seen, at lower speeds (below about 220 ms^{-1}) the amount of breakage observed in the 5g samples is higher than that observed in the 10g samples (base case) at similar speeds. But, at speeds close to 300 ms^{-1}, it appears that better breakage occurs for the 15g samples.

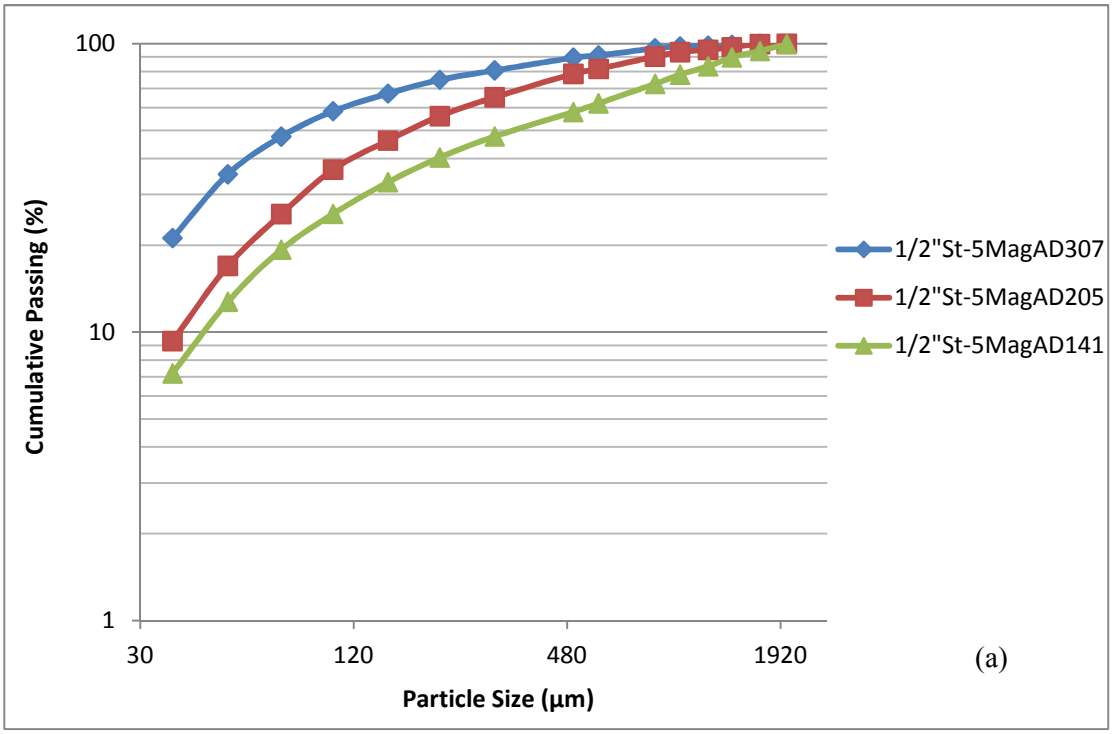

Figure 32. Particle size analysis for 5g, 1-2 mm size magnetite samples

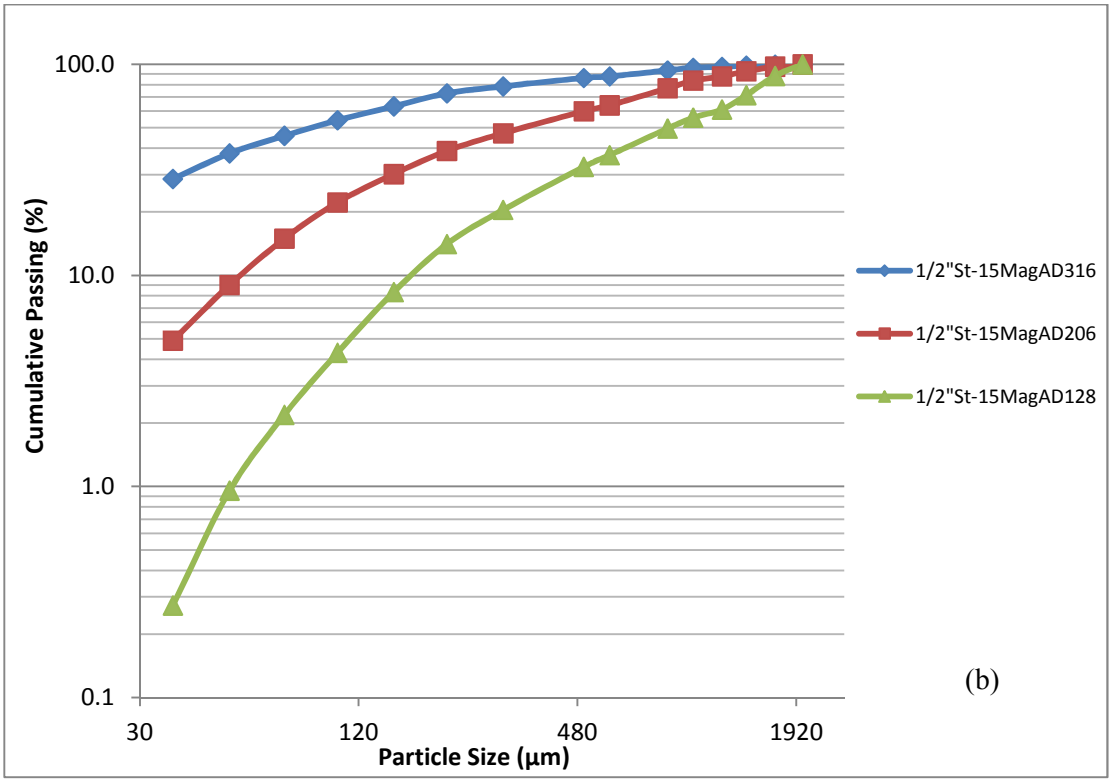

Figure 33. Particle size analysis for 15g, 1-2 mm size magnetite samples impacted by 12.7 mm long steel bullet

The P80, Bond energy and weight percent of - 37 μm and - 150 μm in the product is shown in Table 9. As expected, the amount of undersize particles increases as impact speed increases. However, at lower speeds (under 210 ms^{-1}), the amount of undersize particles in the product is higher at lower masses. As the speed increases to about 300 ms^{-1}, the amount of these undersize particles for the 5 gram sample is lowest, while the amount of undersize particles for the 10 gram sample is much higher than that of the 15 gram sample.

Figure 34 shows the Bond energy as a function of input energy for samples of different mass. The Bond energy for the 5g samples at constant energy is lower than that of the 10g and the 15g samples. However, the Bond energy of the 10g samples is equal, if not higher, than that of the 15g samples up to an input energy level of ~400 J.

Table 9. P80, Bond energy and weight percent of -37 μm and -150 μm material for 5MagAD, 10MagAD and 15MagAD Series

Sample	Speed (ms^{-1})	P80 (μm)	Bond Energy (J)	- 37 μm Size (Weight %)	- 150 μm Size (Weight %)
1/2"St-5MagAD Series					
Before Impact	0	1800	0.0	0.0	0.0
1/2"St-5MagAD141	141	1068	1.4	7.2	33.1
1/2"St-5MagAD205	205	538	4.0	9.3	46.2
1/2"St-5MagAD307	307	287	7.2	21.2	67.2
1/2"St-10MagAD Series					
Before Impact	0	1800	0.0	0	0.0
1/2"St-10MagAD72	72	1462	1.1	0.2	8.9
1/2"St-10MagAD129	129	1265	1.8	0.3	16.2
1/2"St-10MagAD148	148	1064	2.9	0.6	20.1
1/2"St-10MagAD171	171	875	4.2	1.4	28.2
1/2"St-10MagAD201	201	666	6.2	7.0	39.5
1/2"St-10MagAD268	268	313	13.4	45.3	67.4
1/2"St-10MagAD400	400	177	21.0	53.4	78.5
1/2"St-15MagAD Series					
Before Impact	0	1800	0.0	0.0	0.0
1/2"St-15MagAD128	128	1543	1.2	0.3	8.3
1/2"St-15MagAD206	206	916	5.8	4.9	30.2
1/2"St-15MagAD316	316	337	18.9	28.6	63.2

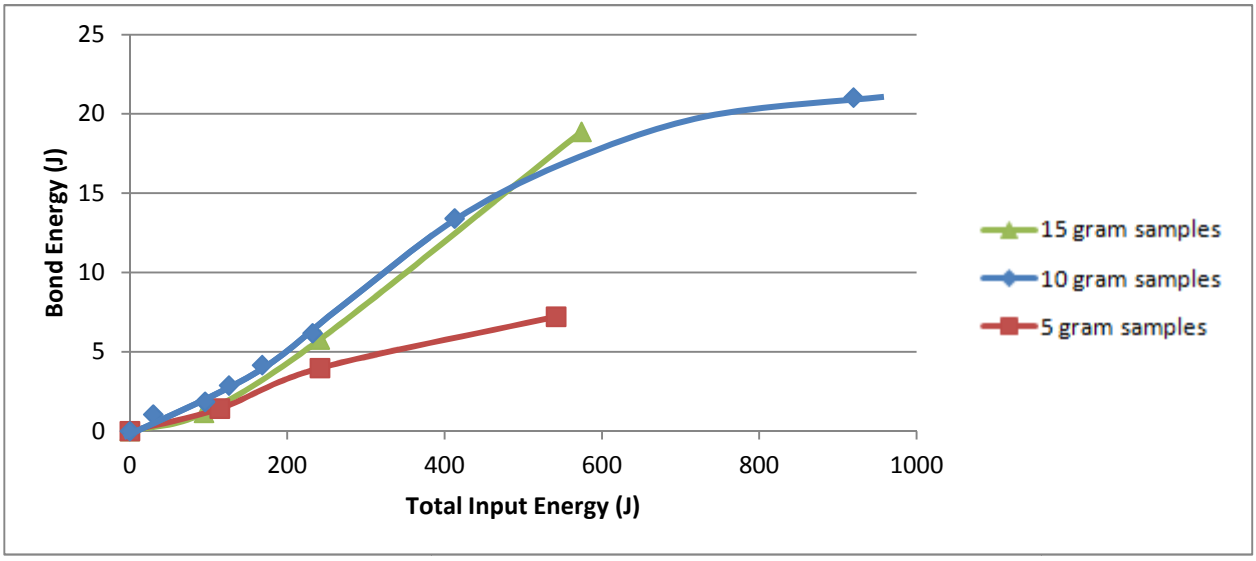

Figure 34. Bond energy as a function of total input energy for samples of various masses

Finally, Figure 35 illustrates and compares energy efficiency as a function of impact speed for samples of different mass. The trends for both series (5g samples and 15g samples) are very similar to that of the base case. However, the 5g series peaks at a lower speed (around 200 ms^{-1}) while the 15g series peaks at about 300 ms^{-1}.

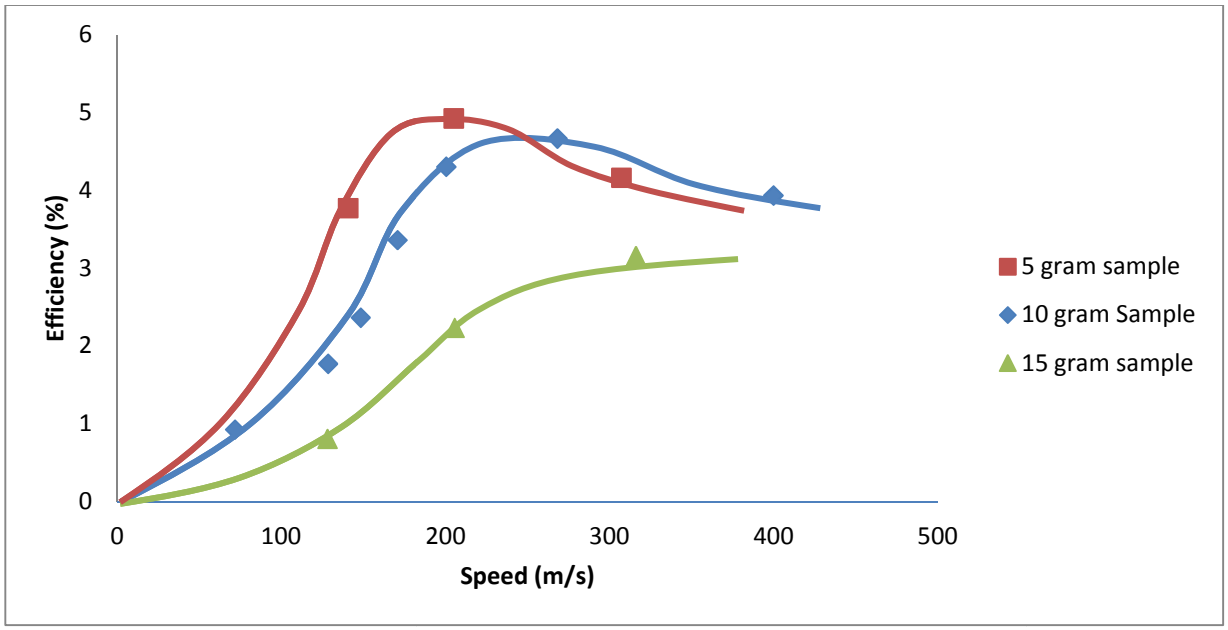

Figure 35. Comparison of energy efficiency vs. impact speed for samples of different mass

4.6 The Effect of Bullet Size and Material

This set of experiments used different size bullets so the energy input would be different for the same projectile velocity. As well, different types of bullet materials were tested to investigate further effects of bullet mass at the same velocity. By changing the size or the material of the bullet, we can investigate the effects of input energy on energy efficiency independent of velocity. A total of fourteen 10g samples with a size distribution of 1 to 2 mm were prepared. Three samples were impacted using a 25.4 mm long steel bullet, three were shot using a 6.35 mm long steel bullets, four were done using a 12.7 mm aluminum bullet and four were shot using a 12.7 mm long glass bullet.

Figure 36 shows the relationship between energy efficiency as a function of impact speed for different bullet sizes and types.

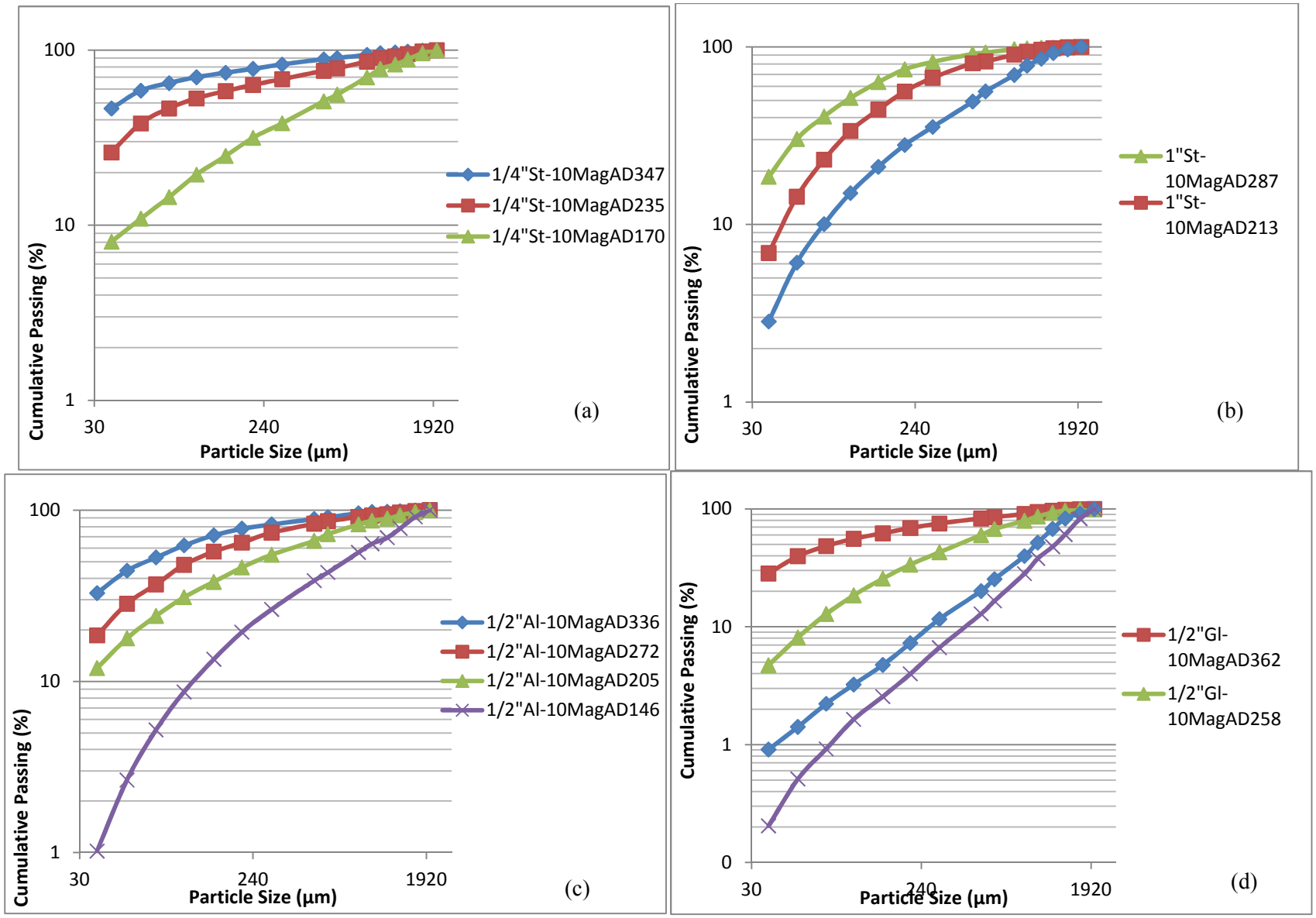

Figure 36. Size analysis for 1 to 2 mm, 10g magnetite samples impacted by a) 6.35 mm long steel bullet; b) 25.4 mm long steel bullet; c) 12.7 mm long aluminum bullet; d) 12.7 mm long glass bullet.

Table 10 summarizes the P80, Bond energy and Weight% -150 µm material in the product for each of the above experiments. As expected, for experiments using steel bullets, the amount of breakage increases when the sample is impacted by a larger bullet. For different materials, breakage with an aluminum bullet is higher than that for the glass bullet, but less than that for the steel bullet.

Table 10. P80, Bond energy, and wt% -150 µm material for 6.35mm steel, 25.4mm steel, and 12.7mm Al and glass bullets.

Sample	Speed (ms^{-1})	P80 (µm)	Bond Energy (J)	-150 µm Size Particle (Mass %)
1/4"St-10MagAD Series				
Before Impact	0	1800	0.0	0.0
1/4"St-10MagAD170	170	1078	2.8	24.9
1/4"St-10MagAD235	235	631	6.6	58.4
1/4"St-10MagAD347	347	244	16.5	74.4
1"St-10MagAD Series				
Before Impact	0	1800	0.0	0.0
1"St-10MagAD127	127	1044	3.0	21.1
1"St-10MagAD213	213	488	8.8	44.4
1"St-10MagAD287	287	273	15.0	63.3
1/2"Al-10MagAD Series				
Before Impact	0	1800	0.0	0.0
1/2"Al-10MagAD205	205	784	4.9	38.1
1/2"Al-10MagAD272	272	429	10.1	57.2
1/2"Al-10MagAD336	336	251	16.1	71.2
1/2"Gl-10MagAD Series				
Before Impact	0	1800	0.0	0.0
1/2"Gl-10MagAD152	152	1646	0.4	2.6
1/2"Gl-10MagAD195	195	1358	1.5	4.8
1/2"Gl-10MagAD258	258	862	4.3	25.7
1/2"Gl-10MagAD362	362	379	11.3	62.2

Figure 37 shows Bond energy as a function of input energy for samples impacted by different bullet types.

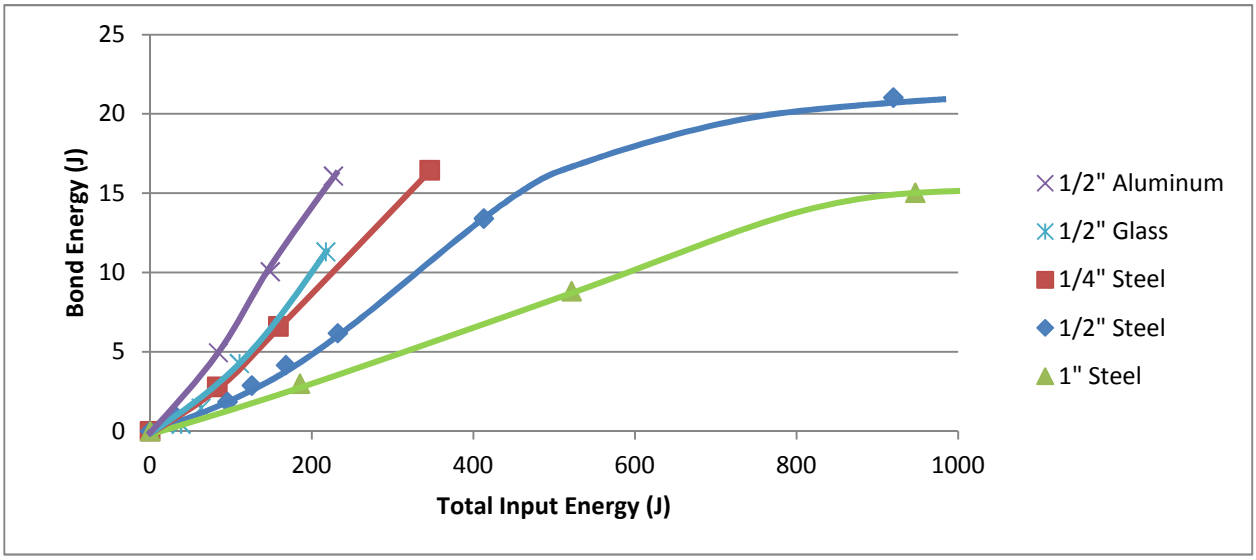

Figure 37. Comparison of Bond energy as a function of input energy for various bullet types

The relationship of energy efficiency with respect to impact speed for experiments using various bullet dimensions and materials is shown in Figure 38. As can be seen, the energy efficiency peaks at around 200 ms^{-1} for samples impacted by the 25.4 mm long steel bullet. For the 6.35 mm steel bullet, the efficiency peaks at 350 ms^{-1}. The trend and relationship between the efficiency and the impact speed seems very similar for the 6.35 mm steel bullet series and the 12.7 mm aluminum bullet series which have a similar mass. In the case of glass bullets, the efficiency is much lower than the other cases and the relationship over the range considered appears almost linear, however, the breakage of the bullet is not considered in this diagram. This will be done subsequently.

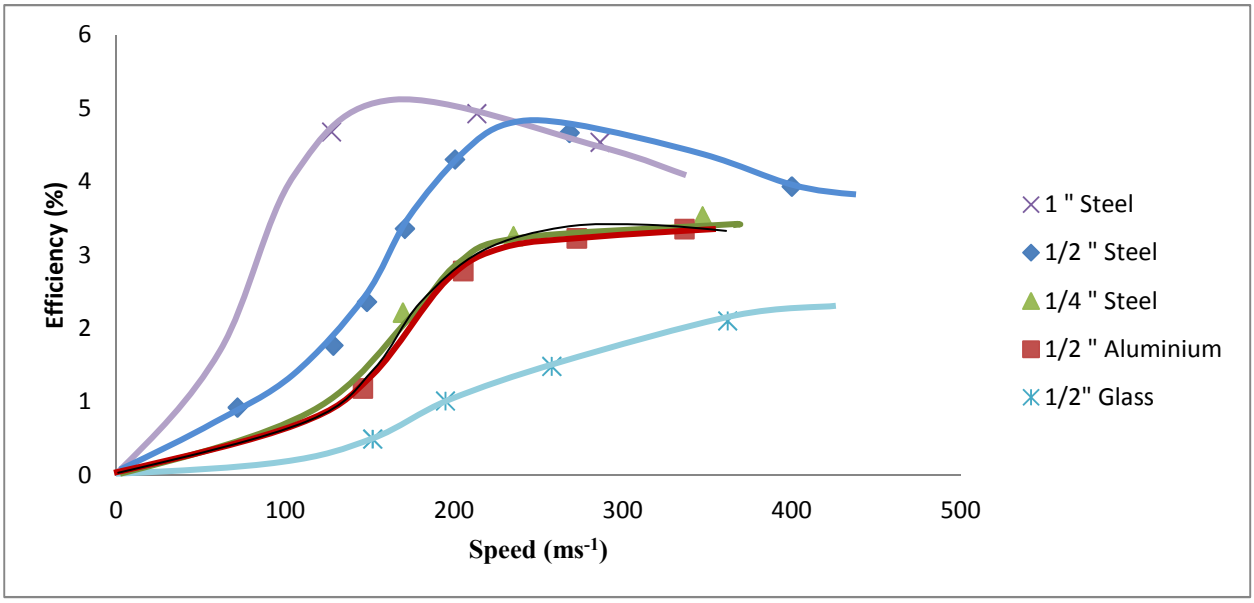

Figure 38. Comparison of energy efficiency vs. impact speed for various bullet types

The type of bullet changes the input energy since the S.G. and mass are different. Figure 39 shows the energy efficiency for the different sets of experiments as a function of input energy. As observed in this graph, experiments with similar input energy lead to similar energy efficiency, although a distinction between the trends of each set can be observed.

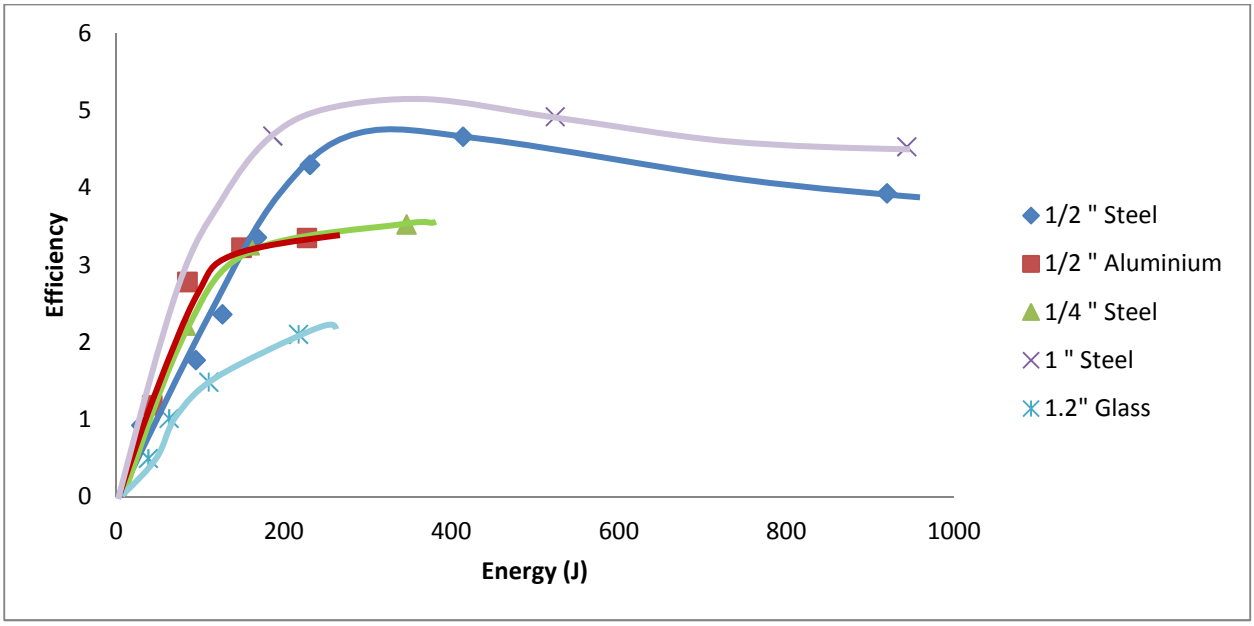

Figure 39. Comparison of energy efficiency vs. input energy for various bullet types

Special consideration must be given to the testwork with glass bullets. As a result of impacting the sample, the glass bullet also breaks and the energy recovered as new surface energy in the bullet particles can be measured. A size analysis was performed on the broken glass after impact. Figure 40 shows the results of this analysis. The trend observed here is similar to that observed for the target sample in that more breakage occurs as impact speed increases.

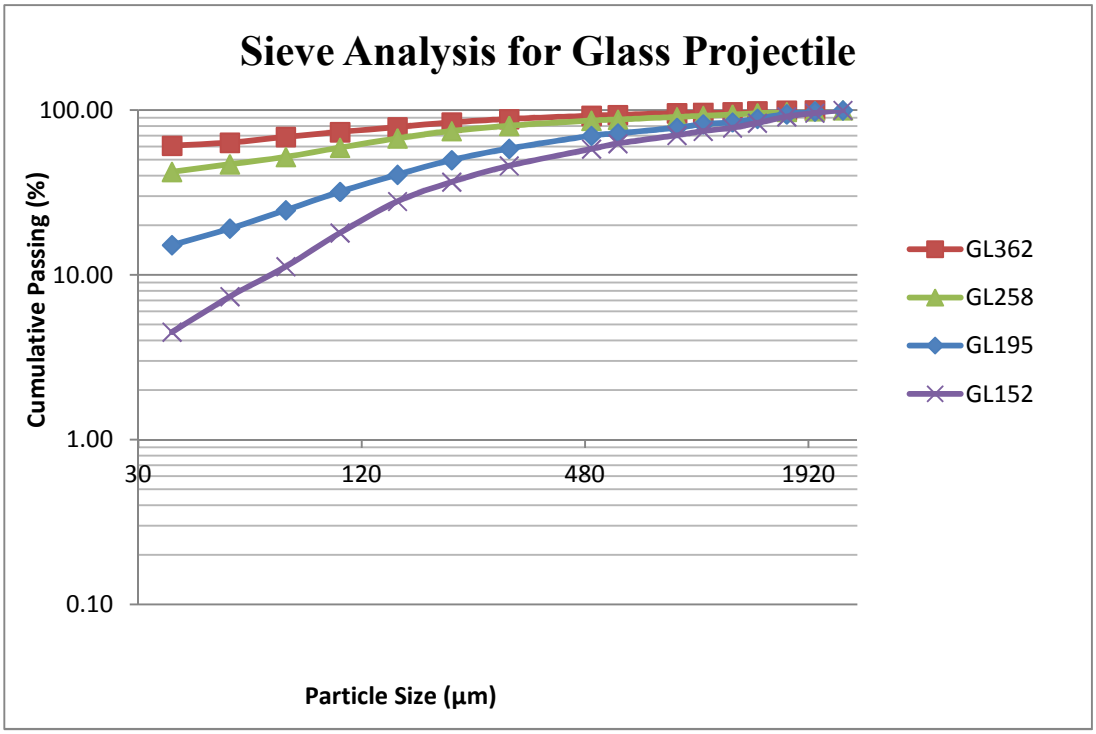

Figure 40. Sieve analysis performed on glass projectiles after impact

Figure 41 illustrates the efficiency of breakage of samples impacted by glass, the efficiency of glass breakage and the combined efficiency of the system as a function of speed Although the relationship seems linear for the case of magnetite particles impacted by glass bullets for this speed range, the overall efficiency of the system, which is the efficiency of breakage of the sample plus the efficiency of breakage of the bullet, has the same trend as a steel bullet of similar energy with a peak occurring at about 300 ms^{-1}.

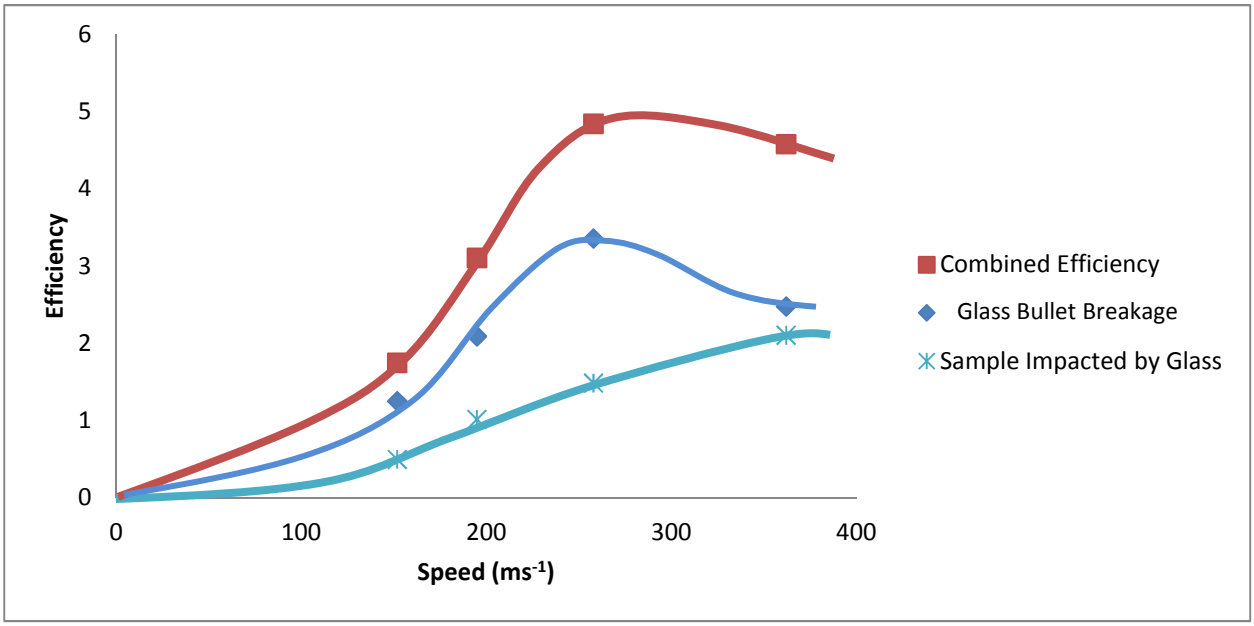

Figure 41. Efficiency as a function of impact speed for magnetite samples impacted by glass, glass bullet breakage and the total breakage efficiency

4.7 Specific Surface Area

Since the definition of efficiency depends on specific surface area, attention should be given to how this changes with particle size. Four samples impacted at various speeds were selected out of the 12.7 mm long St-MagA series. After impact, these samples were sieved into 3 portions: -37 µm, -150 µm +37 µm and +150 µm. Using the BET surface area analyzer, the specific surface areas of these fractions were measured. A similar analysis was also conducted on the sample before impact. The results of these measurements are summarized in Figure 42.

As can be seen the S.S.A. of each size fraction increases with impact velocity indicating that the surface roughness significantly changes during breakage. This suggests that attrition of ultra-fines from surface on surface interactions becomes greater as impact velocity increases.

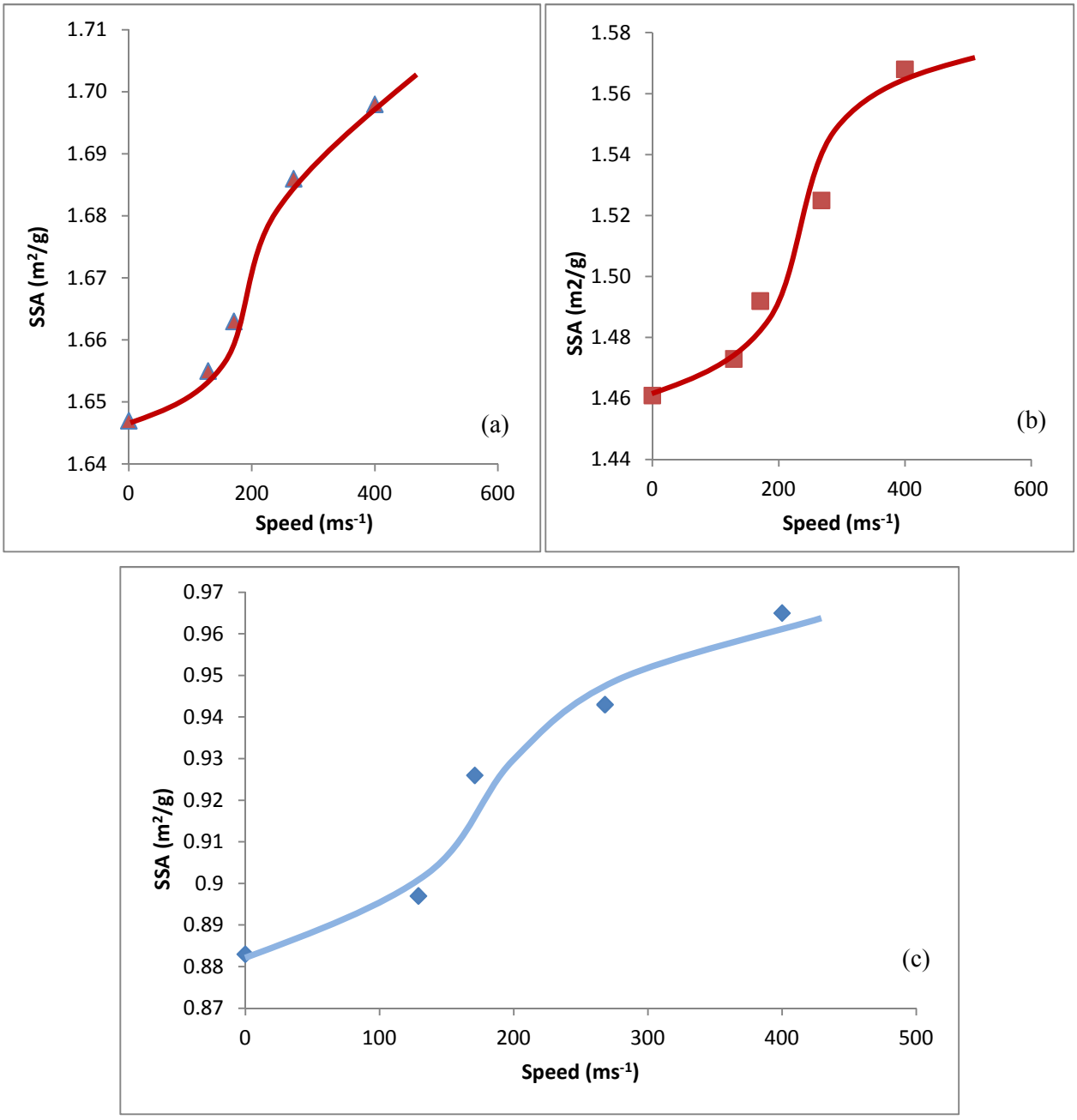

Figure 42. Specific Surface Area (SSA) as a function of impact speed for particle sizes of a) -37 µm b) -150 µm +37 µm c) +150 µm

5 DISCUSSION

5.1 Summary

This section discusses the results of the experiments conducted. The separate contribution of input energy and impact speed on improvements in energy efficiency is analyzed. The reproducibility of the results is evaluated and results are compared to those in previous work. Subsequently, an analysis is provided to describe why the energy efficiency peaks at a particular impact speed and how this peak is influenced as a function of particle size distribution and target bed depth. A discussion of the results of the rock-on-rock impact (using glass projectiles to impact magnetite samples) is also provided. Some thoughts on how these results can be used in future work are presented.

5.2 Impact Speed and Input Energy Models

The objective of this work was to find a relationship between impact speed and energy efficiency. For the base case, it was observed that energy efficiency can be increased up to about 5%. This is over 3 times the comminution efficiency of conventional equipment. Moreover, during all experiments it is shown that, as speed is increased, the energy efficiency increases to a maximum after which it drops as impact speed is further increased.

For impact speeds ranging from 100 ms^{-1} to 350 ms^{-1}, two behaviors are observed: one leading up to the peak efficiency and the second for speeds above this peak.

5.2.1 Impact Speed vs. Input Energy

One important question to consider here is "Does the enhancement in energy efficiency result from impact speed or is it a result of input energy?" Both impact speed and energy efficiency could be thought of as reasons for improvement in energy efficiency. In the case of impact speed, similar to what happens during blasting, higher impact speed introduces a shock wave that travels within the particles facilitating crack initiation and faster crack propagation. This results in more efficient breakage of particles. Likewise, in the

case of input energy, the number of internal microcracks within particles that would start propagating at the time of impact is directly related to the amount of input energy. However, these two factors may or may not contribute equally. It may even be the case that the contribution of one is insignificant or that there are other factors involved. To investigate the source of improvement in energy efficiency further, a number of experiments with various projectiles having different sizes and materials were conducted, as explained before. Comparing the results obtained from these experiments, the contribution of each of these factors can be analyzed separately. In fact, for a given speed, before the peak is reached, more massive projectiles appear to result in higher efficiencies confirming that the input energy is definitely a contributing factor in its own right. However, this observation is countered when considering the effect of input energy on energy efficiency. The graphs in Figures 43 and 44 compare the samples impacted by the 12.7 mm long aluminum projectile to those impacted by the 12.7 mm long steel projectile. For low input energy and a constant energy input, the energy efficiency is higher for the lower mass projectile meaning that impact speed may play a role independent role of energy. At higher energy input levels, the opposite is true suggesting that the effect of impact velocity increases becomes less at high energy levels.

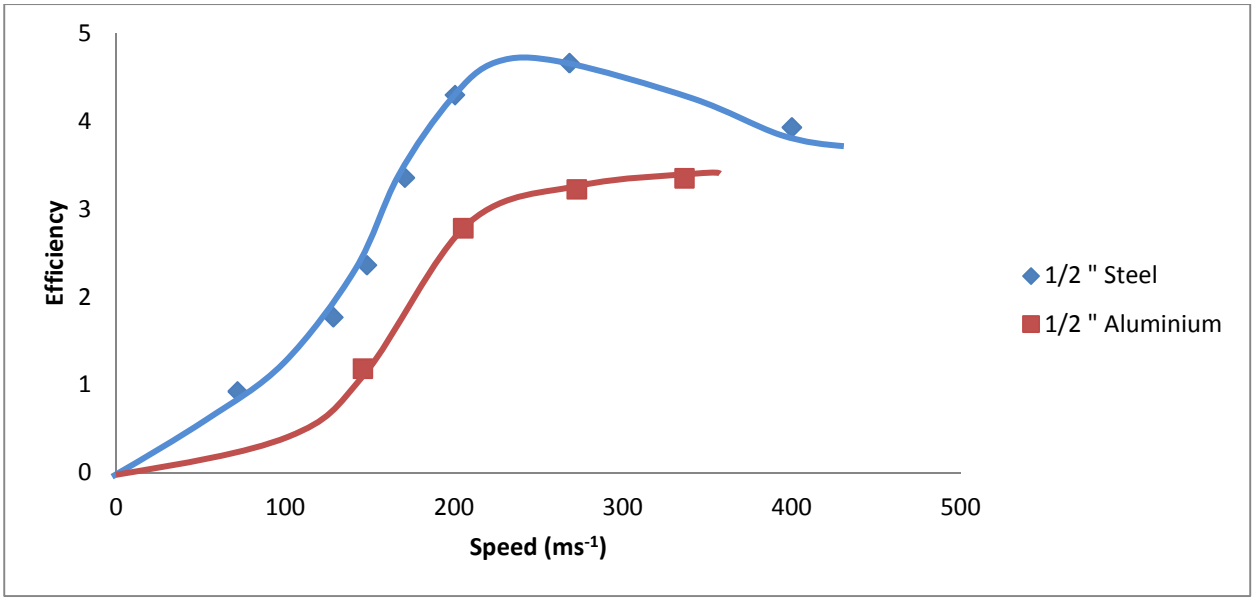

Figure 43. Comparison of energy efficiency vs. impact speed for various bullet types

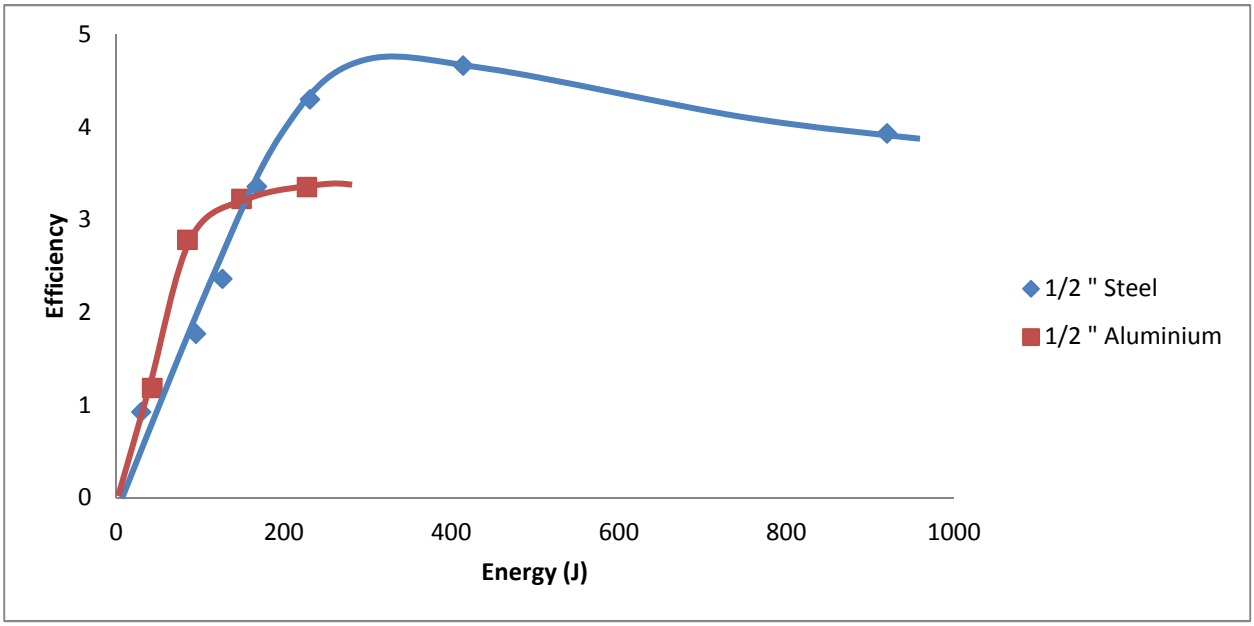

Figure 44. Comparison of energy efficiency vs. input energy for different bullet types

So although input energy and impact speed both contribute to an improved energy efficiency, their relative contributions are not necessarily equal and may change as impact speed changes.

Figure 45 has been drawn to show the family of curves that represent conditions that produce equal energy levels on the efficiency vs. speed graph for various steel projectiles. With this approach, the effects of speed and energy can be separated. The graph shows that despite what was originally expected, at constant energy level, increasing speed does not result in higher efficiencies. In fact, the efficiency obtained at a constant energy level decreases as velocity increases. This shows that the mass of the projectile is the dominant factor which results in improved efficiencies as more input energy is applied. It is important to note, however, that impact speed still has a positive effect on efficiency but through increased input energy.

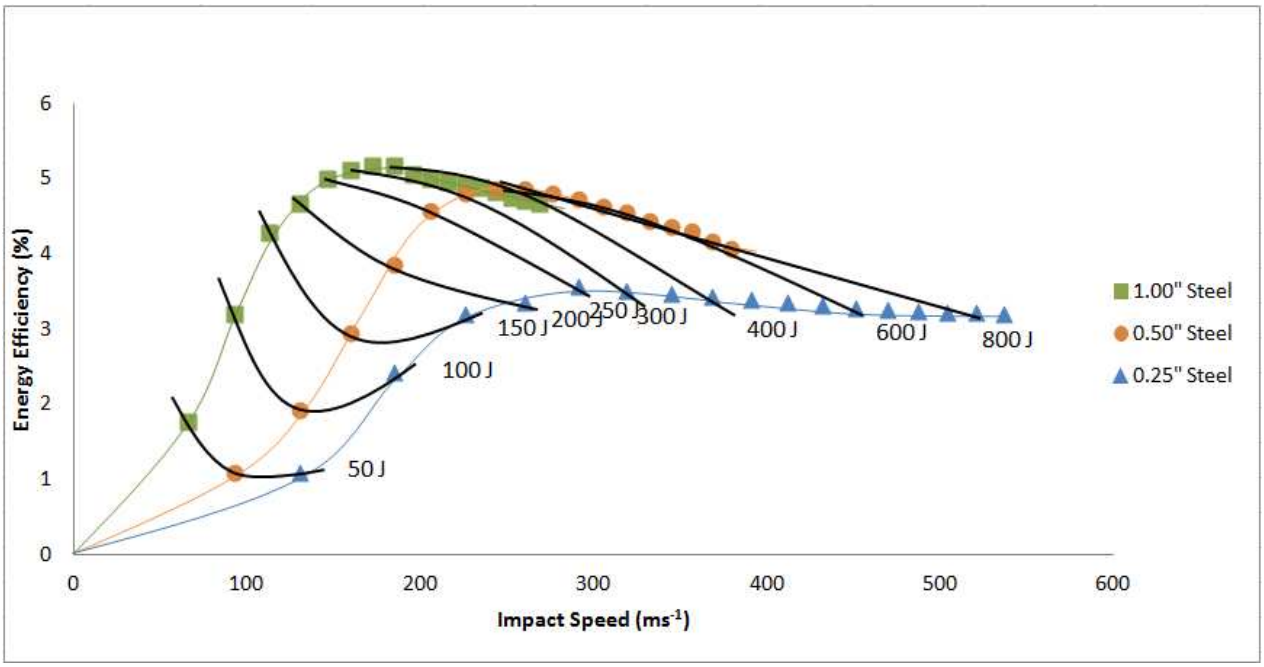

Figure 45. Energy efficiency as a function of impact velocity for various constant energy inputs.

5.2.2 Energy of the New Surface Area

To further investigate the effects of impact speed and input energy, it is important to look at the relationship between the created surface energy through impact as a function of these variables, as this is a measure of how much breakage occurs during impact.

Figure 46 plots total energy of the created surface through each experiment as a function of input energy for various projectiles impacting samples of 1-2 mm size distributions. This graph confirms that more breakage occurs (i.e. more surface area is created) as input energy increases. Moreover, this graph shows that the variations among experiments with projectiles of different masses are not significant. In other words, a particular input energy generates a particular amount of new surface area regardless of the mass and speed of the projectile.

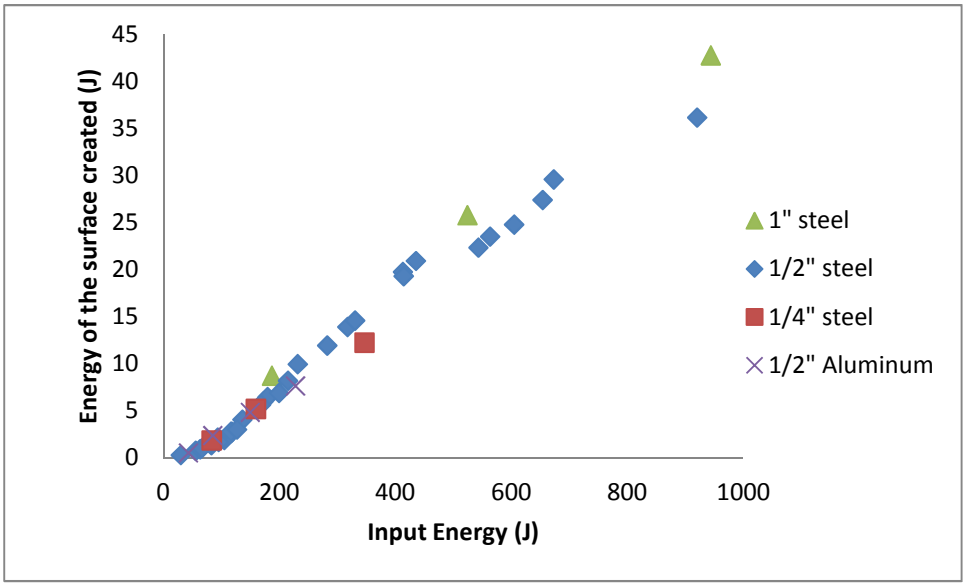

Figure 46. Graph of energy of generates surface area as a function of input energy for various bullet types

Figure 47 plots all points obtained from experiments involving samples of 1 - 2 mm size distribution on one graph. At low energy input levels, the graph is relatively flat, since very low input energies simply do not result in breakage. However as input energy increases, there comes a point at after which further increases in input energy do not produce the same efficiency and si the energy recovered begins to level off. The best fit to this data is a third order empirical polynomial equation of the form:

$$E_S = aE_{in}{}^3 + bE_{in}{}^2 + cE_{in} \qquad (2)$$

where a, b and c are three constants that change as a function of physical properties of the sample.

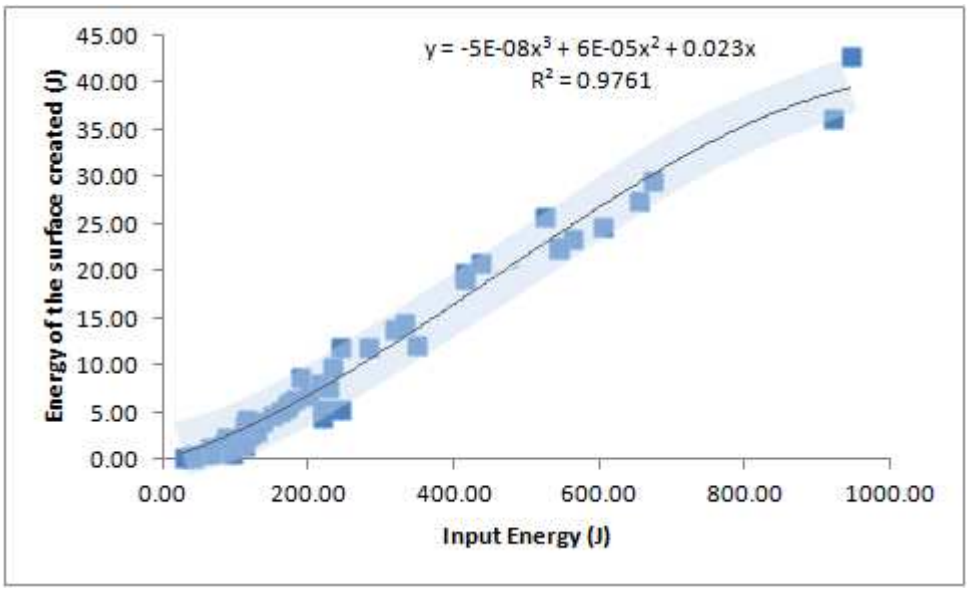

Figure 47. Polynomial fit representing energy of new surface area as a function of input energy

5.2.3 Error Minimization

Previous work reported the relationship between impact speed and energy efficiency for three minerals (rock salt, quartz and limestone). Similar to the results for magnetite samples, previous work indicated significant improvements in energy efficiency (of the order of 3 to 5%) as a function of impact speed. Moreover, it was concluded that improvement in energy efficiency was a combined effect of increased impact speed and increased input energy. The objective of this work was to ensure that a minimum error on each test was achieved with error minimized to a point where experiments are reproducible to a reliable value with the existence of a peak clearly observed. This has been achieved with an error on similar tests of ± 0.3%.

5.2.4 Reproducibility

To demonstrate the reproducibility of the results and to minimize the errors associated with having a large sample size distribution, experiments in Section 4.3 were designed. If all 26 points obtained with a sample size distribution between 1 to 2 mm (results of sections 4.2 and 4.3) are plotted on one graph (Figure 48), it

can be observed that a similar trend as those found for individual sets of experiments is found. This shows that the experimental error is very small.

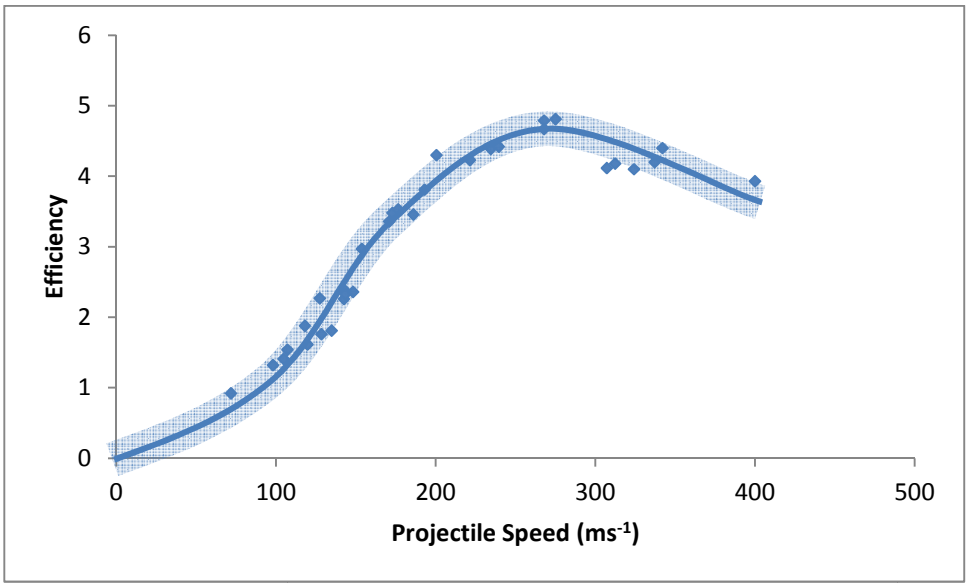

Figure 48. Reproducibility of experiments on all samples with particles between 1 to 2 mm in size impacted by steel bullets

5.3 Bond Efficiency

The Bond energy method is used widely in mining and mineral processing as an important design criterion in determining energy requirements of comminution equipment.

Figure 49 shows the graph of efficiency as calculated using the Bond equation as a function of projectile for all experiments in which steel projectiles was used to impact 1 to 2 mm samples. According to this figure, the Bond efficiency peaks at around the same speed, as well. However, the peak efficiency is only about 3%. Bond's method relies on the P80 of the sample rather than the whole size distribution. Thus, it provides no information on the amount and characteristics of fines and ultra-fines within the sample even though, the majority of the surface area of a sample is within its finer particles. For this reason, efficiency calculated using the Bond method will always be lower than one calculated using the surface area method. It is important to note that this is still a considerable improvement to efficiencies obtained in conventional equipment since typical Bond efficiencies are of the order of 1%.

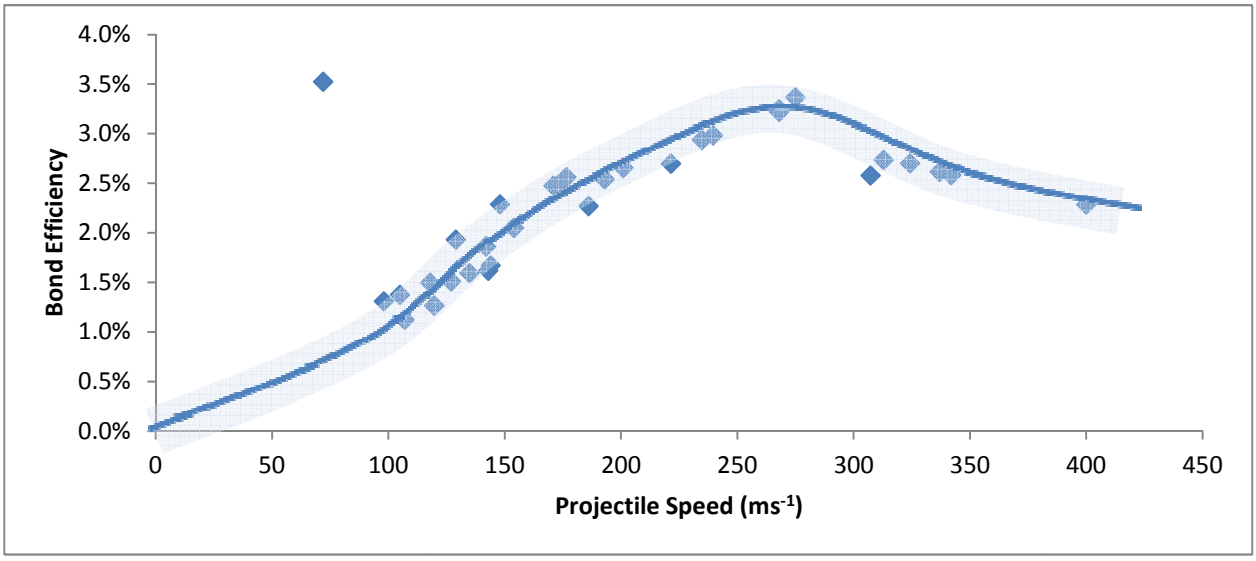

Figure 49. Bond efficiency as a function of projectile speed

5.4 The Peak

Tied to the main objectives of this study, the existence of a peak has now been clearly identified. The question now becomes, what causes this peak and can it be manipulated or eliminated? To answer this, one must consider what happens within the chamber during impact. When the projectile hits the sample particles begin to break. At the same time, the bulk material begins to compact thus reducing the void space between the particles. The existence of void space is essential to ensure free space exists for broken particles to enter. Without this space, even if enough energy is supplied that should break the particles, if the daughter particles cannot be created, the energy will simply move through the mass and dissipate as heat. As particles continue to break, the voidage space becomes filled until there is no further compaction possible. This occurs at a void space of about 22%.

The increase in input energy will improve the efficiency of breakage but up to a certain point, after which the maximum compaction for the sample is reached and more of the added input energy will dissipate as heat. This is the point at which maximum energy efficiency occurs and after which efficiency reduces as impact speed increases. However, sieve analysis results suggest that, although energy efficiency does not

improve after the peak efficiency, significant breakage still occurs. The breakage mode after the point of maximum compaction is mainly attrition, since the particles have very little void space that they can break into. So the majority of the breakage results in ultra-fine particles. As discussed previously, the finer the particles, the harder to break them because of a dirth of micro-cracks and the ever increasing loss of void space.

5.4.1 Effect of Particle Size Distribution

Experiments were conducted on samples of four distinct size distributions to investigate the effects of particle size distribution on the relationship between energy efficiency and impact speed. Results show that for finer feed particle sizes, a particular impact speed results in lower energy efficiencies. This behavior is expected because as particles get smaller, they become more resistant to breakage, since finer materials contain less inherent flaws. Moreover, as observed, the impact speed which produces the maximum efficiency is higher for finer particles. In fact, for particles finer than 300 μm (the two smallest sets) a peak is not reached within the range of the study. This is because compaction of finer particles to the limit of 22% voids requires a much higher force (or speed).

5.4.2 Effect of Sample Mass

The results for samples of various masses indicate that for a particular impact speed, the more massive the sample, the lower the obtained energy efficiency. In our experiments, changing the amount of sample changes the bed depth. This means that more mass requires much more energy input for all of its particles to break. In regards to the location of the peak, as observed, the peak is obtained at a higher velocity for heavier samples. To reach maximum compaction with more mass or a deeper bed, more input energy is required.

Figure 50 shows the graph of efficiency as a function of normalized energy (energy per sample mass). In this figure, the behavior of the 5 gram and 10 gram series are similar. For these samples, the efficiency is higher than that of 15 gram samples at a particular energy level.

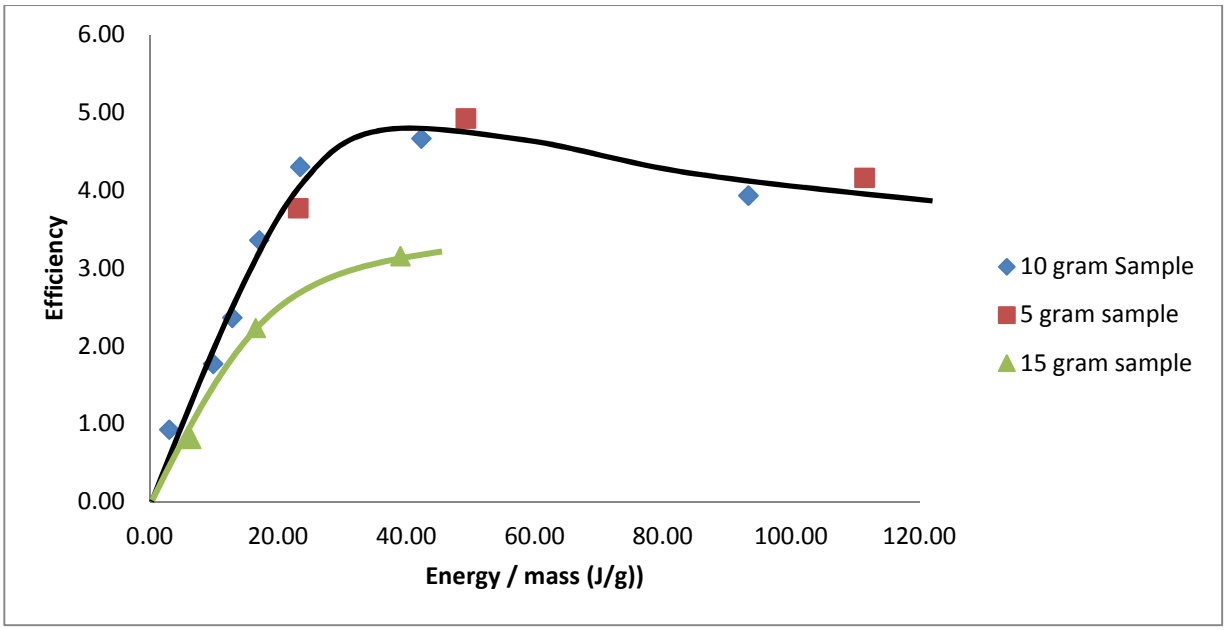

Figure 50. Efficiency as a function of energy per mass for samples of various masses

Furthermore, with further increases in impact speed, the energy efficiencies for all sets appear to converge to a similar value (~3.5%), (see Figure 35).

5.5 Rock-on-Rock Breakage

Special consideration must be given to the experiments involving glass projectiles since they provide information about rock-on-rock impact in which both target and projectile particles may break. The efficiency of fragmentation in the magnetite sample is less than that obtained when the sample is impacted by other projectiles. In addition, there was considerable breakage observed within the projectile itself. When the efficiency of the projectile breakage is combined with the efficiency of fragmentation of the sample, an overall combined energy efficiency is attained. This overall efficiency has a similar trend to the one observed in experiments where an *unbreakable* projectile is used under similar conditions.

Figure 51 compares the combined efficiency with that obtained with the base case. Although, the trends are similar, there are two main differences. First, the peak efficiency is slightly higher than that of the base case. This takes place because the energy is dissipated through breakage of the projectile during the process of compaction of the target sample. For unbreakable projectiles, all the kinetic energy applied to the projectile is dissipated as heat and sound and does not contribute to the overall breakage. Secondly, the peak efficiency occurs at a higher speed. This happens because the breakage of the projectile provides some void space for particles to break into. Hence a higher amount of input energy is required to achieve maximum compaction.

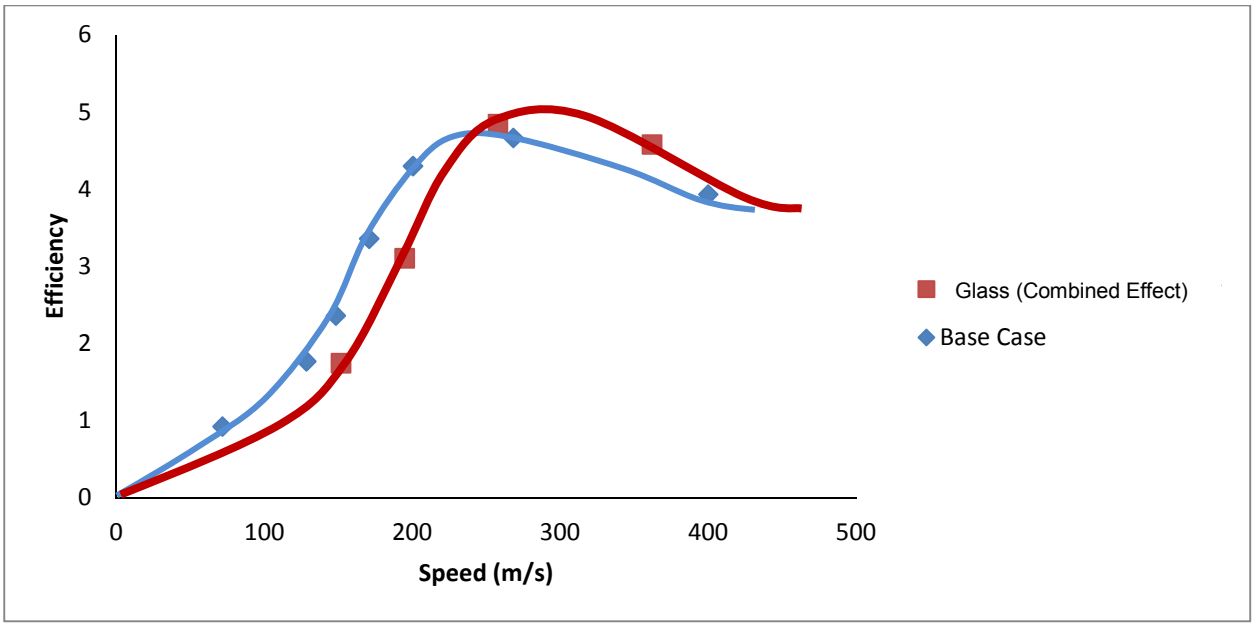

Figure 51. Comparison of the combined efficiency during impact by glass with the base case

5.6 A Modified Barmac Crusher

The main aim of this project was to investigate and prove that high impact speed results in significant improvements in energy efficiency. As a result, it was identified that there exists an impact speed at which the energy efficiency of comminution is maximized. It should be noted that providing high impact speeds itself is a very energy intensive process and may not be cost-effective. Moreover, operating costs of a

machine that provides such comminution techniques, especially in regards to wear rates, should be considered.

As this thesis is focused on investigating the relationship between comminution efficiency and impact speed and since there is no equipment in which material is impacted by speeds up to 350 ms^{-1} (other than high-pressure water jet breakage), as a thought-experiment, this section investigates the power requirements of a modified Barmac crusher which could accommodate particle impacts at these speeds. The Barmac unit was chosen as it has the attributes that could achieve such velocities without significant increase in wear rates assuming the mechanical issues of vibration can be dealt with.

The power requirements of a crusher with a cylindrical rotor of a given height (h) and diameter (D), which accelerates rock particles to a certain speed (V) at the tip of the rotor, is given by the following equation:

$$\text{Power} = \frac{\pi}{4}\rho_r h D V^3 \qquad (3)$$

where ρ_r is the density of the rotor.

Moreover, the total production of such a crusher (in tph) with a number of discharge slots (n) is given by the following equation:

$$\text{Production} = 600\pi\frac{1-f_v}{f}\rho n s_p h V \qquad (4)$$

f_v = Void fraction

f = Fraction of ore through rotor

ρ = ore density ($^{t}/_{m^3}$)

s_p = Particle size (m)

Thus, a rotor made out of steel with a diameter of 0.3 m and a height of 0.1 m will require 5 MW to accelerate particles to 300 ms^{-1}. The production for such a crusher, with 8 discharge slots, crushing 2 mm size silicate or limestone rock in which 25% of the ore goes through the rotor with a void fraction of 90%

is calculated as 850 tph. For such a system, the energy use is about 6 kWh/t. According to the general Bond equation, for material with a Bond Work Index of 12.0 kWh/t, the product size would be 150 µm. If the efficiency of crushing were to be doubled, then one would expect the product size to decrease further to 108 µm. If it were to be tripled, the product size would be 41 µm.

It should be noted that the Barmac crusher actually works on material of about 10-20 mm in size and reduces it to a P80 size of around 7 mm at a rotor tip speed of about 70 ms^{-1}. The available ratings of current Barmac crushers are very different than calculated here. For example, the B9100SE VSI crusher, manufactured by Metso (http://www.metso.com), has an installed power of 600 kW and provides a capacity of 775 tph when the tip speed is 70 ms^{-1}. The crusher has a 0.4 m rotor and is generally used to crush 10 to 20 mm size samples. However, the proposed modification is possible by replacing the rotor with a smaller one and investing in a more powerful motor.

It is also interesting to note that a typical sample size distribution after breakage using a Barmac crusher (as shown in Figure 52) is similar in shape to that obtained in our experiments at low velocities albeit at an order of magnitude difference (see Figure 21, for example).

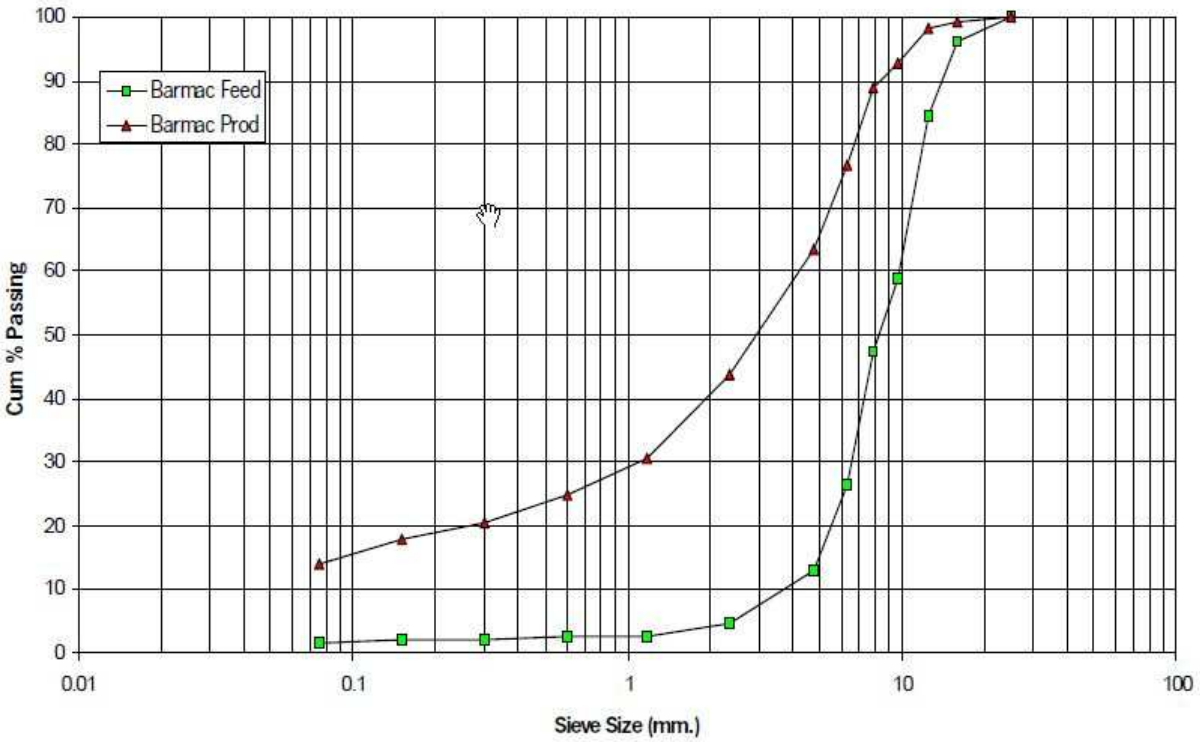

Figure 52. Size distribution of a crushed iron ore sample using a Barmac Crusher (tip speed: 63 ms^{-1}) (Metso Minerals Limited)

6 CONCLUSIONS AND RECOMMENDATIONS

This research has investigated the influence of high speed impact on rock fragmentation and energy efficiency of comminution. The separate effects of input energy and impact speed were examined. Using a high velocity impact laboratory facility, experiments on magnetite samples of various masses and size distributions, impacted by different masses and types of projectiles were performed and analyzed at projectile speeds ranging from 100 ms $^{-1}$ to 400 ms $^{-1}$. Before and after each experiment, the specific surface area of the sample was measured and the energy efficiency of breakage was calculated. The results prove that the energy efficiency of rock fragmentation can be improved to a level of 5% as a result of high speed impact.

6.1 Conclusions

The following conclusions result from this research:

- Energy efficiency in rock fragmentation can be increased to 5% in comparison to conventional comminution equipment at 1-2% through application of high-velocity impact.
- This improved efficiency results from two factors: high rate of input energy and high impact speed, both of which have significant contributions.
- The results indicate that energy efficiency peaks at an impact speed of 225 to 250 ms^{-1}. At this point the sample has been compacted to its maximum limit after which higher input energy does not result in further efficiency improvement.
- If this point of maximum compaction could be eliminated, higher efficiencies may be possible.
- The overall trend in the relationship between energy efficiency and impact speed is conserved regardless of the length of the target bed, size distribution of the sample, or type of projectile.
- The larger the length of the target bed is, the lower the efficiency of breakage at any particular impact speed.

- The smaller the size of the particles in the sample is, the lower efficiency of breakage will be at a particular speed. For example, the maximum efficiency achieved with a sample having a size of 280 μm was only 3% compared to the 5% efficiency achieved with 1.8 mm samples.
- Utilization of more massive projectiles results in higher energy efficiencies at any impact speed.
- During rock-on-rock impacts, where both particles break, higher overall efficiencies can be expected.

6.2 Future Work

The results of this research prove that high velocity impact has significant implication in mining and mineral processing. However, there is still much work to do in applying this technique to achieve the main vision of the research, i.e., to reduce energy requirements in comminution. In this section, some recommendations on the direction of the future work are outlined:

6.2.1 Enhancement of the Quality of Research

While the high velocity impact facility was central to conducting this research, there are some limitations in its use. It is recommended that improvements be done on the facility to enable studying other velocity regimes (an order of magnitude higher). The inspiration behind this work comes from what happens during blasting, but because of the limitation of the facility, we cannot study the effect of velocities higher than 400 ms^{-1}.

Moreover, during the experiments, some sample material is lost. Although, the weight percent of these particles are low, their contribution to the overall specific surface area is very significant. Essentially, most of these particles are very fine particles (or dust) that simply cannot be collected after impact. Thus, using a dust collection technique is recommended.

Probably the most important modification that could result in remarkable findings should attempt to eliminate the peak efficiency. As discussed, the existence of the peak is a result of a limitation of the

apparatus as insufficient space exists into which new particles can move into during breakage at high impact speeds. There are many ways to implement this modification and a recommendation is given in Appendix E which involves redesigning the target chamber. Elimination of the peak point where maximum compaction occurs will mean that further increases in energy efficiency may be possible at higher speeds.

Throughout the experiments, it became apparent that knowledge about how the system behaves at and immediately after the moment that the projectile comes into contact with the sample would enhance our understanding of how particle breakage occurs and how energy is expended. More specifically, identifying and monitoring the location of the projectile as a function of time would enable us to calculate how much force is exerted on the sample as comminution ensues. So, a potential improvement is to introduce a sensor to monitor the projectile as a function of time as it comes into contact with the sample.

6.2.2 Commercialization

In this research, some preliminary calculations based on Barmac crushers were performed to suggest other considerations that should be taken into account in using the results of this work. At this stage, all the results have been obtained using laboratory experiments. It is essential for other aspects of high impact comminution to be analyzed in a commercial setting. It is recommended that research and development be undertaken on how best to use the results obtained here in a commercial setting to achieve lower energy requirements.

REFERENCES

Alvarado, S., Algüerno, J., Auracher, H., & Casali, A. (1998). Energy–exergy optimization of comminution. *Energy*, *23*(2), 153-158.

Austin, L. G. (1984). Concepts in process design of mills. (Pennsylvania state univ., dep. mineral eng., INC, Ed.)*Mining engineering*, *36*(6), 628-635.

Biddulph, M. W. (1976). Principles of recycling processes. *Conservation & Recycling*, *1*(1), 31-54.

Cao Jinxi, Qin Zhiyu, Wang Guopeng, Rong Xingfu, & Yang Shichun. (2007). Investigation on Kinetic Features of Multi-Liners in Coupler Plane of Single Toggle Jaw Crusher. *2nd IEEE Conference on Industrial Electronics and Applications, 2007. ICIEA 2007* (pp. 1639-1642). Presented at the 2nd IEEE Conference on Industrial Electronics and Applications, 2007. ICIEA 2007, IEEE.

Chi, G., Fuerstenau, M. C., Bradt, R. C., & Ghosh, A. (1996). Improved comminution efficiency through controlled blasting during mining. *International Journal of Mineral Processing*, *47*(1-2), 93-101.

Cui, L., An, L., Gong, W., & Jiang, H. (2006). A novel process for preparation of ultra-clean micronized coal by high pressure water jet comminution technique. *Fuel*, *86*(5-6), 750-757.

A. Dance, 2001. Integrating the Mine-Mill Interface. Proceedings of IPMM 2001, pp.11.

A. Dance, W. Valery, A. Jankovic, D. La Rosa. and S. Esen, 2007. Maintaining the Benefit — How to Ensure Mine to Mill Continues to Work for You, 9th Mill Operators Conference, Freemantle, WA, March 19-21, 1-8.

Daniel, M. J., & Morrell, S. (2004). HPGR model verification and scale-up. *Minerals Engineering*, *17*(11-12), 1149-1161.

Donzé, F. V., Bouchez, J., & Magnier, S. A. (1997). Modeling fractures in rock blasting. *International Journal of Rock Mechanics and Mining Sciences*, *34*(8), 1153-1163.

Eloranta, J. (1995). The Selection of Powder Factor in Large Diameter Blast Holes. *Proc. Of 21st Annual Conf. On Explosives and Blasting Research.1*. Nashville, TN. 68-77.

Eloranta, J. (1997). The efficiency of blasting verses crushing and grinding. *Professional papers (blasting, mining, geology).* Retrieved from http://www.elorantaassoc.com/eob97.htm/

Formby, S. A., & Wharton, R. K. (1996). Blast characteristics and TNT equivalence values for some commercial explosives detonated at ground level. *Journal of Hazardous Materials*, *50*(2-3), 183-198.

Fourney, W. L., Dick, R. D., Wang, X. J., & Wei, Y. (1993). Fragmentation mechanism in crater blasting. *International Journal of Rock Mechanics and Mining Sciences & Geomechanics Abstracts*, *30*(4), 413-429.

Fuerstenau, D. ., & Abouzeid, A.-Z. . (2002). The energy efficiency of ball milling in comminution. *International Journal of Mineral Processing*, *67*(1-4), 161-185.

Fuerstenau, D., Daio, A., De, J., & Kapur, P. C. (1995). Fine Grinding of Coal in a Two-Stage High-Pressure Roll Mill/Ball Mill Hybrid Mode. *High Efficiency Coal Preparation: An International Symposium* (pp. 295–305). Society of Mining Engineering, Littleton.

Fuerstenau, D. W., Lutch, J. J., & De, A. (1999). The effect of ball size on the energy efficiency of hybrid high-pressure roll mill/ball mill grinding. *Powder Technology*, *105*(1-3), 199-204.

Fujimoto, S. (1994). Modern technology impact on power usage in cement plants. *IEEE Transactions on Industry Applications*, *30*(3), 553-560.

Georget, J.-P., & Lambrecht, R. (1982, November 30). Jaw crusher. Retrieved from http://www.google.dk/patents/about?id=1To2AAAAEBAJ

Hamer, M.D. (1998). Vertical Shaft impact crushes as pregrinders. In S. Atak, G. Onal, & M.S. Celik (Eds.), Innovations in Mineral and Coal Processing (pp. 73-77). Netherlands: Balkema.

Han, T., Kalman, H., & Levy, A. (2002). DEM Simulation of Particle Comminutionin Jet Milling. *Particulate Science and Technology*, *20*, 325-340.

Jankovic, A., Valery, W., & Davis, E. (2004). Cement grinding optimisation. *Minerals Engineering*, *17*(11-12), 1075-1081.

Katz, A., & Kalman, H. (2007). Preliminary Experimental Analysis of a Spiral Jet Mill Performance. *Particle & Particle Systems Characterization*, *24*(4□5), 332-338.

Lim, W. I. L., Campbell, J. J., & Tondo, L. A. (1997). The effect of rolls speed and rolls surface pattern on high pressure grinding rolls performance. *Minerals Engineering*, *10*(4), 401-419.

Lindqvist, M., & Evertsson, C. M. (2003). Liner wear in jaw crushers. *Minerals Engineering*, *16*(1), 1-12.

Major, K. (2002). Types and characteristics of crushing equipment and circuit flowsheets. *Mineral Processing Plant Design, Practice, and Control Proceedings. 1. Vancouver, BC.* Society of Mining Engineering. 566–583.

Mazurkiewicz M. (1984). High pressure liquid jet as a tool for disintegrating organic and non-organic materials. *Invention disclosure*. *85*.

McHugh, S. (1983). Crack extension caused by internal gas pressure compared with extension caused by tensile stress. *International Journal of Fracture*, *21*, 163-176.

Barmac VSI's Replace Cones for Crushing Iron Ore. *Metso Minerals (Matamata) Limited*. Retrieved from, http://www.metso.com/in/miningandconstruction/MCT_India.nsf/WebWID/WTB-110112-22577-68753/$File/aib010.pdf

Napier-Munn, T. J. (1996). *Mineral comminution circuits: their operation and optimisation*. (J. K. M. R. Centre, Ed.). Julius Kruttschnitt Mineral Research Centre.

Paley, N., and Kojovic, T. (2001). Adjusting Blasting to Increase SAG Mill Throughput at the Red Dog Mine. *Proc. of 27th Annual Conf. On Explosives and Blasting Research*. Orlando, FL.

Radziszewski, P. (2000). Developing an experimental procedure for charge media wear prediction. *Minerals Engineering*, *13*(8-9), 949-961.

Ramanujam, M., & Venkateswarlu, D. (1969). Studies in fluid energy grinding. *Powder Technology*, *3*(1), 92-101.

Rodriguez, D. E. (1990). The Tidco Barmac autogenous crushing mill- A circuit design primer. *Minerals Engineering*, *3*(1-2), 53-65.

Sadler III, L. Y., Stanley, D. A., & Brooks, D. R. (1974). Attrition mill operating characteristics. *Powder Technology*, *12*(1), 19-28.

Sadrai, S., Meech, J. A., Ghomshei, M., Sassani, F., & Tromans, D. (2006). Influence of impact velocity on fragmentation and the energy efficiency of comminution. *International Journal of Impact Engineering*, *33*(1-12), 723-734.

Sadrai, Sepehr, Meech, J. A., Tromans, D., & Sassani, F. (2011). Energy efficient comminution under high velocity impact fragmentation. *Minerals Engineering*, *24*(10), 1053-1061.

Sandvik, K. L., Fagerli, S., & Frost, T. (1999). Change from pressure crushing in roller mills to impact crushing in production of mineral sand. *Powder Technology*, *105*(1-3), 436-442.

Scheuer, A., & Ellerbrock, H.-G. (1992). Possible ways of saving energy in cement production. (Forschungsinst. Zementindustrie, DEU, Ed.) *ZKG international*, *45*(5), 222-230.

Singh, M. M., Singh, R. B., Pal Roy, P., Bagchi, A., & Dhar, B. B. (1994). An approach to improve blasting efficiency in an iron ore mine. *International Journal of Surface Mining, Reclamation and Environment*, *8*(3), 87–93. doi:10.1080/09208119408964766

Svensson, A., & Steer, J. F. (1990). New cone crusher technology and developments in comminution circuits. *Minerals Engineering*, *3*(1-2), 83-103.

Tavares, L. M. (2005). Particle weakening in high-pressure roll grinding. *Minerals Engineering*, *18*(7), 651-657.

Tromans, D, & Meech, J. . (2002). Fracture toughness and surface energies of minerals: theoretical estimates for oxides, sulphides, silicates and halides. *Minerals Engineering*, *15*(12), 1027-1041.

Tromans, D., & Meech, J. A. (2004). Fracture toughness and surface energies of covalent minerals: theoretical estimates. *Minerals Engineering*, *17*(1), 1-15.

Tuunila, R., & Nyström, L. (1998). Effects of grinding parameters on product fineness in jet mill grinding. *Minerals Engineering*, *11*(11), 1089-1094.

Vogel, A. (1991). The Alpine Fluidised Bed Opposed Jet Mill. *Powder Handling & Processing (Germany)*, *3*(2), 129–132.

Walkiewicz, J. W., Clark, A. E., & McGill, S. L. (1991). Microwave-assisted grinding. *IEEE Transactions on Industry Applications*, *27*(2), 239-243.

Whittles, D. N., Kingman, S., Lowndes, I., & Jackson, K. (2006). Laboratory and numerical investigation into the characteristics of rock fragmentation. *Minerals Engineering*, *19*(14), 1418-1429.

Workman, L., and Eloranta, J. (2003). The Effects of Blasting on Crushing and Grinding Efficiency and Energy Consumption, *Proc. Of 29th Conference on Explosives and Blasting Technique*, Nashville, TN.

APPENDIX A: EFFICIENCY CALCULATIONS

	Before Impact				After Impact				
Sample	**SSA (m^2/g)**	**Sample Mass (g)**	**Total Area (m^2)**	**Speed (m/s)**	**SSA (m^2/g)**	**Sample Mass (g)**	**Input Energy (J)**	**Total Area (m^2)**	**Efficiency (%)**
1/2"St-10MagA Series									
10MagA173	0.817	9.9958	8.1666	173.0	0.910	9.9409	172.06	9.046	3.47
10MagA177	0.813	9.9898	8.1217	176.6	0.915	9.8603	179.31	9.017	3.60
10MagA143	0.778	9.9923	7.7740	142.6	0.819	9.9874	116.86	8.180	2.26
10MagA144	0.810	9.9983	8.0986	143.5	0.853	9.9374	118.41	8.477	2.33
10MagA235	0.821	9.9983	8.2086	234.8	1.041	9.8249	317.07	10.223	4.39
10MagA240	0.808	9.9983	8.0786	239.6	1.037	9.8762	330.16	10.242	4.42
10MagA313	0.802	9.9983	8.0186	312.9	1.170	9.9032	563.09	11.590	4.18
10MagA324	0.818	9.9983	8.1786	324.3	1.207	9.8876	604.56	11.934	4.10
10MagA98	0.799	9.9983	7.9886	98.1	0.811	9.7918	55.30	7.937	1.32
10MagA105	0.822	9.9983	8.2186	104.8	0.836	9.8256	63.17	8.215	1.41
1/2"St-10MagB Series									
10MagB307	0.762	9.9962	7.6171	307.3	1.111	9.9268	542.84	11.029	4.12
10MagB222	0.793	10	7.9300	221.5	0.979	9.9491	282.14	9.740	4.23
10MagB135	0.788	9.9999	7.8799	134.9	0.818	9.7829	104.59	8.002	1.81
10MagB186	0.835	9.9875	8.3396	186.1	0.944	9.792	199.10	9.244	3.46
10MagB120	0.800	10.0017	8.0014	119.7	0.821	9.8233	82.41	8.065	1.61

Projectile mass	11.5 g
Specific Surface Energy	6.449 Jm^{-2}

	Before Impact				After Impact				
Sample	**SSA (m^2/g)**	**Sample Mass (g)**	**Total Area (m^2)**	**Speed (m/s)**	**SSA (m^2/g)**	**Sample Mass (g)**	**Input Energy (J)**	**Total Area (m^2)**	**Efficiency (%)**
1/2"St-10MagC Series									
10MagC127	0.778	10.0059	7.7846	127.4	0.812	9.6852	93.36	7.864	2.27
10MagC337	0.798	9.9925	7.9740	337.2	1.230	9.8437	653.67	12.108	4.20
10MagC154	0.756	9.9945	7.5558	153.8	0.820	9.8758	135.98	8.093	2.97
10MagC268	0.841	9.9912	8.4026	267.9	1.157	9.7138	412.63	11.234	4.79
10MagC107	0.755	9.9973	7.5480	107.2	0.771	9.8652	66.14	7.606	1.54
1/2"St-10MagD Series									
10MagD342	0.780	9.9974	7.7980	342.1	1.244	9.8947	672.89	12.309	4.40
10MagD193	0.766	9.9862	7.6494	193.1	0.897	9.6977	214.47	8.697	3.81
10MagD118	0.756	9.9995	7.5596	118.1	0.780	9.9224	80.25	7.736	1.88
10MagD142	0.820	9.987	8.1893	142.3	0.864	9.8089	116.43	8.477	2.40
10MagD275	0.778	9.9995	7.7796	275.1	1.105	9.9408	435.13	10.980	4.81
1/2"St-10MagE Series									
10MagE336	0.829	9.9996	8.2897	335.7	1.239	9.7873	647.93	12.1264647	3.99
10MagE254	0.888	9.9977	8.8780	245.4	1.097	9.7829	346.30	10.7318413	3.81
10MagE163	0.862	9.9994	8.6195	162.8	0.902	9.8287	152.44	8.8654874	1.66
1/2"St-10MagF Series									
10MagF319	1.023	10.0017	10.2317	318.8	1.333	9.9246	584.50	13.2294918	3.39
10MagF224	1.069	9.9982	10.6881	224.4	1.203	9.8333	289.67	11.8294599	2.93
10MagF171	1.024	9.9973	10.2372	170.5	1.058	9.7781	167.09	10.3452298	1.28

Projectile mass	11.5 g
Specific Surface Energy	6.449 Jm^{-2}

	Before Impact				After Impact				
Sample	**SSA (m^2/g)**	**Sample Mass (g)**	**Total Area (m^2)**	**Speed (m/s)**	**SSA (m^2/g)**	**Sample Mass (g)**	**Input Energy (J)**	**Total Area (m^2)**	**Efficiency (%)**
1/2"St-10MagG Series									
10MagG344	1.412	10.0014	14.1220	344.0	1.718	9.9563	680.50	17.1049234	2.89
10MagG176	1.362	9.9972	13.6162	176.4	1.393	9.9595	178.90	13.8735835	1.11
10MagG236	1.366	9.9992	13.6589	236.3	1.473	9.7476	321.01	14.3582148	2.10
1/2"St-10MagAD Series									
10MagAD268	0.789	9.999	7.8892	268.3	1.095	9.7877	413.94	10.718	4.67
10MagAD72	0.793	9.9991	7.9293	71.8	0.797	9.8894	29.60	7.885	0.93
10MagAD400	0.740	9.9994	7.3996	400.0	1.309	9.8616	920.00	12.909	3.93
10MagAD171	0.800	9.9988	7.9990	170.9	0.889	9.8596	167.84	8.762	3.36
10MagAD201	0.756	9.9942	7.5556	200.5	0.912	9.8873	231.21	9.017	4.30
10MagAD129	0.790	9.9983	7.8987	128.5	0.817	9.6573	94.94	7.890	1.77
10MagAD148	0.818	9.9994	8.1795	148.4	0.865	9.8752	126.62	8.542	2.36
1/2"St-15MagAD Series									
15MagAD316	0.787	15.0089	11.8120	316.2	0.978	14.7238	574.84	14.3998764	3.16
15MagAD206	0.788	15.0057	11.8245	205.7	0.845	14.774	243.22	12.48403	2.23
15MagAD128	0.803	15.0068	12.0505	128.2	0.811	14.7668	94.47	11.9758748	0.81
1/2"St-5MagAD Series									
5MagAD307	0.808	5.004	4.0436	307.3	1.527	4.8722	542.84	7.4398494	4.16
5MagAD205	0.771	5.0036	3.8578	205.1	1.147	4.9117	241.91	5.6337199	4.92
5MagAD141	0.788	5.0032	3.9425	140.7	0.923	4.9326	113.86	4.5527898	3.77

Projectile mass	11.5 g
Specific Surface Energy	6.449 Jm^{-2}

	Before Impact				After Impact				
Sample	**SSA (m^2/g)**	**Sample Mass (g)**	**Total Area (m^2)**	**Speed (m/s)**	**SSA (m^2/g)**	**Sample Mass (g)**	**Input Energy (J)**	**Total Area (m^2)**	**Efficiency (%)**
1/2"Al-10MagAD Series									
10MagAD336	0.803	9.9968	8.0274	336.4	0.924	9.78	227.49	9.037	3.35
10MagAD273	0.806	10.0012	8.0610	272.6	0.884	9.587	149.40	8.475	3.23
10MagAD205	0.776	10.0012	7.7609	205.4	0.813	9.8957	84.79	8.045	2.78
10MagAD146	0.789	10.001	7.8908	146.0	0.797	9.8387	42.83	7.841	1.19

Projectile mass	4.02 g
Specific Surface Energy	6.449 Jm^{-2}

	Before Impact				After Impact				
Sample	**SSA (m^2/g)**	**Sample Mass (g)**	**Total Area (m^2)**	**Speed (m/s)**	**SSA (m^2/g)**	**Sample Mass (g)**	**Input Energy (J)**	**Total Area (m^2)**	**Efficiency (%)**
1/4"St-10MagAD Series									
10MagAD347	0.769	10.0005	7.6904	347.2	0.961	9.8761	346.48	9.491	3.53
10MagAD235	0.801	10.0014	8.0111	235.2	0.883	9.8034	159.02	8.656	3.26
10MagAD170	0.794	10.0006	7.9405	169.7	0.823	9.8231	82.80	8.084	2.22

Projectile mass	5.75 g
Specific Surface Energy	6.449 Jm^{-2}

	Before Impact				After Impact				
Sample	**SSA (m^2/g)**	**Sample Mass (g)**	**Total Area (m^2)**	**Speed (m/s)**	**SSA (m^2/g)**	**Sample Mass (g)**	**Input Energy (J)**	**Total Area (m^2)**	**Efficiency (%)**
1"St-10MagAD Series									
10MagAD127	0.797	10.0019	7.9715	127.4	0.934	9.8829	186.73	9.231	4.68

10MagAD213	0.762	10.0006	7.6205	213.4	1.167	9.8815	523.93	11.532	4.93
10MagAD287	0.787	10.0011	7.8709	286.5	1.461	9.8476	943.72	14.387	4.54

Projectile mass	23 g
Specific Surface Energy	6.449 Jm^{-2}

	Before Impact				After Impact				
Sample	**SSA (m^2/g)**	**Sample Mass (g)**	**Total Area (m^2)**	**Speed (m/s)**	**SSA (m^2/g)**	**Sample Mass (g)**	**Input Energy (J)**	**Total Area (m^2)**	**Efficiency (%)**
1/2"Gl-10MagAD Series									
10MagAD195	0.808	10.0041	8.0833	194.9	0.818	9.9241	63.05	8.118	1.02
10MagAD362	0.796	9.9986	7.9589	362.0	0.868	9.8604	217.53	8.559	2.10
10MagAD258	0.787	10.0022	7.8717	257.9	0.813	9.7812	110.38	7.952	1.49
10MagAD152	0.792	10.0018	7.9214	151.8	0.795	9.8246	38.25	7.811	0.50

Projectile mass	3.32 g
Specific Surface Energy	6.449 Jm^{-2}

	Before Impact				After Impact				
Sample	**SSA (m^2/g)**	**Sample Mass (g)**	**Total Area (m^2)**	**Speed (m/s)**	**SSA (m^2/g)**	**Sample Mass (g)**	**Input Energy (J)**	**Total Area (m^2)**	**Efficiency (%)**
1/2"Al-10MagAD Series									
Glass195	0.000507	3.32	0.0017	194.9	0.143	3.0851	63.05	0.441	2.09
Glass362	0.000507	3.32	0.0017	362.0	0.659	2.7273	217.53	1.797	2.48
Glass258	0.000507	3.32	0.0017	257.9	0.385	3.2145	110.38	1.238	3.36
Glass152	0.000507	3.32	0.0017	151.8	0.051	3.1568	38.25	0.161	1.25

Projectile mass	3.32 g
Specific Surface Energy	6.449 Jm^{-2}

APPENDIX B: SIEVE ANALYSIS RESULTS

1/2"St-10MagA98						
US Mesh	**Size (mm)**	**Size Range (µm)**	**Passing Size (µm)**	**Weight (g)**	**Weight (%)**	**Cumulative % Passing**
16	1.200	-1400 + 1200	1400	0.00	0.00	100.00
18	1.000	-1200 + 1000	1200	2.31	23.67	100.00
20	0.850	-1000 + 850	1000	1.28	13.11	76.33
25	0.710	- 850 + 710	850	1.23	12.60	63.22
30	0.589	- 710 + 589	710	0.75	7.68	50.61
35	0.500	- 589 + 500	589	0.68	6.97	42.93
40	0.425	- 500 + 425	500	0.70	7.17	35.96
50	0.300	- 425 + 300	425	1.00	10.25	28.79
100	0.150	- 300 + 150	300	1.11	11.37	18.55
170	0.090	- 150 + 90	150	0.45	4.61	7.17
	0.000	-90	90	0.25	2.56	2.56
Total				**9.76**	**100.00**	

1/2"St-10MagA105						
US Mesh	**Size (mm)**	**Size Range (µm)**	**Passing Size (µm)**	**Weight (g)**	**Weight (%)**	**Cumulative % Passing**
16	1.200	-1400 + 1200	1400	0.00	0.00	100.00
18	1.000	-1200 + 1000	1200	2.03	20.78	100.00
20	0.850	-1000 + 850	1000	1.54	15.76	79.22
25	0.710	- 850 + 710	850	1.11	11.36	63.46
30	0.589	- 710 + 589	710	0.82	8.39	52.10
35	0.500	- 589 + 500	589	0.71	7.27	43.71
40	0.425	- 500 + 425	500	0.72	7.37	36.44
50	0.300	- 425 + 300	425	0.96	9.83	29.07
100	0.150	- 300 + 150	300	1.10	11.26	19.24
170	0.090	- 150 + 90	150	0.39	3.99	7.98
	0.000	-90	90	0.39	3.99	3.99
Total				**9.77**	**100.00**	

1/2"St-10MagA143						
US Mesh	**Size (mm)**	**Size Range (µm)**	**Passing Size (µm)**	**Weight (g)**	**Weight (%)**	**Cumulative % Passing**
16	1.200	-1400 + 1200	1400	0.00	0.00	100.00
18	1.000	-1200 + 1000	1200	0.64	6.51	100.00
20	0.850	-1000 + 850	1000	1.45	14.75	93.49
25	0.710	- 850 + 710	850	1.23	12.51	78.74
30	0.589	- 710 + 589	710	0.87	8.85	66.23
35	0.500	- 589 + 500	589	0.79	8.04	57.38
40	0.425	- 500 + 425	500	0.63	6.41	49.34
50	0.300	- 425 + 300	425	1.19	12.11	42.93
100	0.150	- 300 + 150	300	1.78	18.11	30.82
170	0.090	- 150 + 90	150	0.61	6.21	12.72
	0.000	-90	90	0.64	6.51	6.51
Total				**9.83**	**100.00**	

1/2"St-10MagA144						
US Mesh	**Size (mm)**	**Size Range (µm)**	**Passing Size (µm)**	**Weight (g)**	**Weight (%)**	**Cumulative % Passing**
16	1.200	-1400 + 1200	1400	0.00	0.00	100.00
18	1.000	-1200 + 1000	1200	0.65	6.62	100.00
20	0.850	-1000 + 850	1000	1.33	13.54	93.38
25	0.710	- 850 + 710	850	1.41	14.36	79.84
30	0.589	- 710 + 589	710	0.71	7.23	65.48
35	0.500	- 589 + 500	589	0.77	7.84	58.25
40	0.425	- 500 + 425	500	0.47	4.79	50.41
50	0.300	- 425 + 300	425	1.31	13.34	45.62
100	0.150	- 300 + 150	300	1.82	18.53	32.28
170	0.090	- 150 + 90	150	0.78	7.94	13.75
	0.000	-90	90	0.57	5.80	5.80
Total				**9.82**	**100.00**	

1/2"St-10MagA173						
US Mesh	**Size (mm)**	**Size Range (µm)**	**Passing Size (µm)**	**Weight (g)**	**Weight (%)**	**Cumulative % Passing**
16	1.200	-1400 + 1200	1400	0.00	0.00	100.00
18	1.000	-1200 + 1000	1200	0.18	1.83	100.00
20	0.850	-1000 + 850	1000	0.61	6.19	98.17
25	0.710	- 850 + 710	850	0.74	7.51	91.99
30	0.589	- 710 + 589	710	0.66	6.69	84.48
35	0.500	- 589 + 500	589	0.57	5.78	77.79
40	0.425	- 500 + 425	500	0.42	4.26	72.01
50	0.300	- 425 + 300	425	1.19	12.07	67.75
100	0.150	- 300 + 150	300	2.27	23.02	55.68
170	0.090	- 150 + 90	150	1.13	11.46	32.66
	0.000	-90	90	2.09	21.20	21.20
Total				**9.86**	**100.00**	

1/2"St-10MagA177						
US Mesh	**Size (mm)**	**Size Range (µm)**	**Passing Size (µm)**	**Weight (g)**	**Weight (%)**	**Cumulative % Passing**
16	1.200	-1400 + 1200	1400	0.00	0.00	100.00
18	1.000	-1200 + 1000	1200	0.22	2.24	100.00
20	0.850	-1000 + 850	1000	0.55	5.59	97.76
25	0.710	- 850 + 710	850	0.59	6.00	92.17
30	0.589	- 710 + 589	710	0.70	7.11	86.18
35	0.500	- 589 + 500	589	0.56	5.69	79.07
40	0.425	- 500 + 425	500	0.36	3.66	73.37
50	0.300	- 425 + 300	425	1.20	12.20	69.72
100	0.150	- 300 + 150	300	2.61	26.52	57.52
170	0.090	- 150 + 90	150	1.31	13.31	31.00
	0.000	-90	90	1.74	17.68	17.68
Total				**9.84**	**100.00**	

1/2"St-10MagA235						
US Mesh	**Size (mm)**	**Size Range (µm)**	**Passing Size (µm)**	**Weight (g)**	**Weight (%)**	**Cumulative % Passing**
16	1.200	-1400 + 1200	1400	0.00	0.00	100.00
18	1.000	-1200 + 1000	1200	0.22	2.26	100.00
20	0.850	-1000 + 850	1000	0.29	2.98	97.74
25	0.710	- 850 + 710	850	0.30	3.08	94.76
30	0.589	- 710 + 589	710	0.15	1.54	91.68
35	0.500	- 589 + 500	589	0.39	4.01	90.13
40	0.425	- 500 + 425	500	0.20	2.06	86.13
50	0.300	- 425 + 300	425	0.84	8.63	84.07
100	0.150	- 300 + 150	300	1.88	19.32	75.44
170	0.090	- 150 + 90	150	1.92	19.73	56.12
	0.000	-90	90	3.54	36.38	36.38
Total				**9.73**	**100.00**	

1/2"St-10MagA240						
US Mesh	**Size (mm)**	**Size Range (µm)**	**Passing Size (µm)**	**Weight (g)**	**Weight (%)**	**Cumulative % Passing**
16	1.200	-1400 + 1200	1400	0.00	0.00	100.00
18	1.000	-1200 + 1000	1200	0.23	2.34	100.00
20	0.850	-1000 + 850	1000	0.25	2.54	97.66
25	0.710	- 850 + 710	850	0.27	2.74	95.12
30	0.589	- 710 + 589	710	0.15	1.52	92.38
35	0.500	- 589 + 500	589	0.35	3.56	90.85
40	0.425	- 500 + 425	500	0.24	2.44	87.30
50	0.300	- 425 + 300	425	0.78	7.93	84.86
100	0.150	- 300 + 150	300	1.76	17.89	76.93
170	0.090	- 150 + 90	150	2.00	20.33	59.04
	0.000	-90	90	3.81	38.72	38.72
Total				**9.84**	**100.00**	

1/2"St-10MagA313						
US Mesh	**Size (mm)**	**Size Range (µm)**	**Passing Size (µm)**	**Weight (g)**	**Weight (%)**	**Cumulative % Passing**
16	1.200	-1400 + 1200	1400	0.00	0.00	100.00
18	1.000	-1200 + 1000	1200	0.14	1.42	100.00
20	0.850	-1000 + 850	1000	0.16	1.62	98.58
25	0.710	- 850 + 710	850	0.16	1.62	96.96
30	0.589	- 710 + 589	710	0.09	0.91	95.34
35	0.500	- 589 + 500	589	0.22	2.23	94.43
40	0.425	- 500 + 425	500	0.13	1.32	92.20
50	0.300	- 425 + 300	425	0.47	4.76	90.88
100	0.150	- 300 + 150	300	1.15	11.65	86.12
170	0.090	- 150 + 90	150	1.34	13.58	74.47
	0.000	-90	90	6.01	60.89	60.89
Total				**9.87**	**100.00**	

1/2"St-10MagA325						
US Mesh	**Size (mm)**	**Size Range (µm)**	**Passing Size (µm)**	**Weight (g)**	**Weight (%)**	**Cumulative % Passing**
16	1.200	-1400 + 1200	1400	0.00	0.00	100.00
18	1.000	-1200 + 1000	1200	0.14	1.42	100.00
20	0.850	-1000 + 850	1000	0.16	1.63	98.58
25	0.710	- 850 + 710	850	0.17	1.73	96.95
30	0.589	- 710 + 589	710	0.15	1.53	95.22
35	0.500	- 589 + 500	589	0.14	1.42	93.69
40	0.425	- 500 + 425	500	0.15	1.53	92.27
50	0.300	- 425 + 300	425	0.41	4.17	90.74
100	0.150	- 300 + 150	300	1.04	10.58	86.57
170	0.090	- 150 + 90	150	1.35	13.73	75.99
	0.000	-90	90	6.12	62.26	62.26
Total				**9.83**	**100.00**	

1/2"St-10MagB120						
US Mesh	**Size (mm)**	**Size Range (µm)**	**Passing Size (µm)**	**Weight (g)**	**Weight (%)**	**Cumulative % Passing**
14	1.400	-1680 + 1400	1680	0.00	0.00	100.00
16	1.200	-1400 + 1200	1400	1.62	16.58	100.00
18	1.000	-1200 + 1000	1200	1.03	10.54	83.42
20	0.850	-1000 + 850	1000	0.99	10.13	72.88
30	0.589	- 710 + 589	850	1.03	10.54	62.74
35	0.500	- 589 + 500	589	0.60	6.14	52.20
50	0.300	- 500 + 300	500	1.38	14.12	46.06
70	0.210	- 300 + 210	300	0.97	9.93	31.93
100	0.150	- 210 + 150	210	0.72	7.37	22.01
140	0.105	- 150 + 105	150	0.64	6.55	14.64
200	0.075	- 105 + 75	105	0.34	3.48	8.09
270	0..053	- 53 + 37	75	0.21	2.15	4.61
400	0..37	- 75 + 54	53	0.15	1.54	2.46
		-37	37	0.09	0.92	0.92
Total				**9.77**	**100.00**	

1/2"St-10MagB135						
US Mesh	**Size (mm)**	**Size Range (µm)**	**Passing Size (µm)**	**Weight (g)**	**Weight (%)**	**Cumulative % Passing**
14	1.400	-1680 + 1400	1680	0.00	0.00	100.00
16	1.200	-1400 + 1200	1400	1.22	12.55	100.00
18	1.000	-1200 + 1000	1200	0.83	8.54	87.45
20	0.850	-1000 + 850	1000	0.65	6.69	78.91
30	0.589	- 710 + 589	850	0.89	9.16	72.22
35	0.500	- 589 + 500	589	0.47	4.84	63.07
50	0.300	- 500 + 300	500	1.24	12.76	58.23
70	0.210	- 300 + 210	300	0.95	9.77	45.47
100	0.150	- 210 + 150	210	0.81	8.33	35.70
140	0.105	- 150 + 105	150	0.83	8.54	27.37
200	0.075	- 105 + 75	105	0.60	6.17	18.83
270	0..053	- 53 + 37	75	0.53	5.45	12.65
400	0..37	- 75 + 54	53	0.39	4.01	7.20
		-37	37	0.31	3.19	3.19
Total				**9.72**	**100.00**	

1/2"St-10MagB186						
US Mesh	**Size (mm)**	**Size Range (µm)**	**Passing Size (µm)**	**Weight (g)**	**Weight (%)**	**Cumulative % Passing**
14	1.400	-1680 + 1400	1680	0.00	0.00	100.00
16	1.200	-1400 + 1200	1400	0.48	4.92	100.00
18	1.000	-1200 + 1000	1200	0.39	4.00	95.08
20	0.850	-1000 + 850	1000	0.50	5.13	91.08
30	0.589	- 710 + 589	850	0.91	9.33	85.95
35	0.500	- 589 + 500	589	0.44	4.51	76.62
50	0.300	- 500 + 300	500	1.14	11.69	72.10
70	0.210	- 300 + 210	300	0.91	9.33	60.41
100	0.150	- 210 + 150	210	0.81	8.31	51.08
140	0.105	- 150 + 105	150	0.68	6.97	42.77
200	0.075	- 105 + 75	105	0.66	6.77	35.79
270	0..053	- 53 + 37	75	0.62	6.36	29.03
400	0..37	- 75 + 54	53	0.65	6.67	22.67
		-37	37	1.56	16.00	16.00
Total				**9.75**	**100.00**	

1/2"St-10MagB222						
US Mesh	**Size (mm)**	**Size Range (µm)**	**Passing Size (µm)**	**Weight (g)**	**Weight (%)**	**Cumulative % Passing**
14	1.400	-1680 + 1400	1680	0.00	0.00	100.00
16	1.200	-1400 + 1200	1400	0.30	3.04	100.00
18	1.000	-1200 + 1000	1200	0.20	2.02	96.96
20	0.850	-1000 + 850	1000	0.34	3.44	94.94
30	0.589	- 710 + 589	850	0.69	6.98	91.50
35	0.500	- 589 + 500	589	0.32	3.24	84.51
50	0.300	- 500 + 300	500	1.07	10.83	81.28
70	0.210	- 300 + 210	300	0.87	8.81	70.45
100	0.150	- 210 + 150	210	0.77	7.79	61.64
140	0.105	- 150 + 105	150	0.65	6.58	53.85
200	0.075	- 105 + 75	105	0.61	6.17	47.27
270	0..053	- 53 + 37	75	0.60	6.07	41.09
400	0..37	- 75 + 54	53	0.63	6.38	35.02
		-37	37	2.83	28.64	28.64
Total				**9.88**	**100.00**	

1/2"St-10MagB307						
US Mesh	**Size (mm)**	**Size Range (µm)**	**Passing Size (µm)**	**Weight (g)**	**Weight (%)**	**Cumulative % Passing**
14	1.400	-1680 + 1400	1680	0.00	0.00	100.00
16	1.200	-1400 + 1200	1400	0.35	3.55	100.00
18	1.000	-1200 + 1000	1200	0.17	1.72	96.45
20	0.850	-1000 + 850	1000	0.20	2.03	94.73
30	0.589	- 710 + 589	850	0.42	4.26	92.71
35	0.500	- 589 + 500	589	0.22	2.23	88.45
50	0.300	- 500 + 300	500	0.52	5.27	86.22
70	0.210	- 300 + 210	300	0.50	5.07	80.95
100	0.150	- 210 + 150	210	0.44	4.46	75.89
140	0.105	- 150 + 105	150	0.57	5.78	71.43
200	0.075	- 105 + 75	105	0.59	5.98	65.65
270	0..053	- 53 + 37	75	0.63	6.38	59.68
400	0..37	- 75 + 54	53	0.73	7.40	53.29
		-37	37	4.53	45.90	45.90
Total				**9.87**	**100.00**	

1/2"St-10MagC107						
US Mesh	**Size (mm)**	**Size Range (µm)**	**Passing Size (µm)**	**Weight (g)**	**Weight (%)**	**Cumulative % Passing**
12	1.680	-2000 + 1680	2000	0.00	0.00	100.00
14	1.400	-1680 + 1400	1680	2.00	20.73	100.00
16	1.200	-1400 + 1200	1400	1.40	14.51	79.27
18	1.000	-1200 + 1000	1200	0.70	7.25	64.77
20	0.850	-1000 + 850	1000	0.70	7.25	57.51
25	0.710	- 850 + 710	850	0.80	8.29	50.26
30	0.589	- 710 + 589	710	0.50	5.18	41.97
35	0.500	- 589 + 500	589	0.35	3.63	36.79
40	0.425	- 500 + 425	500	0.20	2.07	33.16
50	0.300	- 425 + 300	425	0.65	6.74	31.09
100	0.150	- 300 + 150	300	1.20	12.44	24.35
	0.000	-150	150	1.15	11.92	11.92
Total				**9.65**	**100.00**	

1/2"St-10MagC127						
US Mesh	**Size (mm)**	**Size Range (µm)**	**Passing Size (µm)**	**Weight (g)**	**Weight (%)**	**Cumulative % Passing**
12	1.680	-2000 + 1680	2000	0	0.00	100.00
14	1.400	-1680 + 1400	1680	0.97	10.74	100.00
16	1.200	-1400 + 1200	1400	1.13	12.51	89.26
18	1.000	-1200 + 1000	1200	0.67	7.42	76.74
20	0.850	-1000 + 850	1000	0.68	7.53	69.32
25	0.710	- 850 + 710	850	0.53	5.87	61.79
30	0.589	- 710 + 589	710	0.52	5.76	55.92
35	0.500	- 589 + 500	589	0.49	5.43	50.17
40	0.425	- 500 + 425	500	0.52	5.76	44.74
50	0.300	- 425 + 300	425	0.8	8.86	38.98
100	0.150	- 300 + 150	300	1.31	14.51	30.12
	0.000	-150	150	1.41	15.61	15.61
Total				**9.03**	**100.00**	

1/2"St-10MagC154						
US Mesh	**Size (mm)**	**Size Range (µm)**	**Passing Size (µm)**	**Weight (g)**	**Weight (%)**	**Cumulative % Passing**
12	1.680	-2000 + 1680	2000	0	0.00	100.00
14	1.400	-1680 + 1400	1680	0.62	6.47	100.00
16	1.200	-1400 + 1200	1400	0.83	8.65	93.53
18	1.000	-1200 + 1000	1200	0.45	4.69	84.88
20	0.850	-1000 + 850	1000	0.6	6.26	80.19
25	0.710	- 850 + 710	850	0.53	5.53	73.93
30	0.589	- 710 + 589	710	0.51	5.32	68.40
35	0.500	- 589 + 500	589	0.51	5.32	63.09
40	0.425	- 500 + 425	500	0.53	5.53	57.77
50	0.300	- 425 + 300	425	0.93	9.70	52.24
100	0.150	- 300 + 150	300	1.46	15.22	42.54
	0.000	-150	150	2.62	27.32	27.32
Total				**9.59**	**100.00**	

1/2"St-10MagC268						
US Mesh	**Size (mm)**	**Size Range (µm)**	**Passing Size (µm)**	**Weight (g)**	**Weight (%)**	**Cumulative % Passing**
12	1.680	-2000 + 1680	2000	0	0.00	100.00
14	1.400	-1680 + 1400	1680	0.12	1.22	100.00
16	1.200	-1400 + 1200	1400	0.22	2.24	98.78
18	1.000	-1200 + 1000	1200	0.11	1.12	96.53
20	0.850	-1000 + 850	1000	0.20	2.04	95.41
25	0.710	- 850 + 710	850	0.19	1.94	93.37
30	0.589	- 710 + 589	710	0.21	2.14	91.44
35	0.500	- 589 + 500	589	0.28	2.85	89.30
40	0.425	- 500 + 425	500	0.15	1.53	86.44
50	0.300	- 425 + 300	425	0.49	4.99	84.91
100	0.150	- 300 + 150	300	1.10	11.21	79.92
	0.000	-150	150	6.74	68.71	68.71
Total				**9.81**	**100.00**	

1/2"St-10MagC337						
US Mesh	**Size (mm)**	**Size Range (µm)**	**Passing Size (µm)**	**Weight (g)**	**Weight (%)**	**Cumulative % Passing**
12	1.680	-2000 + 1680	2000	0	0.00	100.00
14	1.400	-1680 + 1400	1680	0.12	1.23	100.00
16	1.200	-1400 + 1200	1400	0.12	1.23	98.77
18	1.000	-1200 + 1000	1200	0.12	1.23	97.53
20	0.850	-1000 + 850	1000	0.12	1.23	96.30
25	0.710	- 850 + 710	850	0.08	0.82	95.06
30	0.589	- 710 + 589	710	0.16	1.65	94.24
35	0.500	- 589 + 500	589	0.20	2.06	92.60
40	0.425	- 500 + 425	500	0.22	2.26	90.54
50	0.300	- 425 + 300	425	0.41	4.11	88.28
100	0.150	- 300 + 150	300	0.81	8.23	84.17
	0.000	-150	150	7.51	75.94	75.94
Total				**9.89**	**100.00**	

1/2"St-10MagD118						
US Mesh	**Size (mm)**	**Size Range (µm)**	**Passing Size (µm)**	**Weight (g)**	**Weight (%)**	**Cumulative % Passing**
10	2.000	-2362 + 2000	2362	0.00	0.00	100.00
12	1.680	-2000 + 1680	2000	1.16	11.76	100.00
14	1.400	-1680 + 1400	1680	1.39	14.10	88.24
16	1.200	-1400 + 1200	1400	0.98	9.94	74.14
18	1.000	-1200 + 1000	1200	0.73	7.40	64.20
20	0.850	-1000 + 850	1000	0.83	8.42	56.80
25	0.710	- 850 + 710	850	0.91	9.23	48.38
30	0.589	- 710 + 589	710	0.64	6.49	39.15
35	0.500	- 589 + 500	589	0.76	7.71	32.66
40	0.425	- 500 + 425	500	0.63	6.39	24.95
50	0.300	- 425 + 300	425	0.81	8.22	18.56
100	0.150	- 300 + 150	300	0.60	6.09	10.34
170	0.090	- 150 + 90	150	0.16	1.62	4.26
	0.000	-90	90	0.26	2.64	2.64
Total				**9.86**	**100.00**	

1/2"St-10MagD142						
US Mesh	**Size (mm)**	**Size Range (µm)**	**Passing Size (µm)**	**Weight (g)**	**Weight (%)**	**Cumulative % Passing**
10	2.000	-2362 + 2000	2362	0.00	0.00	100.00
12	1.680	-2000 + 1680	2000	0.53	5.39	100.00
14	1.400	-1680 + 1400	1680	0.96	9.80	94.61
16	1.200	-1400 + 1200	1400	0.74	7.52	84.80
18	1.000	-1200 + 1000	1200	0.50	5.07	77.29
20	0.850	-1000 + 850	1000	0.80	8.17	72.22
25	0.710	- 850 + 710	850	0.82	8.33	64.05
30	0.589	- 710 + 589	710	0.77	7.84	55.72
35	0.500	- 589 + 500	589	0.75	7.68	47.88
40	0.425	- 500 + 425	500	0.56	5.72	40.20
50	0.300	- 425 + 300	425	1.12	11.44	34.48
100	0.150	- 300 + 150	300	1.37	14.05	23.04
170	0.090	- 150 + 90	150	0.37	3.76	8.99
	0.000	-90	90	0.51	5.23	5.23
Total				**9.78**	**100.00**	

1/2"St-10MagD193						
US Mesh	**Size (mm)**	**Size Range (µm)**	**Passing Size (µm)**	**Weight (g)**	**Weight (%)**	**Cumulative % Passing**
10	2.000	-2362 + 2000	2362	0	0.00	100.00
12	1.680	-2000 + 1680	2000	0.21	2.19	100.00
14	1.400	-1680 + 1400	1680	0.43	4.48	97.81
16	1.200	-1400 + 1200	1400	0.34	3.55	93.33
18	1.000	-1200 + 1000	1200	0.27	2.82	89.78
20	0.850	-1000 + 850	1000	0.41	4.28	86.97
25	0.710	- 850 + 710	850	0.44	4.59	82.69
30	0.589	- 710 + 589	710	0.39	4.07	78.10
35	0.500	- 589 + 500	589	0.52	5.42	74.04
40	0.425	- 500 + 425	500	0.49	5.11	68.61
50	0.300	- 425 + 300	425	1.30	13.56	63.50
100	0.150	- 300 + 150	300	1.85	19.29	49.95
170	0.090	- 150 + 90	150	1.13	11.78	30.66
	0.000	-90	90	1.81	18.87	18.87
Total				**9.59**	**100.00**	

1/2"St-10MagD275						
US Mesh	**Size (mm)**	**Size Range (µm)**	**Passing Size (µm)**	**Weight (g)**	**Weight (%)**	**Cumulative % Passing**
10	2.000	-2362 + 2000	2362	0.00	0.00	100.00
12	1.680	-2000 + 1680	2000	0.03	0.30	100.00
14	1.400	-1680 + 1400	1680	0.09	0.92	99.70
16	1.200	-1400 + 1200	1400	0.08	0.81	98.79
18	1.000	-1200 + 1000	1200	0.12	1.22	97.98
20	0.850	-1000 + 850	1000	0.16	1.63	96.75
25	0.710	- 850 + 710	850	0.18	1.83	95.13
30	0.589	- 710 + 589	710	0.14	1.42	93.30
35	0.500	- 589 + 500	589	0.26	2.65	91.87
40	0.425	- 500 + 425	500	0.22	2.24	89.23
50	0.300	- 425 + 300	425	0.57	5.80	86.99
100	0.150	- 300 + 150	300	1.76	17.91	81.19
170	0.090	- 150 + 90	150	1.97	20.04	63.28
	0.000	-90	90	4.25	43.24	43.24
Total				**9.83**	**100.00**	

1/2"St-10MagD342						
US Mesh	**Size**	**Size Range**	**Passing**	**Weight (g)**	**Weight**	**Cumulative**

	(mm)	(µm)	Size (µm)		(%)	% Passing
10	2.000	-2362 + 2000	2362	0.00	0.00	100.00
12	1.680	-2000 + 1680	2000	0.02	0.20	100.00
14	1.400	-1680 + 1400	1680	0.06	0.61	99.80
16	1.200	-1400 + 1200	1400	0.07	0.71	99.19
18	1.000	-1200 + 1000	1200	0.09	0.92	98.47
20	0.850	-1000 + 850	1000	0.13	1.32	97.56
25	0.710	- 850 + 710	850	0.14	1.42	96.23
30	0.589	- 710 + 589	710	0.14	1.42	94.81
35	0.500	- 589 + 500	589	0.15	1.53	93.39
40	0.425	- 500 + 425	500	0.18	1.83	91.86
50	0.300	- 425 + 300	425	0.47	4.78	90.03
100	0.150	- 300 + 150	300	1.19	12.08	85.24
170	0.090	- 150 + 90	150	0.95	9.67	73.17
	0.000	-90	90	6.24	63.50	63.50
Total				**9.83**	**100.00**	

1/2"St-10MagAD72						
US Mesh	**Size (mm)**	**Size Range (µm)**	**Passing Size (µm)**	**Weight (g)**	**Weight (%)**	**Cumulative % Passing**
10	2.000	+ 2000		0.00	0.00	100.00
12	1.680	-2000 + 1680	2000	1.29	13.16	100.00
14	1.400	-1680 + 1400	1680	0.86	8.78	86.84
16	1.200	-1400 + 1200	1400	0.54	5.51	78.06
18	1.000	-1200 + 1000	1200	0.35	3.57	72.55
20	0.850	-1000 + 850	1000	0.33	3.37	68.98
30	0.589	- 710 + 589	850	0.71	7.24	65.61
35	0.500	- 589 + 500	589	0.50	5.10	58.37
40	0.425	- 500 + 425	500	1.15	11.73	53.27
50	0.300	- 425 + 300	425	1.61	16.43	41.53
100	0.150	- 300 + 150	300	1.59	16.22	25.10
140	0.105	- 150 + 105	150	0.53	5.41	8.88
200	0.075	- 105 + 75	105	0.23	2.35	3.47
270	0..053	- 53 + 37	75	0.07	0.71	1.12
400	0..37	- 75 + 54	53	0.02	0.20	0.41
		-37	37	0.02	0.20	0.20
Total				**9.80**	**100.00**	

1/2"St-10MagAD129						
US Mesh	**Size (mm)**	**Size Range (µm)**	**Passing Size (µm)**	**Weight (g)**	**Weight (%)**	**Cumulative % Passing**
10	2.000	+ 2000		0.00	0.00	100.00
12	1.680	-2000 + 1680	2000	0.88	9.15	100.00
14	1.400	-1680 + 1400	1680	0.72	7.48	90.85
16	1.200	-1400 + 1200	1400	0.48	4.99	83.37
18	1.000	-1200 + 1000	1200	0.34	3.53	78.38
20	0.850	-1000 + 850	1000	0.44	4.57	74.84
30	0.589	- 710 + 589	850	0.72	7.48	70.27
35	0.500	- 589 + 500	589	0.64	6.65	62.79
40	0.425	- 500 + 425	500	0.98	10.19	56.13
50	0.300	- 425 + 300	425	1.41	14.66	45.95
100	0.150	- 300 + 150	300	1.45	15.07	31.29
140	0.105	- 150 + 105	150	0.66	6.86	16.22
200	0.075	- 105 + 75	105	0.55	5.72	9.36
270	0..053	- 53 + 37	75	0.25	2.60	3.64
400	0..37	- 75 + 54	53	0.07	0.73	1.04
		-37	37	0.03	0.31	0.31
Total				**9.62**	**100.00**	

1/2"St-10MagAD148						
US Mesh	**Size (mm)**	**Size Range (µm)**	**Passing Size (µm)**	**Weight (g)**	**Weight (%)**	**Cumulative % Passing**
10	2.000	+ 2000		0.00	0.00	100.00
12	1.680	-2000 + 1680	2000	0.69	6.93	100.00
14	1.400	-1680 + 1400	1680	0.61	6.12	93.07
16	1.200	-1400 + 1200	1400	0.44	4.42	86.95
18	1.000	-1200 + 1000	1200	0.37	3.71	82.53
20	0.850	-1000 + 850	1000	0.51	5.12	78.82
30	0.589	- 710 + 589	850	0.75	7.53	73.69
35	0.500	- 589 + 500	589	0.72	7.23	66.16
40	0.425	- 500 + 425	500	0.95	9.54	58.94
50	0.300	- 425 + 300	425	1.38	13.86	49.40
100	0.150	- 300 + 150	300	1.54	15.46	35.54
140	0.105	- 150 + 105	150	0.83	8.33	20.08
200	0.075	- 105 + 75	105	0.62	6.22	11.75
270	0..053	- 53 + 37	75	0.36	3.61	5.52
400	0..37	- 75 + 54	53	0.13	1.31	1.91
		-37	37	0.06	0.60	0.60
Total				**9.96**	**100.00**	

1/2"St-10MagAD171						
US Mesh	**Size (mm)**	**Size Range (µm)**	**Passing Size (µm)**	**Weight (g)**	**Weight (%)**	**Cumulative % Passing**
10	2.000	+ 2000		0.00	0.00	100.00
12	1.680	-2000 + 1680	2000	0.37	3.77	100.00
14	1.400	-1680 + 1400	1680	0.39	3.97	96.23
16	1.200	-1400 + 1200	1400	0.34	3.46	92.26
18	1.000	-1200 + 1000	1200	0.38	3.87	88.80
20	0.850	-1000 + 850	1000	0.58	5.91	84.93
30	0.589	- 850 + 589	850	0.71	7.23	79.02
35	0.500	- 589 + 500	589	0.76	7.74	71.79
40	0.425	- 500 + 425	500	0.79	8.04	64.05
50	0.300	- 425 + 300	425	1.20	12.22	56.01
100	0.150	- 300 + 150	300	1.53	15.58	43.79
140	0.105	- 150 + 105	150	0.77	7.84	28.21
200	0.075	- 105 + 75	105	0.83	8.45	20.37
270	0..053	- 53 + 37	75	0.72	7.33	11.91
400	0..37	- 75 + 54	53	0.31	3.16	4.58
		-37	37	0.14	1.43	1.43
Total				**9.82**	**100.00**	

1/2"St-10MagAD72						
US Mesh	**Size (mm)**	**Size Range (µm)**	**Passing Size (µm)**	**Weight (g)**	**Weight (%)**	**Cumulative % Passing**
10	2.000	+ 2000		0.00	0.00	100.00
12	1.680	-2000 + 1680	2000	0.24	2.44	100.00
14	1.400	-1680 + 1400	1680	0.27	2.75	97.56
16	1.200	-1400 + 1200	1400	0.28	2.85	94.81
18	1.000	-1200 + 1000	1200	0.33	3.36	91.96
20	0.850	-1000 + 850	1000	0.43	4.37	88.61
30	0.589	- 850 + 589	850	0.59	6.00	84.23
35	0.500	- 589 + 500	589	0.63	6.41	78.23
40	0.425	- 500 + 425	500	0.66	6.71	71.82
50	0.300	- 425 + 300	425	1.01	10.27	65.11
100	0.150	- 300 + 150	300	1.51	15.36	54.83
140	0.105	- 150 + 105	150	0.98	9.97	39.47
200	0.075	- 105 + 75	105	0.91	9.26	29.50
270	0..053	- 53 + 37	75	0.77	7.83	20.24
400	0..37	- 75 + 54	53	0.53	5.39	12.41
		-37	37	0.69	7.02	7.02
Total				**9.83**	**100.00**	

1/2"St-10MagAD268						
US Mesh	**Size (mm)**	**Size Range (µm)**	**Passing Size (µm)**	**Weight (g)**	**Weight (%)**	**Cumulative % Passing**
10	2.000	+ 2000		0.00	0.00	100.00
12	1.680	-2000 + 1680	2000	0.24	2.47	100.00
14	1.400	-1680 + 1400	1680	0.16	1.64	97.53
16	1.200	-1400 + 1200	1400	0.04	0.41	95.89
18	1.000	-1200 + 1000	1200	0.06	0.62	95.48
20	0.850	-1000 + 850	1000	0.10	1.03	94.86
30	0.589	- 710 + 589	850	0.26	2.67	93.83
35	0.500	- 589 + 500	589	0.07	0.72	91.16
40	0.425	- 500 + 425	500	0.40	4.11	90.44
50	0.300	- 425 + 300	425	0.69	7.09	86.33
100	0.150	- 300 + 150	300	1.15	11.82	79.24
140	0.105	- 150 + 105	150	0.66	6.78	67.42
200	0.075	- 105 + 75	105	0.46	4.73	60.64
270	0..053	- 53 + 37	75	0.40	4.11	55.91
400	0..37	- 75 + 54	53	0.63	6.47	51.80
		-37	37	4.41	45.32	45.32
Total				**9.73**	**100.00**	

1/2"St-10MagAD400						
US Mesh	**Size (mm)**	**Size Range (µm)**	**Passing Size (µm)**	**Weight (g)**	**Weight (%)**	**Cumulative % Passing**
10	2.000	+ 2000		0.00	0.00	100.00
12	1.680	-2000 + 1680	2000	0.01	0.14	100.00
14	1.400	-1680 + 1400	1680	0.02	0.21	99.86
16	1.200	-1400 + 1200	1400	0.04	0.38	99.65
18	1.000	-1200 + 1000	1200	0.04	0.40	99.27
20	0.850	-1000 + 850	1000	0.09	0.92	98.87
30	0.589	- 710 + 589	850	0.19	1.90	97.96
35	0.500	- 589 + 500	589	0.18	1.83	96.05
40	0.425	- 500 + 425	500	0.27	2.73	94.23
50	0.300	- 425 + 300	425	0.43	4.39	91.49
100	0.150	- 300 + 150	300	0.85	8.63	87.11
140	0.105	- 150 + 105	150	0.53	5.39	78.47
200	0.075	- 105 + 75	105	0.46	4.72	73.08
270	0..053	- 53 + 37	75	0.62	6.29	68.36
400	0..37	- 75 + 54	53	0.85	8.70	62.07
		-37	37	5.22	53.37	53.37
Total				**9.79**	**100.00**	

1/4"St-10MagAD170						
US Mesh	**Size (mm)**	**Size Range (µm)**	**Passing Size (µm)**	**Weight (g)**	**Weight (%)**	**Cumulative % Passing**
10	2.000	+ 2000		0.00	0.00	100.00
12	1.680	-2000 + 1680	2000	0.37	3.78	100.00
14	1.400	-1680 + 1400	1680	0.74	7.55	96.22
16	1.200	-1400 + 1200	1400	0.57	5.82	88.67
18	1.000	-1200 + 1000	1200	0.46	4.69	82.86
20	0.850	-1000 + 850	1000	0.79	8.06	78.16
30	0.589	- 710 + 589	850	1.40	14.29	70.10
35	0.500	- 589 + 500	589	0.46	4.69	55.82
50	0.300	- 500 + 300	500	1.26	12.86	51.12
70	0.210	- 300 + 210	300	0.65	6.63	38.27
100	0.150	- 210 + 150	210	0.66	6.73	31.63
140	0.105	- 150 + 105	150	0.53	5.41	24.90
200	0.075	- 105 + 75	105	0.49	5.00	19.49
270	0..053	- 53 + 37	75	0.35	3.57	14.49
400	0..37	- 75 + 54	53	0.28	2.86	10.92
		-37	37	0.79	8.06	8.06
Total				**9.80**	**100.00**	

1/4"St-10MagAD235						
US Mesh	**Size (mm)**	**Size Range (µm)**	**Passing Size (µm)**	**Weight (g)**	**Weight (%)**	**Cumulative % Passing**
10	2.000	+ 2000		0.00	0.00	10
12	1.680	-2000 + 1680	2000	0.16	1.64	12
14	1.400	-1680 + 1400	1680	0.33	3.37	14
16	1.200	-1400 + 1200	1400	0.26	2.66	16
18	1.000	-1200 + 1000	1200	0.21	2.15	18
20	0.850	-1000 + 850	1000	0.40	4.09	20
30	0.589	- 710 + 589	850	0.71	7.26	30
35	0.500	- 589 + 500	589	0.25	2.56	35
50	0.300	- 500 + 300	500	0.78	7.98	50
70	0.210	- 300 + 210	300	0.49	5.01	70
100	0.150	- 210 + 150	210	0.48	4.91	100
140	0.105	- 150 + 105	150	0.52	5.32	140
200	0.075	- 105 + 75	105	0.64	6.54	200
270	0..053	- 53 + 37	75	0.82	8.38	270
400	0..37	- 75 + 54	53	1.18	12.07	400
		-37	37	2.55	26.07	
Total				**9.78**	**100.00**	

1/4"St-10MagAD347						
US Mesh	**Size (mm)**	**Size Range (µm)**	**Passing Size (µm)**	**Weight (g)**	**Weight (%)**	**Cumulative % Passing**
10	2.000	+ 2000		0.00	0.00	100.00
12	1.680	-2000 + 1680	2000	0.05	0.51	100.00
14	1.400	-1680 + 1400	1680	0.14	1.42	99.49
16	1.200	-1400 + 1200	1400	0.10	1.01	98.08
18	1.000	-1200 + 1000	1200	0.09	0.91	97.06
20	0.850	-1000 + 850	1000	0.22	2.23	96.15
30	0.589	- 710 + 589	850	0.37	3.74	93.93
35	0.500	- 589 + 500	589	0.14	1.42	90.18
50	0.300	- 500 + 300	500	0.58	5.87	88.77
70	0.210	- 300 + 210	300	0.46	4.66	82.89
100	0.150	- 210 + 150	210	0.38	3.85	78.24
140	0.105	- 150 + 105	150	0.43	4.35	74.39
200	0.075	- 105 + 75	105	0.51	5.16	70.04
270	0..053	- 53 + 37	75	0.61	6.17	64.88
400	0..37	- 75 + 54	53	1.21	12.25	58.70
		-37	37	4.59	46.46	46.46
Total				**9.88**	**100.00**	

1"St-10MagAD127						
US Mesh	**Size (mm)**	**Size Range (µm)**	**Passing Size (µm)**	**Weight (g)**	**Weight (%)**	**Cumulative % Passing**
10	2.000	+ 2000		0.00	0.00	100.00
12	1.680	-2000 + 1680	2000	0.31	3.14	100.00
14	1.400	-1680 + 1400	1680	0.45	4.56	96.86
16	1.200	-1400 + 1200	1400	0.65	6.59	92.29
18	1.000	-1200 + 1000	1200	0.72	7.30	85.70
20	0.850	-1000 + 850	1000	0.88	8.92	78.40
30	0.589	- 710 + 589	850	1.32	13.39	69.47
35	0.500	- 589 + 500	589	0.68	6.90	56.09
50	0.300	- 500 + 300	500	1.36	13.79	49.19
70	0.210	- 300 + 210	300	0.73	7.40	35.40
100	0.150	- 210 + 150	210	0.68	6.90	27.99
140	0.105	- 150 + 105	150	0.60	6.09	21.10
200	0.075	- 105 + 75	105	0.49	4.97	15.01
270	0..053	- 53 + 37	75	0.39	3.96	10.04
400	0..37	- 75 + 54	53	0.32	3.25	6.09
		-37	37	0.28	2.84	2.84
Total				**9.86**	**100.00**	

1"St-10MagAD213						
US Mesh	**Size (mm)**	**Size Range (µm)**	**Passing Size (µm)**	**Weight (g)**	**Weight (%)**	**Cumulative % Passing**
10	2.000	+ 2000		0.00	0.00	100.00
12	1.680	-2000 + 1680	2000	0.05	0.51	100.00
14	1.400	-1680 + 1400	1680	0.12	1.22	99.49
16	1.200	-1400 + 1200	1400	0.18	1.83	98.27
18	1.000	-1200 + 1000	1200	0.25	2.54	96.45
20	0.850	-1000 + 850	1000	0.34	3.45	93.91
30	0.589	- 710 + 589	850	0.75	7.61	90.46
35	0.500	- 589 + 500	589	0.20	2.03	82.84
50	0.300	- 500 + 300	500	1.36	13.81	80.81
70	0.210	- 300 + 210	300	1.08	10.96	67.01
100	0.150	- 210 + 150	210	1.15	11.68	56.04
140	0.105	- 150 + 105	150	1.06	10.76	44.37
200	0.075	- 105 + 75	105	1.03	10.46	33.60
270	0..053	- 53 + 37	75	0.87	8.83	23.15
400	0..37	- 75 + 54	53	0.73	7.41	14.31
		-37	37	0.68	6.90	6.90
Total				**9.85**	**100.00**	

1"St-10MagAD287						
US Mesh	**Size (mm)**	**Size Range (µm)**	**Passing Size (µm)**	**Weight (g)**	**Weight (%)**	**Cumulative % Passing**
10	2.000	+ 2000		0.00	0.00	100.00
12	1.680	-2000 + 1680	2000	0.02	0.20	100.00
14	1.400	-1680 + 1400	1680	0.05	0.51	99.80
16	1.200	-1400 + 1200	1400	0.05	0.51	99.29
18	1.000	-1200 + 1000	1200	0.07	0.71	98.78
20	0.850	-1000 + 850	1000	0.11	1.12	98.06
30	0.589	- 710 + 589	850	0.40	4.08	96.94
35	0.500	- 589 + 500	589	0.16	1.63	92.86
50	0.300	- 500 + 300	500	0.88	8.97	91.23
70	0.210	- 300 + 210	300	0.74	7.54	82.26
100	0.150	- 210 + 150	210	1.12	11.42	74.72
140	0.105	- 150 + 105	150	1.15	11.72	63.30
200	0.075	- 105 + 75	105	1.08	11.01	51.58
270	0..053	- 53 + 37	75	1.01	10.30	40.57
400	0..37	- 75 + 54	53	1.15	11.72	30.28
		-37	37	1.82	18.55	18.55
Total				**9.81**	**100.00**	

1/2"Al-10MagAD146						
US Mesh	**Size (mm)**	**Size Range (µm)**	**Passing Size (µm)**	**Weight (g)**	**Weight (%)**	**Cumulative % Passing**
10	2.000	+ 2000		0.00	0.00	100.00
12	1.680	-2000 + 1680	2000	0.84	8.57	100.00
14	1.400	-1680 + 1400	1680	1.29	13.16	91.43
16	1.200	-1400 + 1200	1400	0.90	9.18	78.27
18	1.000	-1200 + 1000	1200	0.53	5.41	69.08
20	0.850	-1000 + 850	1000	0.69	7.04	63.67
30	0.589	- 710 + 589	850	1.31	13.37	56.63
35	0.500	- 589 + 500	589	0.44	4.49	43.27
50	0.300	- 500 + 300	500	1.22	12.45	38.78
70	0.210	- 300 + 210	300	0.68	6.94	26.33
100	0.150	- 210 + 150	210	0.58	5.92	19.39
140	0.105	- 150 + 105	150	0.47	4.80	13.47
200	0.075	- 105 + 75	105	0.34	3.47	8.67
270	0..053	- 53 + 37	75	0.25	2.55	5.20
400	0..37	- 75 + 54	53	0.16	1.63	2.65
		-37	37	0.10	1.02	1.02
Total				**9.80**	**100.00**	

1/2"Al-10MagAD205						
US Mesh	**Size (mm)**	**Size Range (µm)**	**Passing Size (µm)**	**Weight (g)**	**Weight (%)**	**Cumulative % Passing**
10	2.000	+ 2000		0.00	0.00	100.00
12	1.680	-2000 + 1680	2000	0.26	2.63	100.00
14	1.400	-1680 + 1400	1680	0.40	4.05	97.37
16	1.200	-1400 + 1200	1400	0.39	3.95	93.31
18	1.000	-1200 + 1000	1200	0.25	2.53	89.36
20	0.850	-1000 + 850	1000	0.42	4.26	86.83
30	0.589	- 710 + 589	850	1.00	10.13	82.57
35	0.500	- 589 + 500	589	0.61	6.18	72.44
50	0.300	- 500 + 300	500	1.12	11.35	66.26
70	0.210	- 300 + 210	300	0.85	8.61	54.91
100	0.150	- 210 + 150	210	0.81	8.21	46.30
140	0.105	- 150 + 105	150	0.70	7.09	38.10
200	0.075	- 105 + 75	105	0.68	6.89	31.00
270	0..053	- 53 + 37	75	0.62	6.28	24.11
400	0..37	- 75 + 54	53	0.58	5.88	17.83
		-37	37	1.18	11.96	11.96
Total				**9.87**	**100.00**	

1/2"Al -10MagAD272						
US Mesh	**Size (mm)**	**Size Range (µm)**	**Passing Size (µm)**	**Weight (g)**	**Weight (%)**	**Cumulative % Passing**
10	2.000	+ 2000		0.00	0.00	100.00
12	1.680	-2000 + 1680	2000	0.12	1.26	100.00
14	1.400	-1680 + 1400	1680	0.18	1.89	98.74
16	1.200	-1400 + 1200	1400	0.22	2.31	96.86
18	1.000	-1200 + 1000	1200	0.14	1.47	94.55
20	0.850	-1000 + 850	1000	0.17	1.78	93.08
30	0.589	- 710 + 589	850	0.49	5.14	91.30
35	0.500	- 589 + 500	589	0.27	2.83	86.16
50	0.300	- 500 + 300	500	0.90	9.43	83.33
70	0.210	- 300 + 210	300	0.89	9.33	73.90
100	0.150	- 210 + 150	210	0.70	7.34	64.57
140	0.105	- 150 + 105	150	0.89	9.33	57.23
200	0.075	- 105 + 75	105	1.06	11.11	47.90
270	0..053	- 53 + 37	75	0.80	8.39	36.79
400	0..37	- 75 + 54	53	0.94	9.85	28.41
		-37	37	1.77	18.55	18.55
Total				**9.54**	**100.00**	

1/2"Al-10MagAD336						
US Mesh	**Size (mm)**	**Size Range (µm)**	**Passing Size (µm)**	**Weight (g)**	**Weight (%)**	**Cumulative % Passing**
10	2.000	+ 2000		0.00	0.00	100.00
12	1.680	-2000 + 1680	2000	0.04	0.41	100.00
14	1.400	-1680 + 1400	1680	0.10	1.02	99.59
16	1.200	-1400 + 1200	1400	0.07	0.72	98.57
18	1.000	-1200 + 1000	1200	0.05	0.51	97.85
20	0.850	-1000 + 850	1000	0.15	1.54	97.34
30	0.589	- 710 + 589	850	0.47	4.81	95.80
35	0.500	- 589 + 500	589	0.22	2.25	90.99
50	0.300	- 500 + 300	500	0.61	6.24	88.74
70	0.210	- 300 + 210	300	0.45	4.61	82.50
100	0.150	- 210 + 150	210	0.65	6.65	77.89
140	0.105	- 150 + 105	150	0.88	9.01	71.24
200	0.075	- 105 + 75	105	0.91	9.31	62.23
270	0..053	- 53 + 37	75	0.84	8.60	52.92
400	0..37	- 75 + 54	53	1.13	11.57	44.32
		-37	37	3.20	32.75	32.75
Total				**9.77**	**100.00**	

1/2"Gl -10MagAD152						
US Mesh	**Size (mm)**	**Size Range (µm)**	**Passing Size (µm)**	**Weight (g)**	**Weight (%)**	**Cumulative % Passing**
10	2.000	+ 2000		0.00	0.00	100.00
12	1.680	-2000 + 1680	2000	1.69	17.32	100.00
14	1.400	-1680 + 1400	1680	2.15	22.03	82.68
16	1.200	-1400 + 1200	1400	1.25	12.81	60.66
18	1.000	-1200 + 1000	1200	0.96	9.84	47.85
20	0.850	-1000 + 850	1000	0.95	9.73	38.01
30	0.589	- 710 + 589	850	1.14	11.68	28.28
35	0.500	- 589 + 500	589	0.36	3.69	16.60
50	0.300	- 500 + 300	500	0.61	6.25	12.91
70	0.210	- 300 + 210	300	0.26	2.66	6.66
100	0.150	- 210 + 150	210	0.14	1.43	4.00
140	0.105	- 150 + 105	150	0.09	0.92	2.56
200	0.075	- 105 + 75	105	0.07	0.72	1.64
270	0..053	- 53 + 37	75	0.04	0.41	0.92
400	0..37	- 75 + 54	53	0.03	0.31	0.51
		-37	37	0.02	0.20	0.20
Total				**9.76**	**100.00**	

1/2"Gl-10MagAD195						
US Mesh	**Size (mm)**	**Size Range (µm)**	**Passing Size (µm)**	**Weight (g)**	**Weight (%)**	**Cumulative % Passing**
10	2.000	+ 2000		0.00	0.00	100.00
12	1.680	-2000 + 1680	2000	0.87	8.81	100.00
14	1.400	-1680 + 1400	1680	0.79	8.00	91.19
16	1.200	-1400 + 1200	1400	1.52	15.38	83.20
18	1.000	-1200 + 1000	1200	1.58	15.99	67.81
20	0.850	-1000 + 850	1000	1.18	11.94	51.82
30	0.589	- 710 + 589	850	1.43	14.47	39.88
35	0.500	- 589 + 500	589	0.52	5.26	25.40
50	0.300	- 500 + 300	500	0.84	8.50	20.14
70	0.210	- 300 + 210	300	0.43	4.35	11.64
100	0.150	- 210 + 150	210	0.25	2.53	7.29
140	0.105	- 150 + 105	150	0.15	1.52	4.76
200	0.075	- 105 + 75	105	0.10	1.01	3.24
270	0..053	- 53 + 37	75	0.08	0.81	2.23
400	0..37	- 75 + 54	53	0.05	0.51	1.42
		-37	37	0.09	0.91	0.91
Total				**9.88**	**100.00**	

1/2"Gl -10MagAD258						
US Mesh	**Size (mm)**	**Size Range (µm)**	**Passing Size (µm)**	**Weight (g)**	**Weight (%)**	**Cumulative % Passing**
10	2.000	+ 2000		0.00	0.00	100.00
12	1.680	-2000 + 1680	2000	0.08	0.82	100.00
14	1.400	-1680 + 1400	1680	0.19	1.95	99.18
16	1.200	-1400 + 1200	1400	0.40	4.11	97.23
18	1.000	-1200 + 1000	1200	0.65	6.68	93.11
20	0.850	-1000 + 850	1000	0.68	6.99	86.43
30	0.589	- 710 + 589	850	1.15	11.82	79.45
35	0.500	- 589 + 500	589	0.73	7.50	67.63
50	0.300	- 500 + 300	500	1.67	17.16	60.12
70	0.210	- 300 + 210	300	0.90	9.25	42.96
100	0.150	- 210 + 150	210	0.78	8.02	33.71
140	0.105	- 150 + 105	150	0.70	7.19	25.69
200	0.075	- 105 + 75	105	0.55	5.65	18.50
270	0..053	- 53 + 37	75	0.46	4.73	12.85
400	0..37	- 75 + 54	53	0.33	3.39	8.12
		-37	37	0.46	4.73	4.73
Total				**9.73**	**100.00**	

1/2"Gl-10MagAD362						
US Mesh	**Size (mm)**	**Size Range (µm)**	**Passing Size (µm)**	**Weight (g)**	**Weight (%)**	**Cumulative % Passing**
10	2.000	+ 2000		0.00	0.00	100.00
12	1.680	-2000 + 1680	2000	0.06	0.61	100.00
14	1.400	-1680 + 1400	1680	0.10	1.02	99.39
16	1.200	-1400 + 1200	1400	0.17	1.74	98.36
18	1.000	-1200 + 1000	1200	0.23	2.35	96.63
20	0.850	-1000 + 850	1000	0.34	3.48	94.27
30	0.589	- 710 + 589	850	0.55	5.62	90.80
35	0.500	- 589 + 500	589	0.20	2.04	85.17
50	0.300	- 500 + 300	500	0.77	7.87	83.13
70	0.210	- 300 + 210	300	0.62	6.34	75.26
100	0.150	- 210 + 150	210	0.66	6.75	68.92
140	0.105	- 150 + 105	150	0.62	6.34	62.17
200	0.075	- 105 + 75	105	0.72	7.36	55.83
270	0..053	- 53 + 37	75	0.85	8.69	48.47
400	0..37	- 75 + 54	53	1.12	11.45	39.78
		-37	37	2.77	28.32	28.32
Total				**9.78**	**100.00**	

GLProjectile152						
US Mesh	**Size (mm)**	**Size Range (µm)**	**Passing Size (µm)**	**Weight (g)**	**Weight (%)**	**Cumulative % Passing**
10	2.000	+ 2000		0.12	3.86	100.00
12	1.680	-2000 + 1680	2000	0.15	4.82	96.14
14	1.400	-1680 + 1400	1680	0.24	7.72	91.32
16	1.200	-1400 + 1200	1400	0.17	5.47	83.60
18	1.000	-1200 + 1000	1200	0.11	3.54	78.14
20	0.850	-1000 + 850	1000	0.13	4.18	74.60
30	0.589	- 710 + 589	850	0.24	7.72	70.42
35	0.500	- 589 + 500	589	0.14	4.50	62.70
50	0.300	- 500 + 300	500	0.38	12.22	58.20
70	0.210	- 300 + 210	300	0.29	9.32	45.98
100	0.150	- 210 + 150	210	0.27	8.68	36.66
140	0.105	- 150 + 105	150	0.31	9.97	27.97
200	0.075	- 105 + 75	105	0.21	6.75	18.01
270	0..053	- 53 + 37	75	0.12	3.86	11.25
400	0..37	- 75 + 54	53	0.09	2.89	7.40
		-37	37	0.14	4.50	4.50
Total				**3.11**	**100.00**	

GLProjectile195						
US Mesh	**Size (mm)**	**Size Range (µm)**	**Passing Size (µm)**	**Weight (g)**	**Weight (%)**	**Cumulative % Passing**
10	2.000	+ 2000		0.04	1.34	100.00
12	1.680	-2000 + 1680	2000	0.12	3.96	98.66
14	1.400	-1680 + 1400	1680	0.18	5.94	94.70
16	1.200	-1400 + 1200	1400	0.13	4.29	88.76
18	1.000	-1200 + 1000	1200	0.07	2.31	84.47
20	0.850	-1000 + 850	1000	0.12	3.96	82.16
30	0.589	- 710 + 589	850	0.18	5.94	78.20
35	0.500	- 589 + 500	589	0.07	2.31	72.26
50	0.300	- 500 + 300	500	0.35	11.55	69.95
70	0.210	- 300 + 210	300	0.26	8.58	58.41
100	0.150	- 210 + 150	210	0.28	9.24	49.83
140	0.105	- 150 + 105	150	0.26	8.58	40.59
200	0.075	- 105 + 75	105	0.22	7.26	32.01
270	0..053	- 53 + 37	75	0.17	5.61	24.75
400	0..37	- 75 + 54	53	0.12	3.96	19.14
		-37	37	0.46	15.18	15.18
Total				**3.03**	**100.00**	

GLProjectileAD258						
US Mesh	**Size (mm)**	**Size Range (µm)**	**Passing Size (µm)**	**Weight (g)**	**Weight (%)**	**Cumulative % Passing**
10	2.000	+ 2000		0.03	0.95	100.00
12	1.680	-2000 + 1680	2000	0.04	1.26	99.05
14	1.400	-1680 + 1400	1680	0.06	1.89	97.79
16	1.200	-1400 + 1200	1400	0.06	1.89	95.90
18	1.000	-1200 + 1000	1200	0.05	1.58	94.01
20	0.850	-1000 + 850	1000	0.05	1.58	92.43
30	0.589	- 710 + 589	850	0.10	3.15	90.85
35	0.500	- 589 + 500	589	0.04	1.26	87.70
50	0.300	- 500 + 300	500	0.19	5.99	86.44
70	0.210	- 300 + 210	300	0.18	5.68	80.44
100	0.150	- 210 + 150	210	0.23	7.26	74.76
140	0.105	- 150 + 105	150	0.26	8.20	67.51
200	0.075	- 105 + 75	105	0.23	7.26	59.31
270	0..053	- 53 + 37	75	0.16	5.05	52.05
400	0..37	- 75 + 54	53	0.15	4.73	47.00
		-37	37	1.34	42.27	42.27
Total				**3.17**	**100.00**	

GLProjectile362						
US Mesh	**Size (mm)**	**Size Range (µm)**	**Passing Size (µm)**	**Weight (g)**	**Weight (%)**	**Cumulative % Passing**
10	2.000	+ 2000		0.00	0.00	100.00
12	1.680	-2000 + 1680	2000	0.01	0.38	100.00
14	1.400	-1680 + 1400	1680	0.03	1.13	99.62
16	1.200	-1400 + 1200	1400	0.03	1.13	98.50
18	1.000	-1200 + 1000	1200	0.02	0.75	97.37
20	0.850	-1000 + 850	1000	0.02	0.75	96.62
30	0.589	- 710 + 589	850	0.06	2.26	95.86
35	0.500	- 589 + 500	589	0.03	1.13	93.61
50	0.300	- 500 + 300	500	0.11	4.14	92.48
70	0.210	- 300 + 210	300	0.11	4.14	88.35
100	0.150	- 210 + 150	210	0.14	5.26	84.21
140	0.105	- 150 + 105	150	0.14	5.26	78.95
200	0.075	- 105 + 75	105	0.13	4.89	73.68
270	0..053	- 53 + 37	75	0.14	5.26	68.80
400	0..37	- 75 + 54	53	0.07	2.63	63.53
		-37	37	1.62	60.90	60.90
Total				**2.66**	**100.00**	

1/2"St-5MagAD141						
US Mesh	**Size (mm)**	**Size Range (µm)**	**Passing Size (µm)**	**Weight (g)**	**Weight (%)**	**Cumulative % Passing**
10	2.000	+ 2000		0.00	0.00	100.00
12	1.680	-2000 + 1680	2000	0.27	5.56	100.00
14	1.400	-1680 + 1400	1680	0.23	4.73	94.44
16	1.200	-1400 + 1200	1400	0.30	6.17	89.71
18	1.000	-1200 + 1000	1200	0.26	5.35	83.54
20	0.850	-1000 + 850	1000	0.27	5.56	78.19
30	0.589	- 710 + 589	850	0.51	10.49	72.63
35	0.500	- 589 + 500	589	0.20	4.12	62.14
50	0.300	- 500 + 300	500	0.50	10.29	58.02
70	0.210	- 300 + 210	300	0.36	7.41	47.74
100	0.150	- 210 + 150	210	0.35	7.20	40.33
140	0.105	- 150 + 105	150	0.36	7.41	33.13
200	0.075	- 105 + 75	105	0.31	6.38	25.72
270	0..053	- 53 + 37	75	0.32	6.58	19.34
400	0..37	- 75 + 54	53	0.27	5.56	12.76
		-37	37	0.35	7.20	7.20
Total				**4.86**	**100.00**	

1/2"St-5MagAD205						
US Mesh	**Size (mm)**	**Size Range (µm)**	**Passing Size (µm)**	**Weight (g)**	**Weight (%)**	**Cumulative % Passing**
10	2.000	+ 2000		0.00	0.00	100.00
12	1.680	-2000 + 1680	2000	0.01	0.21	100.00
14	1.400	-1680 + 1400	1680	0.12	2.48	99.79
16	1.200	-1400 + 1200	1400	0.10	2.07	97.31
18	1.000	-1200 + 1000	1200	0.08	1.66	95.24
20	0.850	-1000 + 850	1000	0.16	3.31	93.58
30	0.589	- 710 + 589	850	0.41	8.49	90.27
35	0.500	- 589 + 500	589	0.15	3.11	81.78
50	0.300	- 500 + 300	500	0.65	13.46	78.67
70	0.210	- 300 + 210	300	0.44	9.11	65.22
100	0.150	- 210 + 150	210	0.48	9.94	56.11
140	0.105	- 150 + 105	150	0.46	9.52	46.17
200	0.075	- 105 + 75	105	0.53	10.97	36.65
270	0..053	- 53 + 37	75	0.42	8.70	25.67
400	0..37	- 75 + 54	53	0.37	7.66	16.98
		-37	37	0.45	9.32	9.32
Total				**4.83**	**100.00**	

1/2"St-5MagAD307						
US Mesh	**Size (mm)**	**Size Range (µm)**	**Passing Size (µm)**	**Weight (g)**	**Weight (%)**	**Cumulative % Passing**
10	2.000	+ 2000		0.00	0.00	100.00
12	1.680	-2000 + 1680	2000	0.00	0.00	100.00
14	1.400	-1680 + 1400	1680	0.03	0.63	100.00
16	1.200	-1400 + 1200	1400	0.04	0.84	99.37
18	1.000	-1200 + 1000	1200	0.02	0.42	98.53
20	0.850	-1000 + 850	1000	0.08	1.68	98.11
30	0.589	- 710 + 589	850	0.25	5.25	96.43
35	0.500	- 589 + 500	589	0.08	1.68	91.18
50	0.300	- 500 + 300	500	0.41	8.61	89.50
70	0.210	- 300 + 210	300	0.28	5.88	80.88
100	0.150	- 210 + 150	210	0.37	7.77	75.00
140	0.105	- 150 + 105	150	0.42	8.82	67.23
200	0.075	- 105 + 75	105	0.51	10.71	58.40
270	0..053	- 53 + 37	75	0.59	12.39	47.69
400	0..37	- 75 + 54	53	0.67	14.08	35.29
		-37	37	1.01	21.22	21.22
Total				**4.76**	**100.00**	

1/2"St-15MagAD128						
US Mesh	**Size (mm)**	**Size Range (µm)**	**Passing Size (µm)**	**Weight (g)**	**Weight (%)**	**Cumulative % Passing**
10	2.000	+ 2000		0.00	0.00	100.00
12	1.680	-2000 + 1680	2000	1.73	11.83	100.00
14	1.400	-1680 + 1400	1680	2.44	16.69	88.17
16	1.200	-1400 + 1200	1400	1.52	10.40	71.48
18	1.000	-1200 + 1000	1200	0.76	5.20	61.08
20	0.850	-1000 + 850	1000	0.91	6.22	55.88
30	0.589	- 710 + 589	850	1.83	12.52	49.66
35	0.500	- 589 + 500	589	0.65	4.45	37.14
50	0.300	- 500 + 300	500	1.79	12.24	32.69
70	0.210	- 300 + 210	300	0.93	6.36	20.45
100	0.150	- 210 + 150	210	0.84	5.75	14.09
140	0.105	- 150 + 105	150	0.59	4.04	8.34
200	0.075	- 105 + 75	105	0.31	2.12	4.31
270	0..053	- 53 + 37	75	0.18	1.23	2.19
400	0..37	- 75 + 54	53	0.10	0.68	0.96
		-37	37	0.04	0.27	0.27
Total				**14.62**	**100.00**	

1/2"St-15MagAD206						
US Mesh	**Size (mm)**	**Size Range (µm)**	**Passing Size (µm)**	**Weight (g)**	**Weight (%)**	**Cumulative % Passing**
10	2.000	+ 2000		0.00	0.00	100.00
12	1.680	-2000 + 1680	2000	0.37	2.52	100.00
14	1.400	-1680 + 1400	1680	0.70	4.77	97.48
16	1.200	-1400 + 1200	1400	0.73	4.98	92.70
18	1.000	-1200 + 1000	1200	0.58	3.96	87.72
20	0.850	-1000 + 850	1000	0.99	6.75	83.77
30	0.589	- 710 + 589	850	1.92	13.10	77.01
35	0.500	- 589 + 500	589	0.58	3.96	63.92
50	0.300	- 500 + 300	500	1.88	12.82	59.96
70	0.210	- 300 + 210	300	1.21	8.25	47.14
100	0.150	- 210 + 150	210	1.27	8.66	38.88
140	0.105	- 150 + 105	150	1.18	8.05	30.22
200	0.075	- 105 + 75	105	1.06	7.23	22.17
270	0..053	- 53 + 37	75	0.87	5.93	14.94
400	0..37	- 75 + 54	53	0.60	4.09	9.00
		-37	37	0.72	4.91	4.91
Total				**14.66**	**100.00**	

1/2"St-15MagAD316						
US Mesh	**Size (mm)**	**Size Range (µm)**	**Passing Size (µm)**	**Weight (g)**	**Weight (%)**	**Cumulative % Passing**
10	2.000	+ 2000		0.00	0.00	100.00
12	1.680	-2000 + 1680	2000	0.07	0.48	100.00
14	1.400	-1680 + 1400	1680	0.15	1.03	99.52
16	1.200	-1400 + 1200	1400	0.19	1.30	98.49
18	1.000	-1200 + 1000	1200	0.14	0.96	97.19
20	0.850	-1000 + 850	1000	0.39	2.67	96.23
30	0.589	- 710 + 589	850	0.86	5.89	93.56
35	0.500	- 589 + 500	589	0.22	1.51	87.66
50	0.300	- 500 + 300	500	1.10	7.54	86.15
70	0.210	- 300 + 210	300	0.84	5.76	78.62
100	0.150	- 210 + 150	210	1.41	9.66	72.86
140	0.105	- 150 + 105	150	1.29	8.84	63.19
200	0.075	- 105 + 75	105	1.24	8.50	54.35
270	0..053	- 53 + 37	75	1.17	8.02	45.85
400	0..37	- 75 + 54	53	1.34	9.18	37.83
		-37	37	4.18	28.65	28.65
Total				**14.59**	**100.00**	

1/2"St-10MagE163						
US Mesh	**Size (mm)**	**Size Range (µm)**	**Passing Size (µm)**	**Weight (g)**	**Weight (%)**	**Cumulative % Passing**
30	0.589	- 710 + 589	850	0.00	0.00	100.00
35	0.500	- 589 + 500	589	0.27	2.77	100.00
40	0.425	- 500 + 425	500	2.37	24.31	97.23
50	0.300	- 425 + 300	425	1.30	13.33	72.92
100	0.150	- 300 + 150	300	1.40	14.36	59.59
140	0.105	- 150 + 105	150	1.24	12.72	45.23
200	0.075	- 105 + 75	105	1.33	13.64	32.51
270	0..053	- 53 + 37	75	0.98	10.05	18.87
400	0..37	- 75 + 54	53	0.55	5.64	8.82
		-37	37	0.31	3.18	3.18
Total				**9.75**	**100.00**	

1/2"St-10MagE245						
US Mesh	**Size (mm)**	**Size Range (µm)**	**Passing Size (µm)**	**Weight (g)**	**Weight (%)**	**Cumulative % Passing**
30	0.589	- 710 + 589	850	0.00	0.00	100.00
35	0.500	- 589 + 500	589	0.46	4.72	100.00
40	0.425	- 500 + 425	500	0.65	6.67	95.28
50	0.300	- 425 + 300	425	0.74	7.60	88.60
100	0.150	- 300 + 150	300	1.07	10.99	81.01
140	0.105	- 150 + 105	150	1.28	13.14	70.02
200	0.075	- 105 + 75	105	1.48	15.20	56.88
270	0..053	- 53 + 37	75	1.66	17.04	41.68
400	0..37	- 75 + 54	53	1.27	13.04	24.64
		-37	37	1.13	11.60	11.60
Total				**9.74**	**100.00**	

1/2"St-10MagE336						
US Mesh	**Size (mm)**	**Size Range (µm)**	**Passing Size (µm)**	**Weight (g)**	**Weight (%)**	**Cumulative % Passing**
30	0.589	- 710 + 589	850	0.00	0.00	100.00
35	0.500	- 589 + 500	589	0.19	1.95	100.00
40	0.425	- 500 + 425	500	0.41	4.20	98.05
50	0.300	- 425 + 300	425	0.48	4.92	93.85
100	0.150	- 300 + 150	300	1.02	10.45	88.93
140	0.105	- 150 + 105	150	1.34	13.73	78.48
200	0.075	- 105 + 75	105	1.64	16.80	64.75
270	0..053	- 53 + 37	75	1.56	15.98	47.95
400	0..37	- 75 + 54	53	1.59	16.29	31.97
		-37	37	1.53	15.68	15.68
Total				**9.76**	**100.00**	

1/2"St-10MagF171						
US Mesh	**Size (mm)**	**Size Range (µm)**	**Passing Size (µm)**	**Weight (g)**	**Weight (%)**	**Cumulative % Passing**
50	0.300	- 425 + 300	425	0.00	0.00	100.00
70	0.210	- 300 + 210	300	3.29	33.78	100.00
100	0.150	- 210 + 150	210	2.30	23.61	66.22
140	0.105	- 150 + 105	150	1.64	16.84	42.61
200	0.075	- 105 + 75	105	1.41	14.48	25.77
270	0..053	- 53 + 37	75	0.54	5.54	11.29
400	0..37	- 75 + 54	53	0.21	2.16	5.75
		-37	37	0.35	3.59	3.59
Total				**9.74**	**100.00**	

1/2"St-10MagF224						
US Mesh	**Size (mm)**	**Size Range (µm)**	**Passing Size (µm)**	**Weight (g)**	**Weight (%)**	**Cumulative % Passing**
50	0.300	- 425 + 300	425	0.00	0.00	100.00
70	0.210	- 300 + 210	300	1.44	14.68	100.00
100	0.150	- 210 + 150	210	1.56	15.90	85.32
140	0.105	- 150 + 105	150	1.59	16.21	69.42
200	0.075	- 105 + 75	105	1.37	13.97	53.21
270	0..053	- 53 + 37	75	1.33	13.56	39.25
400	0..37	- 75 + 54	53	1.27	12.95	25.69
		-37	37	1.25	12.74	12.74
Total				**9.81**	**100.00**	

1/2"St-10MagF319						
US Mesh	**Size (mm)**	**Size Range (µm)**	**Passing Size (µm)**	**Weight (g)**	**Weight (%)**	**Cumulative % Passing**
50	0.300	- 425 + 300	425	0.00	0.00	100.00
70	0.210	- 300 + 210	300	0.83	8.38	100.00
100	0.150	- 210 + 150	210	0.94	9.49	91.62
140	0.105	- 150 + 105	150	1.15	11.62	82.12
200	0.075	- 105 + 75	105	1.29	13.03	70.51
270	0..053	- 53 + 37	75	1.60	16.16	57.47
400	0..37	- 75 + 54	53	1.83	18.48	41.31
		-37	37	2.26	22.83	22.83
Total				**9.90**	**100.00**	

1/2"St-10MagG176						
US Mesh	**Size (mm)**	**Size Range (µm)**	**Passing Size (µm)**	**Weight (g)**	**Weight (%)**	**Cumulative % Passing**
100	0.150	- 210 + 150	210	0.00	0.00	100.00
140	0.105	- 150 + 105	150	3.81	38.53	100.00
200	0.075	- 105 + 75	105	2.86	28.87	61.47
270	0..053	- 53 + 37	75	1.09	11.07	32.60
400	0..37	- 75 + 54	53	0.60	6.04	21.53
		-37	37	1.53	15.49	15.49
Total				**9.89**	**100.00**	

1/2"St-10MagG236						
US Mesh	**Size (mm)**	**Size Range (µm)**	**Passing Size (µm)**	**Weight (g)**	**Weight (%)**	**Cumulative % Passing**
100	0.150	- 210 + 150	210	0.00	0.00	100.00
140	0.105	- 150 + 105	150	1.97	20.35	100.00
200	0.075	- 105 + 75	105	1.77	18.29	79.65
270	0..053	- 53 + 37	75	1.40	14.46	61.36
400	0..37	- 75 + 54	53	1.87	19.32	46.90
		-37	37	2.67	27.58	27.58
Total				**9.68**	**100.00**	

1/2"St-10MagG334						
US Mesh	**Size (mm)**	**Size Range (µm)**	**Passing Size (µm)**	**Weight (g)**	**Weight (%)**	**Cumulative % Passing**
100	0.150	- 210 + 150	210	0.00	0.00	100.00
140	0.105	- 150 + 105	150	1.06	10.69	100.00
200	0.075	- 105 + 75	105	1.11	11.19	89.31
270	0..053	- 53 + 37	75	1.88	18.95	78.13
400	0..37	- 75 + 54	53	2.56	25.81	59.17
		-37	37	3.31	33.37	33.37
Total				**9.92**	**100.00**	

APPENDIX C: BOND WORK INDEX DETERMINATION (MAGNETITE)

Test Conditions

Period	Weight (gram)			Weight (gram)				
	Fresh Feed	Undersize fresh feed	# of revolutions	Oversize	Undersize	Net Undersize	Net Undersize Per Rev	Circulating Load (%)
1	1985.1	279.42	200	1310.2	674.9	395.48	1.98	194.13
2	674.9	95.00	238.8	1387.5	597.6	502.60	2.10	232.18
3	597.6	84.12	229.5	1399.2	585.9	501.78	2.19	238.81
4	585.9	82.47	221.7	1408.6	576.5	494.03	2.23	244.34
5	576.5	81.15	218.1	1415.6	569.5	488.35	2.24	248.57
6	569.5	80.16	217.5	1416.2	568.9	488.74	2.25	248.94

Test Results

Material Charge Weight - 700 ml (g)	1985.1
Test Sieve (µm)	150
IPP (g)	567.2
Undersize in feed (%)	14.08
Circulating Load (%)	249
Grindability (average)	2.24
Product P_{80} (µm)	134
Feed F_{80} (µm)	2055
BWI (kWh/t)	**11.3**

Feed Sieve Analysis						
US Mesh	**Size (mm)**	**Size Range (µm)**	**Passing Size (µm)**	**Weight (g)**	**Weight (%)**	**Cumulative % Passing**
6	3.35	+ 3350		0	0.00	100.00
8	2.38	-3350 + 2380	3350	143.96	9.26	100.00
10	2.000	-2380 + 2000	2380	195.55	12.58	90.74
12	1.680	-2000 + 1680	2000	176.02	11.32	78.16
14	1.400	-1680 + 1400	1680	165.20	10.62	66.84
16	1.200	-1400 + 1200	1400	107.36	6.90	56.22
18	1.000	-1200 + 1000	1200	90.76	5.84	49.31
20	0.850	-1000 + 850	1000	92.90	5.97	43.48
30	0.589	- 710 + 589	850	154.08	9.91	37.50
35	0.500	- 589 + 500	589	47.58	3.06	27.59
50	0.300	- 500 + 300	500	101.36	6.52	24.53
70	0.210	- 300 + 210	300	61.22	3.94	18.01
100	0.150	- 210 + 150	210	48.10	3.09	14.08
140	0.105	- 150 + 105	150	43.06	2.77	10.98
200	0.075	- 105 + 75	105	39.27	2.53	8.21
270	0..053	- 53 + 37	75	30.11	1.94	5.69
400	0..37	- 75 + 54	53	23.51	1.51	3.75
		-37	37	34.81	2.24	2.24
Total				**1554.85**	**100.00**	

Product Sieve Analysis						
US Mesh	**Size (mm)**	**Size Range (µm)**	**Passing Size (µm)**	**Weight (g)**	**Weight (%)**	**Cumulative % Passing**
70	0.210	- 300 + 210	300	0.0	0.00	100.00
100	0.150	- 210 + 150	210	0.0	0.00	100.00
140	0.105	- 150 + 105	150	291.3	51.20	100.00
200	0.075	- 105 + 75	105	154.1	27.09	48.80
270	0..053	- 53 + 37	75	71.1	12.50	21.71
400	0..37	- 75 + 54	53	35.7	6.28	9.21
		-37	37	16.7	2.94	2.94
Total				**568.90**	**100.00**	

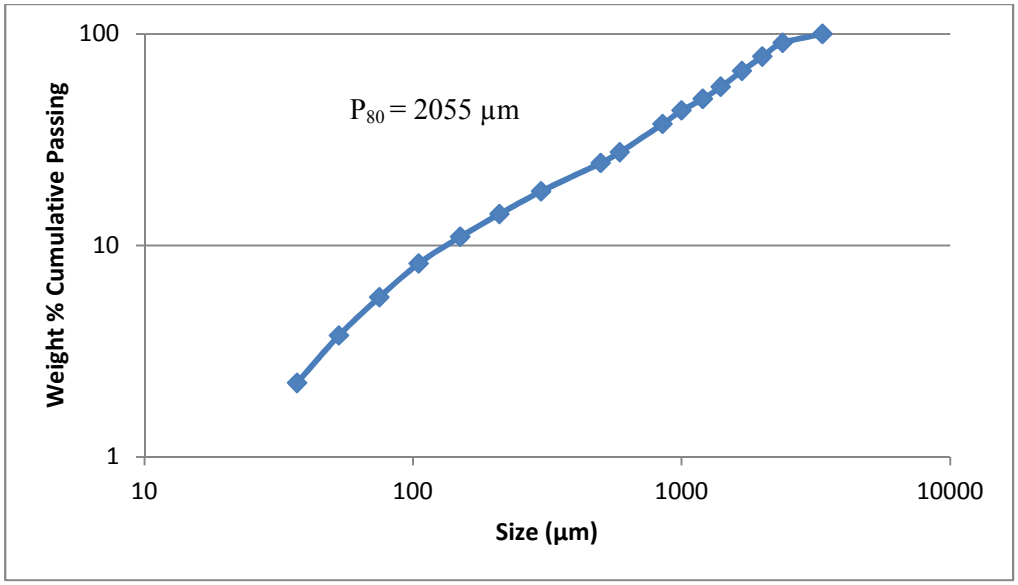

Figure 53. Size analysis of the original feed

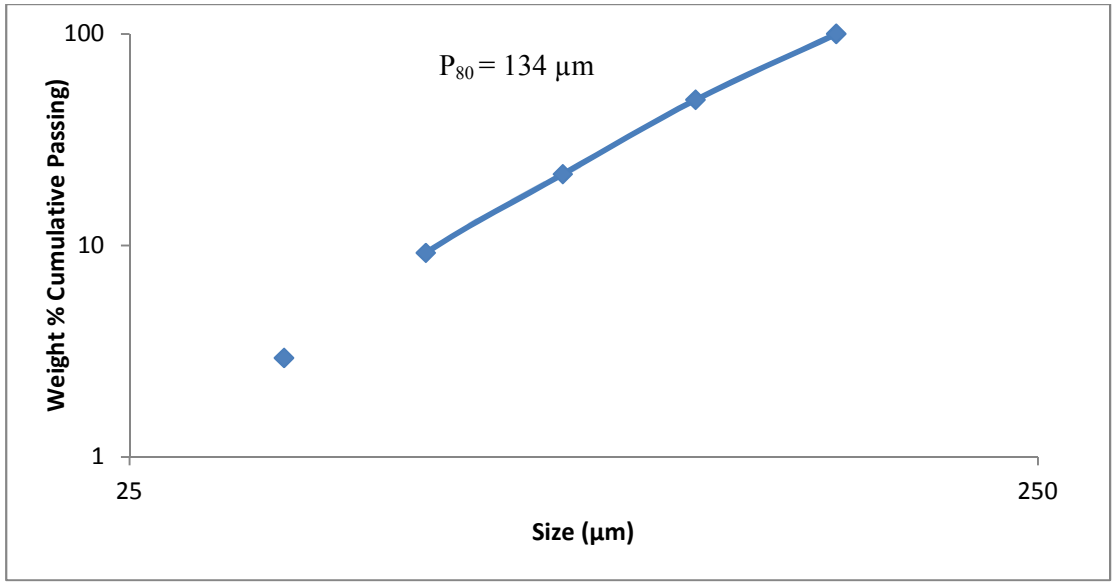

Figure 54. Size analysis of the final product

APPENDIX D: CALCULATIONS OF THE MODIFIED BARMAC CRUSHER

The power requirements of a crusher with a cylindrical rotor of a given height (h) and diameter (D), which accelerates rock particles to a certain tip speed (V) at the moment the particles leave the rotor, is given as follows:

$$\text{Power} = \tau\omega = I\alpha\omega = \frac{MD^2}{8}\omega^3 = \frac{MD^2}{8}\left(\frac{8V^3}{D^3}\right) = \frac{MV^3}{D}$$

$$= \frac{\pi}{4}\rho_r h D^2 \frac{V^3}{D} = \frac{\pi}{4}\rho_r h D V^3$$

$$\Rightarrow \text{Power} = \frac{\pi}{4}\rho_r h D V^3$$

The total production of such a crusher is given by as follows:

$$\text{Production} = \frac{T}{f} = \frac{(1-f_v)P_r L_p}{f} = \frac{(1-f_v)}{f} d_p \omega V_p \left(\frac{h}{s_p}\right)$$

where, $d_p = \frac{\pi D}{s_p} n$, and $\omega = \frac{V}{\pi D}$, and $V_p = {}^4/_3\,\pi(\frac{s_p}{2})^3$

$\Rightarrow$ Production = $\frac{(1-f_v)}{6f}\pi n s_p h V$ (m^3/s)

or converting the units to tph:

$$\text{Production} = 600\pi\frac{1-f_v}{f}\rho n s_p h V$$

h = Rotor height (m)
D = Rotor diameter (m)
V = Rotor speed (m)
M = Rotor mass (Kg)
ρ_r = Rotor density ($t.m^{-3}$)
n = Number of discharge slots
f_v = Void fraction
f = Fraction of ore through rotor
T = Rotor throughput ($m^3.s^{-1}$)
ρ = ore density ($t.m^{-3}$)
s_p = Particle size (m)
V_p = Particle volume (m^3)
L_p = Layers of particles
P_r = Production rate ($m^3.s^{-1}$)
d_p = Particle discharge rate

APPENDIX E: RECOMMENDED MODIFICATION OF TARGET CHAMBER

Redesigning the target chamber to allow the volume of the void space in the sample to not contually decrease in volume as the sample is compressed during impact could result in sustaining the effects of high input energy on the efficiency of particle breakage and may eliminate the observed peak efficiency.

One way to achieve would be to place the sample into a chamber consisting of an annulus around a central movable cylinder. Figure 56 provides the schematics for this chamber. In this apparatus, the projectile (having a tapered front-end) would enter the central cylinder and force particles out against the outer surface of the target chamber generating torsion forces in the particles as they move between the projectile and the chamber wall. This should enhance breakage due to higher transfer of energy as a shear force.

In this scenario, the resultant impact velocity on particles might be significantly less than the projectile velocity, but the distance that the particles move is also less. In addition, a component of the impact force creates shear stresses rather than normal compressive stresses which could also improve efficiency.

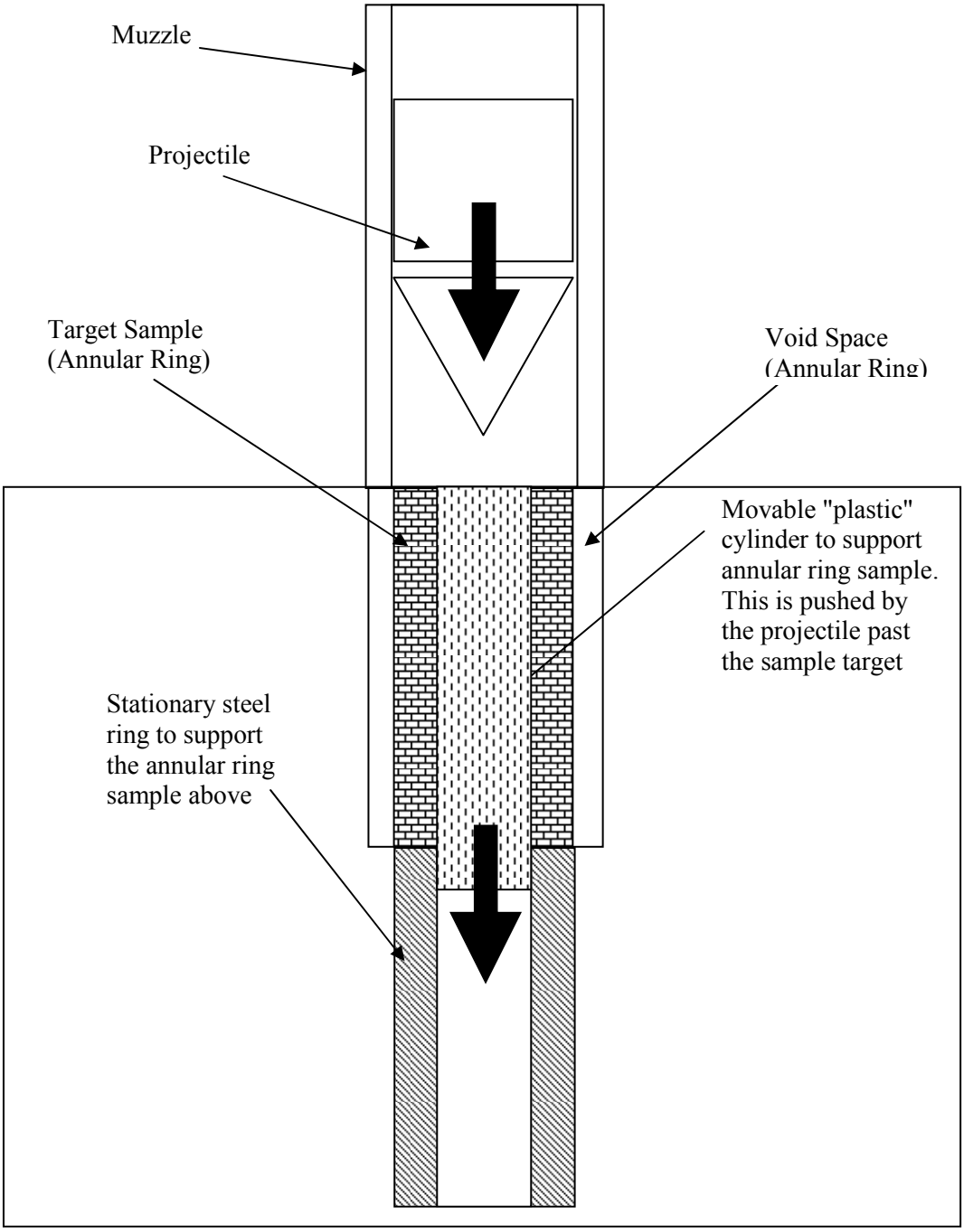

Figure 55. Schematics of a modified target chamber

APPENDIX F: SAMPLE ASSAYING RESULTS

METHOD	Fe-VOL51	ME-ICP61a	ME-ICP61a	ME-ICP61a	ME-ICP61a	ME-ICP61a	ME-ICP61a
SAMPLE	Fe	Ag	Al	As	Ba	Be	Bi
DESCRIPTION	%	ppm	%	ppm	ppm	ppm	ppm
AMOUNT	67.94	<1	0.15	50	<50	<10	<20
METHODS	ME-ICP61a	ME-ICP61a	ME-ICP61a	ME-ICP61a	ME-ICP61a	ME-ICP61a	ME-ICP61a
SAMPLE	Ca	Cd	Co	Cr	Cu	Fe	Ga
DESCRIPTION	%	ppm	ppm	ppm	ppm	%	ppm
AMOUNT	0.56	<10	110	50	30	>50	<50
METHODS	ME-ICP61a	ME-ICP61a	ME-ICP61a	ME-ICP61a	ME-ICP61a	ME-ICP61a	ME-ICP61a
SAMPLE	K	La	Mg	Mn	Mo	Na	Ni
DESCRIPTION	%	ppm	%	ppm	ppm	%	ppm
AMOUNT	<0.1	50	0.43	590	<10	0.13	410
METHODS	ME-ICP61a	ME-ICP61a	ME-ICP61a	ME-ICP61a	ME-ICP61a	ME-ICP61a	ME-ICP61a
SAMPLE	P	Pb	S	Sb	Sc	Sr	Th
DESCRIPTION	ppm	ppm	%	ppm	ppm	ppm	ppm
AMOUNT	1720	690	0.13	<50	<10	10	<50
METHODS	ME-ICP61a	ME-ICP61a	ME-ICP61a	ME-ICP61a	ME-ICP61a	ME-ICP61a	Fe-VOL05
SAMPLE	Ti	Tl	U	V	W	Zn	FeO
DESCRIPTION	%	ppm	ppm	ppm	ppm	ppm	%
AMOUNT	<0.05	<50	<50	1170	<50	1200	23.7